Modeling and simulation of homogeneous nucleation in turbulent flows: physics, methods and realizable solutions

A DISSERTATION
SUBMITTED TO THE FACULTY OF THE GRADUATE SCHOOL
OF THE UNIVERSITY OF MINNESOTA
BY

Nathan James Murfield

IN PARTIAL FULFILLMENT OF THE REQUIREMENTS
FOR THE DEGREE OF
Doctor of Philosophy

Sean C. Garrick

March, 2013

Acknowledgements

Support for this work was provided by the Digital Technology Center at the University of Minnesota. Computational resources were provided by the Minnesota Supercomputing Institute.

Dedication

This work would not have been possible without the support of many people. First and foremost, to my beautiful wife Elisabeth: Your love and support has been unwavering; this has meant the world to me, and the world is ours to have, together. To my daughter Annelise: You amaze me each and every day, and the thought of seeing your beautiful smile more often only furthered my motivation. To my parents: Your support throughout this college experience has meant more than I can convey. Finally, the work here would never have come to fruition without the support of my advisor and mentor, Dr. Sean Garrick. Though the path was indeed long and arduous, your support continued to the end. My deepest, heartfelt gratitude to you all.

Abstract

Numerical simulations of nanoparticle nucleation in turbulent shear flows are performed. We consider the homogeneous nucleation of dibutyl-phthalate (DBP) nanoparticles via direct numerical simulation (DNS) and large-eddy simulation (LES). The flows consist of a high-temperature, DBP-laden stream issuing into a low-temperature, faster or slower moving, DBP-free environment. As the flows cool, via molecular and large-scale convective mixing, the DBP vapor becomes highly supersaturated and particles are formed by nucleation. This particle formation takes place in the absence of condensation or coagulation. Classical nucleation theory is used to model particle nucleation and the Navier-Stokes equations are coupled with the scalar transport equations to provide the fluid, thermal, and chemical fields.

The effects of large-scale mixing and vapor concentration on homogeneous nucleation rates are investigated via DNS in three-dimensional planar jets. The simulation results provide a demonstration of how nucleation takes place in narrow regions where molecular mixing of the two streams occurs. When maximum nucleation rates occur in conditions where the nucleation rates are sensitive to ambient conditions, islands of nucleation form. There are two possible nucleation events: initial shear layer nucleation, and later nucleation in coherent structures or eddies generated by the velocity difference between the jet and the co-flow. A scatter plot diagram of observed dilution paths in temperature versus condensable vapor concentration space where nucleation rates are superimposed is shown to be a convenient tool for analyzing nucleation events. Convection by large-scale eddies gradually spreads the range of mixing paths in this space towards higher nucleation rates. The results also show that boundary conditions, including inlet concentration and velocity ratio, have both qualitative and quantitative effects on particle nucleation. The effects of Lewis number on the homogeneous nucleation of DBP particles are also studied via DNS. Simulations at two Lewis numbers are performed to investigate the effects of molecular mixing on nucleation. These simulations are also carried out at two co-flow velocities to assess the effects of large-scale mixing. The results show that the Lewis number as well the level of large-scale mixing inherent in the flow have substantial effects on particle nucleation.

The effects of the subgrid-scale (SGS) scalar interactions on nanoparticle nucleation are investigated via *a priori* analysis of DNS data. To assess the effect of SGS scalar interactions on DBP particle nucleation, the temperature and mass-fractions are filtered and the resulting quantities are used to compute the nucleating particle field. Two filter widths are used to obtain varying levels of SGS interactions. Particle size distributions are computed to examine the particle fields produced. This work shows that the SGS interactions' effect on nucleation has two distinct trends. In the proximal region of the flow, the unresolved interactions act to decrease particle formation. However, as the flow transitions or becomes turbulent the effect of the SGS interactions acts to increase particle formation.

In the DNS, all relevant length and time-scales are resolved while in LES a closure is used to represent the SGS stress, and fluid-scalar fluxes. We perform the LES at two resolutions to illustrate the effect of "resolving less" and "modeling more". Additionally, to illustrate the effects of the SGS interactions on homogeneous nucleation in turbulent flows, the unresolved scalar-scalar interactions appearing in nucleation source term are neglected. The results again show that nucleation initially occurs in the shear layers where molecular transport dominates and across the span of the wake once the core collapses and the flow transitions to turbulence. Pre-transition, the saturation ratio – representative of the driving force for particle formation – predicted by the LES and DNS is quite similar. Post-transition, the saturation ratios predicted by the LES are significantly greater than those predicted by the DNS, and the discrepancy increases as the filter-width increases (and resolution decreases). This dynamic is also reflected in the nucleation rate. The LES predicts nucleation rates between one and two orders of magnitude greater than the DNS and the discrepancy increases as the resolution decreases. There is also a shift towards the nucleation of smaller nanoparticles in the LES compared to the DNS. The results suggests that the SGS interactions act to decrease the rate of nanoparticle nucleation and increase nuclei size. The compute time between the DNS and LES decreased by three orders of magnitude, suggesting that SGS closures for nucleation would be a significant addition to simulation capabilities and tools. The work concludes with a discussion of a probabilistic method able to resolve these issues, which are inherent to LES.

Contents

List of Tables

List of Figures

Chapter 1

Introduction

1.1 Nucleation and its practical application

Nucleation, in its most basic form, is a phase transition from one state to another [1]. Most routinely this is a transition from the gaseous to liquid or solid phases, or a transition from the liquid to solid state. Gas-phase particle formation issues pose a challenge not only from a scientific viewpoint but from an industrial perspective where quality control issues play a primary role in product design, longevity, and profitability. One of the principal goals of nanoparticle production is to create "near-monodisperse" distributions of particle size [2]. Accurate control of nanoparticle size can affect such physical properties as the anti-fouling ability of titania particles in high performance filtration systems [3], the onset temperature of surface melting of nano-structured materials [4] and the ability of platinum to effectively oxidize carbon monoxide in fuel cells [5]. Additionally, Mayera, *et al.* have shown that particle size directly affects the toxicity and adverse effects of nano-sized particles to the human body [6]. While research has shown, using various methods, that turbulence somehow affects and often increases particle formation via nucleation [7, 8, 9], understanding further the nucleation mechanism and the effect that turbulence has on it is paramount to prediction and control of production of fine particles.

Classical nucleation theory is deeply rooted in both kinetics and thermodynamics. At its most fundamental level, the theory describing nucleation kinetics considers the energy balance between the kinetic energy of molecules engaged in Brownian motion

and the cohesive or inter-molecular forces that bind clusters of molecules together. As a cluster (or droplet in the case of vapor-to-liquid transition) is formed from individual molecules, its surface energy rises from zero to some larger value based upon the cohesive force or surface tension that arises between the constituent molecules. This change in energy, termed Gibb's free energy, is used to quantify the energy balance considered here. By differentiating the free energy with respect to the droplet size, a maximum is found and is termed the energy barrier to droplet formation [10]. Once clusters reach the critical size, by surpassing the energy barrier to nucleation, they become stable droplets or nuclei. In thermodynamic terms, to have a stable droplet the partial pressure of vapor surrounding the droplet must be greater than the saturation vapor pressure of the droplet [11]. The Kelvin relation (also known as the Gibbs-Thompson effect) states that as droplets become smaller and surface curvature increases, the effective vapor pressure of the droplet increases. This directly relates the size of a droplet to the ratio of the droplet's saturation vapor pressure and the surrounding partial pressure, also known as the saturation ratio [12]. The likelihood that clusters form above the critical size or the rate at which they are produced is now a function of the level of super-saturation, which is in turn dictated by the local fluid conditions and material properties of the substance of interest [10].

The pioneering work of Volmer and Weber in the early twentieth century calculated the critical diameter of a nucleating droplet, following Gibbs' initial work [13], above which the droplet grew and below which the droplet dissolved [14]. Cloud chamber experiments were carried out by Wilson (1927) in which he demonstrated the nucleation of water droplets in a cloud chamber in the absence of foreign condensation nuclei, and suggested correctly that the vapor molecules themselves served to incite nucleation [15]. Becker and Döring (1935) continued this work, deriving rudimentary nucleation rate expressions for liquid droplets forming in a vapor [16]. The work of Frenkel (1946) modernized the work of Becker and Döring, providing the expressions for nucleation rate based upon familiar thermodynamic quantities, which have been widely used and cited since [1].

The aforementioned gas-to-particle conversion is termed homogeneous nucleation, which occurs in a system that is free of condensation nuclei. Molecular clusters that are present in all gasses increase in size by the attachment of additional, single molecules

and through cluster-to-cluster collisions [17]. In conditions where the saturation ratio is high, termed super-saturation, these collisions increase in frequency, leading directly to higher rates of homogeneous nucleation [11]. Another, more common type of nucleation is heterogeneous nucleation. Here, condensation nuclei such as dust particles or ionized air molecules serve as the starting point of nucleation [10]. Vapor molecules adhere to the nuclei via condensation, and the droplets grow. While this type of nucleation is nearly ubiquitous in nature and industry (cloud formation, acid rain, industrial gas by-product formation), homogeneous nucleation affords benefits in the research setting. The absence of seed particles makes the process computationally attractive as no Lagrangian-type particle tracking need be employed, and homogeneous nucleation is readily produced in laboratory settings, which has yielded numerous experiments with which to compare results. As the focus of this study is not the molecular dynamics behind nucleation, nano-scale chemistry or the inclusion of evaporation (or for that matter condensation and coagulation), these prefatory limitations are acknowledged and further work in these areas will be left for future studies and to others.

1.2 Simulation of homogeneous nucleation

A number of simulations have been carried out in which formation and growth of nano-sized particles is studied. While these studies provide some insight into the structure of nano-sized particle nucleation and how it is affected by small-scale, turbulent mixing, it is clear that precise knowledge of where nucleation is taking place and what simplifications may be made is needed. A computational method that has the ability to observe the mechanisms in a more accurate way would be advantageous. Additionally, an *accurate* computational method to describe the nucleation process that is tractable in complex engineering flows would allow further study of the phenomena in practical applications.

Direct numerical simulation (DNS) is a computational tool that resolves with no modeling, and in all three spatial dimensions, the evolution of all energy containing scales in a time-accurate manner [18]. DNS has been applied to a variety of very complex flows, and increasing high performance computing (HPC) power allows for larger, more complex flow to be studied, especially those containing turbulence and

turbulent combustion [19, 20]. Also of relevance here, DNS has been used successfully and is well suited to investigate nanoparticle formation and growth in turbulent shear flows [21, 22, 23]. DNS is advantageous in that, unlike other methods, there are very few underlying assumptions, and the simulation is carried out in a model-free manner. Moreover, there is no assumption of the mixing structure that will develop or of the nature of particle distributions in aerosol computations. As nucleation often occurs in the shear layer of a flow where mixing and temperature gradients are highest, the former attribute of DNS is paramount. The accuracy of DNS, though, is weighed against its computational costs; flows of engineering interest are often to computationally expensive to compute. In these situations RANS, and increasingly LES is used.

Large eddy simulation (LES) is a method that is able to capture the large, energy-containing scales of motion of turbulent flows in an unsteady, model-free manner [24]. This is accomplished by solving explicitly for the large scale motion and only modeling the small-scale (or subgrid scale) dynamics, which provides a large computational advantage over DNS. While LES is not yet a design tool that untrained engineers may use without experience or training in LES techniques, it is being used extensively in areas with complex flow where RANS has failed [24]. These areas include active flow control, aeroacoustics, aeropropulsion (including hypersonic propulsion), combustion reactions in aircraft engines and largely separated wake problems such as flow behind moving vehicles, ships, submarines and human bodies [24]. LES has even been used in such varied biological contexts as blood flow through an arterial stenosis [25] and toxicological studies of nanoparticle deposition in the noses of rats [26]. More closely related to the present research is the large eddy simulation of turbulent reacting flows. Studies have been carried of such varied reacting flows as mixing in chemical reactors and aircraft and reciprocating engine combustion [27, 28]. Additionally, the LES methodology has been successfully implemented in a number of turbulent shear flows containing nanoparticle formation and growth [29, 30] and this work aims to build upon these successes. LES, though, by its nature has the distinct disadvantage that the smallest mixing scales are not resolved, but rather must be modeled. In turbulent, reacting flows this may obscure the role turbulent fluctuations play and subgrid scale closure (modeling) is needed to capture the dynamics of these smallest mixing scales.

Probability density function or PDF-based methods' application to turbulent reacting flows was proposed by Givi (1989) and has been used extensively since [31]. In the case of flows with chemical reactions, PDF methods overcome the closure problems that arise in the non-linear reaction rates in simple LES by using a PDF to describe the subgrid scale or unresolved quantities [32]. PDF methods have compelling advantages modeling chemically reacting turbulent flows in that they provide an elegant and effective resolution to the closure problems that arise from averaging or filtering the highly nonlinear source terms in the instantaneous governing equations [33]. Using a version of the PDF based upon the filtered quantities present in LES, termed the filtered density function (FDF), PDF methods are directly applicable to LES and methods describing the transport of the FDF have been derived [34]. Using the FDF, the scalar quantities are completely described statistically at each point in the flow [35]. This provides an immense advantage over the simple use of filtered quantities in that the scalar quantities retain the variation required to correctly be used in non-linear source terms, especially important in processes such as combustion or nucleation. FDF methods have been particularly successful in turbulent reacting flows involving combustion [36, 37, 38] and have been applied directly to nucleation in a limited sense [39, 40]. PDF methods have even been applied to distinct two-phase flow containing water droplets [41]. While the source terms appear in closed form in PDF or FDF methods, closure is still needed for the subgrid scale mixing of scalars. Micro-mixing models are required to close the mixing term in transported PDF and FDF methods [35]. These models account for the effects of molecular diffusion or mixing within the subgrid scale [42].

1.3 Intent of research

The intent of this work is to further the understanding of homogeneous nucleation, and to determine what modeling assumptions most affect simulation of nucleation. First, the structure of nucleation in turbulent flows is investigated. The level of large-scale mixing and vapor concentration are varied to determine what factors most affect the nucleation process. Additionally, the effect of different vapor and thermal diffusivities (vis-a-vis the Lewis number) is investigated.

The next analyses are carried out to elucidate the effect that small-scale mixing has

on nucleation. Artificial mixing introduced here by way of spatial filtering may greatly affect the rates of particle formation, as well as the properties of particles produced. Utilizing data from direct numerical simulation (DNS) and examining the consequences of filtering, the effects of augmented (and often artificial) small-scale mixing may readily be seen. An *a priori* analysis is beneficial to ascertain whether a PDF method can provide tangible improvements over the simple use of filtered precursors; if the use of filtered quantities alters the predictions of the nucleation source term, an improved method would be beneficial.

Large eddy simulation (LES) of nucleation in turbulent wakes is carried out next. By comparing the LES solutions to that of the DNS, the accuracy of traditional LES in the context of homogeneous nucleation can be determined and its shortcomings ascertained. Finally, a filtered density function (FDF) method is discussed, which has the possibility to more accurately describes all dependent variables present in the nucleation source term. The implications of a successful LES method to compute homogeneous nucleation are not insignificant. Currently, DNS is needed to accurately model homogeneous nucleation, though some attempts to model nucleation with traditional LES have been carried out. A successful LES method would *more accurately* allow homogeneous nucleation calculations to begin to move from the research community, capable of carrying out DNS, to the engineering community, carrying out more computationally affordable LES, in practical flows.

Chapter 2

The structure of nanoparticle nucleation in three-dimensional planar jets

2.1 Introduction

In various processes, homogeneous nucleation that occurs in turbulent flow is a key issue in determining the properties of resulting aerosol. Examples can be found in nanoparticle synthesis, exhaust gas emissions, aerosol dilution and sampling techniques as well as in atmospheric processes. As nucleation rates are very sensitive to small changes in local ambient conditions, turbulence-induced fluctuations are an important consideration in the modeling of these phenomena. A case that is often encountered in practice is that of a a hot jet or a plume that contains condensable vapors issuing into colder ambient air. Turbulent eddies are involved in transporting the vapors into cooler regions where they become supersaturated enough for homogeneous nucleation to occur. The overall mixing process involves advective transport by eddies and molecular mixing at the edges of these eddies. Roughly speaking, larger eddies are mainly responsible for the overall mixing in the large scale, while the coupled action of small-scale eddies and molecular diffusion are responsible for the micro-level mixing. In this paper, we focus on homogeneous nucleation that occurs when temperature and saturation pressure decrease as

a result of turbulent mixing. Other important pathways for particle formation are nucleation due to chemical reactions, and nucleation due to a pressure drop in supersonic flow. Examples of nucleation by chemical reactions are titanium dioxide particle formation [43, 44, 45] and soot particle inception [46, 47]. Converging/diverging nozzles provide an example of pressure drop induced nucleation [48, 49].

There are a number of studies, both experimental and theoretical, on the effect of turbulence on homogeneous nucleation. Lesniewski and Friedlander (1998) carried out a series of experiments on dibutyl-phthalate (DBP) nucleation and growth in turbulent round jet shear layers [50]. In the analysis of their experiments, Lesniewski and Friedlander (1995,1998) took advantage of the fact that, in round jet flows, RMS fluctuations, probablity density functions (PDFs) and mean values of temperature and gaseous species concentration are known to depend only on the ratio of the radial position in the shear layer to the axial position [51, 50]. The PDFs do not have a Reynolds number dependence. In order to render the problem amenable to a simple computational analysis, they assumed that heat and the condensable vapor diffuse in a similar fashion, i.e. that the Lewis number Le is equal to one. In addition, nucleation was assumed to be limited to the shear layer. With these assumptions, shear layer nucleation was shown to be proportional to d_{jet}^3, where d_{jet} is the diameter of the jet, and to be independent of the jet velocity. With high enough DBP concentration, nucleation outside the shear layer was also observed in the experiments. In addition to the fundamental studies by Lesniewski and Friedlander (1998) and preceding studies of similar type summarized in their paper, there are a number of more applied studies on nucleation and aerosol dynamics in exhaust plumes. The simulations of Wu and Menon (2001) are the most relevant to this work [52] . They simulated aerosol particle formation via binary nucleation of sulphuric acid - water vapor system using a linear eddy model. In the linear eddy model, a one-dimensional grid that is perpendicular to the plume is marched and stretched along the plume and turbulent mixing is represented with a series of stochastic mappings in this space. The peak number density was shown to be under-predicted by about 40% when micromixing was not included in the simulations. More recently, Housiadas *et al.* (2004) showed using data from a LES study of the planetary boundary layer that the effect of turbulence on the overall atmospheric nucleation rate in a sulfuric acid - water vapor system is not very large in the cases they considered [53].

Also recently, Shaw (2004) demonstrated with asymptotic analysis that mean particle formation rates are essentially dependent only on the value of the PDF at which the exponential of the nucleation rate expression attains maximum [39].

A computational fluid dynamics technique called direct numerical simulation (DNS) is used to capture the mixing process in a model-free manner [31]. Both the convective/advective action of the eddies and the molecular mixing processes are considered explicitly. No assumptions regarding flow structure or the nature of the molecular mixing process need to be made. Instead, the Navier-Stokes equations and other transport equations are solved down to the smallest scales. The methodology is general and not restricted to a single flow configuration. The disadvantage of DNS is the large amount of computational resources it requires. This limits the applicability of DNS to relatively simple cases, and to relatively low levels of turbulence. Even so, these cases are valuable since as a mixing process, they contain most of the same salient features that exist in more complex flows. This makes it possible to infer or test models or theories of nucleation in turbulent flow. The visualization of the results provides an instructive and easily understandable insight into the fine-structure details of the nucleation process. A similar degree of information is not available from today's experimental techniques. The framework of DNS allows, in a relatively straightforward manner, the inclusion of other phenomena such as heterogeneous condensation, surface reactions, coagulation and intra-particle processes. The DNS methodology is potentially even more beneficial in dealing with the effects of micro-mixing when some of these mechanisms are significant as well, and coupled with each other, since such cases are beyond the scope of simplified models.

In this work, we analyze nucleation in the eddies formed by three-dimensional, cooling planar jet flows. The flow and the transport of vapor and particles are modeled with a three-dimensional DNS code. This configuration and modeling approach has been used in a number of University of Minnesota studies to simulate reacting flows [54, 55, 56]. In the studies reported in this paper, homogeneous nucleation is considered to be the sole aerosol transformation mechanism. This goal of this work is to provide insights into homogeneous nucleation under various mixing intensities and its DNS modeling as well as to act as a stepping stone toward turbulent mixing cases that involve other phenomena as well. Dibutyl-phthalate (DBP) is adopted as an example

species because it has been used widely in experimental nucleation research, modeling studies and as a large molecule it is representative of heavy organic compounds that are important in fine particle emission issues.

2.2 Formulation

2.2.1 Fluid field

The flow and temperature fields are represented by the Navier-Stokes equations for compressible non-isothermal flow:

$$\frac{\partial \rho}{\partial t} + \frac{\partial \rho u_j}{\partial x_j} = 0, \tag{2.1}$$

$$\frac{\partial \rho u_i}{\partial t} + \frac{\partial \rho u_i u_j}{\partial x_j} = -\frac{\partial p}{\partial x_i} + \frac{\partial \tau_{ij}}{\partial x_j}, \tag{2.2}$$

$$\frac{\partial \rho h}{\partial t} + \frac{\partial \rho u_j h}{\partial x_j} = \frac{\partial}{\partial x_j}\left(\frac{k}{C_p}\frac{\partial h}{\partial x_j}\right), \tag{2.3}$$

where $u_i(\bar{x}, t)$ is the velocity vector, $p(\bar{x}, t)$ is the fluid pressure, $\rho(\bar{x}, t)$ is the fluid density, $h(\bar{x}, t)$ is the enthalpy, τ_{ij} is the viscous stress tensor for a Newtonian fluid, C_p is the fluid specific heat capacity under constant pressure, and k is the thermal conductivity of the fluid. The ideal gas law closes the equation system.

2.2.2 Aerosol field

In the cases presented this paper, the fluid consists of air, the properties of which are set to determine bulk fluid properties, and DBP which is considered to be a trace species. The equation of transport of DBP vapor, with a nucleation sink term $\dot{\omega}_{nucl}$ for the DBP vapor mass concentration, is given by the species conservation equation:

$$\frac{\partial \rho Y}{\partial t} + \frac{\partial \rho u_j Y}{\partial x_j} = \frac{\partial}{\partial x_j}\left(\rho \mathcal{D}_Y \frac{\partial Y}{\partial x_j}\right) - \dot{\omega}_{nucl}, \tag{2.4}$$

where Y is the mass fraction of the condensable DBP vapor, and $\mathcal{D}_Y$ is its diffusion coefficient. The heat release due to nucleation is neglected in this work since we only deal with low mass conversions, but its inclusion would be a simple thing.

The transport of the nucleated particles and their size distribution are solved for. As no other phenomena besides nucleation are included in the simulation, the nucleated particles retain the critical sizes they have at formation. The neglect of heterogeneous condensation and coagulation are valid at the initial stages of nucleation, and when small particle concentrations are generated. This is not necessarily true in the simulated cases when the inlet concentration of DBP is high. Therefore, high number concentration regions in such simulation results should be understood as areas where other phenomena can be active, and the predicted number concentration values should be taken as theoretical limits in the absence of these phenomena. Particle sizes are recorded using a sectional grid. The grid consists of nine nodal grid points or bins which are given in a series of doubling particle volumes such that they cover the range of critical clusters possible during appreciable nucleation. For particles in bin k, the transport equation for the mass fraction Q_k is given as:

$$\frac{\partial \rho Q_k}{\partial t} + \frac{\partial \rho u_j Q_k}{\partial x_j} = \frac{\partial}{\partial x_j}\left(\rho \mathcal{D}_Q \frac{\partial Q_k}{\partial x_j}\right) + \dot{\omega}_{nucl\ k}, \tag{2.5}$$

where $\mathcal{D}_Q$ is the particle diffusivity. Since in the simulations of this paper the average distances the nucleated particles diffuse are very short, the differences in the diffusivities of particles of various sizes do not have practical effects on the results. However, the Eulerian simulation of particles of very small diffusivity creates a large computational burden on the DNS simulation method. Therefore, the particle diffusion coefficients for all the bins are simply given such that they correspond to a Schmidt number 2.0, which still yields low particle diffusion and retains the computational burden manageable. For a more detailed discussion of this approximation, see Garrick and Khakpour (2004) [55].

Nucleation is modeled with the expression of Girshick and Chiu (1990) [57]. It is based on a kinetic approach and applies a correction to the classical nucleation expression that forces the Gibbs free energy for monomers to zero. The equation is derived for steady-state conditions, and therefore the time scale of fluctuations for local conditions should be smaller than that required to reach steady-state nucleation. It is good to bear in mind that nucleation rate expressions involve significant uncertainties. To a considerable degree, these arise from the use of macroscopical properties to represent molecular scale phenomena. To cope with these uncertainties, we make use of empirical data on DBP nucleation. We supplement the nucleation rate expression by multiplying

the rate expression with a correction factor c_{nuc}. For DBP, we use a correction factor c_{nuc} value 3.2×10^{-4} derived by PyykönenandJokiniemi(2000) based on the analysis laminar flow reactor experiments of Nguyen *et al.* (1987) [58, 59]. Nucleating particles have the size of a critical cluster (of diameter d_C) determined by:

$$d_C = \frac{4\sigma v_m}{k_B T \ln(S)}, \tag{2.6}$$

where σ is the surface tension of the condensed species (here DBP), v_m is its molecular volume, k_B is the Boltzmann constant, T is the temperature, and S is the saturation ratio of the condensable vapor.

The classical expression for nucleation rate as formulated by Frenkel J_{Fr} is given by:

$$J_{Fr} = \frac{(\rho Y)^2}{\rho_c m_m}\sqrt{\frac{2\sigma}{\pi m_m}}\exp\left(-\frac{\pi\sigma d_C^2}{3k_B T}\right), \tag{2.7}$$

where m_m is the mass of a molecule of condensable species and ρ_c is the condensed phase density. With the self-consistent correction of Girshick and Chiu (1990), the nucleation rate J_{Gi} can be expressed as:

$$J_{Gi} = \frac{1}{S}\exp\left(\frac{\sqrt[3]{36\pi v_m^2}\sigma}{k_B T}\right) J_{Fr}, \tag{2.8}$$

The sink term for nucleation $\dot{\omega}_{nucl}$ is the nucleation rate J_{Gi} multiplied by the empirical correction factor c_{nuc} and the mass of a critical cluster:

$$\dot{\omega}_{nucl} = c_{nuc}\frac{\pi}{6}\rho_c d_C^3 J_{Gi}. \tag{2.9}$$

Since we consider nucleation as the only aerosol transformation mechanism, the nucleating critical cluster is size-split in the sectional representation between neighboring bins such that the particle number and volume concentrations are conserved [60]. In one physical grid point at one time step, only these two bins have a non-zero nucleation source term $\dot{\omega}_{nucl\ k}$. The sum of these two nucleation mass conversion rates equals the total nucleation rate $\dot{\omega}_{nucl}$. The size-split can be represented using a mass splitting function $\Xi_k(v)$:

$$\dot{\omega}_{nucl\ k} = \Xi_k(v_p^\star)\dot{\omega}_{nucl}, \tag{2.10}$$

where $v_p^\star$ is the volume of critical cluster, and the mass splitting function is given by:

$$\Xi_k(v) = \begin{cases} \frac{v_{k+1}-v}{v_{k+1}-v_k}, & \text{if } v_k \le v < v_{k+1} \\ \frac{v-v_{k-1}}{v_k-v_{k-1}}, & \text{if } v_{k-1} \le v < v_k \\ 0, & \text{otherwise.} \end{cases} \tag{2.11}$$

2.2.3 Non-dimensionalization

For computational efficiency and consistency, the transport equations are rendered nondimensional. This is done with the definition of following nondimensional variables (marked with $\star$) and reference values (marked with subscript o):

$$x_j^\star = \frac{x_j}{L},\ t^\star = \frac{t}{L/U_0},\ u_j^\star = \frac{u_j}{U_0},\ p^\star = \frac{p}{\rho_0 U_0^2},\ \rho^\star = \frac{\rho}{\rho_0},\ T^\star = \frac{T}{T_0},$$

$$h^\star = \frac{h}{h_0},\ Y^\star = \frac{Y}{Y_0},\ Q_k^\star = \frac{Q_k}{Q_0} \tag{2.12}$$

where L is the reference length scale, U_o is the reference velocity, T_o, h_o, and ρ_o are the reference values for temperature, enthalpy, and fluid density, respectively, and Y_o and Q_o are the reference values for vapor and particle size mass fractions, respectively. In addition, dimensionless property variables for condensed phase density $\rho_c^\star$ and surface tension $\sigma^\star$ are defined similarly with the reference values ρ_{co}, σ_o estimated at reference conditions (T_o, ρ_o). The reference value for molecular volume of condensable species v_{mo} is also estimated in reference ambient conditions. The familiar non-dimensionalized mass, momentum, enthalpy and mass-fraction transport equations are given by

$$\frac{\partial \rho^\star}{\partial t^\star} + \frac{\partial \rho^\star u_j^\star}{\partial x_j^\star} = 0, \tag{2.13}$$

$$\frac{\partial \rho^\star u_i^\star}{\partial t^\star} + \frac{\partial \rho^\star u_i^\star u_j^\star}{\partial x_j^\star} = -\frac{\partial p^\star}{\partial x_i^\star} + \frac{1}{Re}\frac{\partial^2 u_i^\star}{\partial x_j^\star \partial x_j^\star}, \tag{2.14}$$

$$\frac{\partial \rho^\star h^\star}{\partial t^\star} + \frac{\partial \rho^\star u_j^\star h^\star}{\partial x_j^\star} = \frac{1}{RePr}\frac{\partial^2 h^\star}{\partial x_j^\star \partial x_j^\star}, \tag{2.15}$$

$$\frac{\partial \rho^\star Y^\star}{\partial t^\star} + \frac{\partial \rho^\star u_j^\star Y^\star}{\partial x_j^\star} = \frac{1}{ReSc_Y}\frac{\partial^2 Y^\star}{\partial x_j^\star \partial x_j^\star} - \dot{\omega}_{nucl}^\star, \tag{2.16}$$

where Re is the Reynolds number, Pr is the Prandtl number, and Sc_Y is the vapor Schmidt number. The non-dimensional transport equation for the condensable vapor mass fraction is given by

$$\frac{\partial \rho^\star Q_k^\star}{\partial t^\star} + \frac{\partial \rho^\star u_j^\star Q_k^\star}{\partial x_j^\star} = \frac{1}{ReSc_k}\frac{\partial^2 Q_k^\star}{\partial x_j^\star \partial x_j^\star} + \dot{\omega}_{nucl\ k}^\star, \tag{2.17}$$

where Sc_k is the Schmidt number of bin k particles. The critical diameter can be expressed in terms of dimensionless variables as

$$d_C^\star = N_1 \frac{\sigma^\star}{\rho_c^\star T^\star \ln(S)}, \tag{2.18}$$

where the constant N_1 is given by

$$N_1 = \frac{\sigma_o v_{mo}}{k_B T_o}. \tag{2.19}$$

The non-dimensional form of the nucleation sink term is given by:

$$\dot{\omega}^\star = \frac{L}{U_o \rho_o} N_2 \frac{\rho^{*2} Y^{*2}}{\rho_c^\star \sqrt{\sigma^\star} S} \exp\left(N_3 \frac{\sigma^\star d_C^{\star 2}}{T^\star} + N_4 \frac{\sigma^\star}{\rho_{c*}^{2/3} T^\star}\right), \tag{2.20}$$

where the constants N_2, N_3 and N_4 are defined as:

$$N_2 = \frac{\rho_o^2 Y_o^2}{\rho_{co} m_m}\sqrt{\frac{2\sigma_o}{\pi m_m}}, N_3 = \frac{\pi \sigma_o}{3 k_B T_o}, N_4 = \frac{\sqrt[3]{36\pi v_{mo}^2}\sigma_o}{k_B T_o}. \tag{2.21}$$

2.3 Results

2.3.1 Flow configuration

The flow configuration in this research is a three-dimensional heated planar jet. A warm jet ($T_o = 400K$) of particle-free air doped with DBP vapor issues into a co-flow of approximately room-temperature ($T_\infty = 300K$) air. A schematic of the configuration is presented in Fig. 1. The jet originates in a nozzle of diameter D. At the nozzle outlet, the jet has a velocity u_o, density ρ_o, viscosity μ_o and a temperature T_o. The Reynolds number of the jet nozzle is $Re = \rho_o u_o D/\mu_o = 4000$. While the flow field is determined by the Reynolds number, the time scale of the nucleation phenomena is determined by the jet velocity u_o that is 100m/s and the jet diameter that is $0.57mm$ which result in a residence time of 0.114ms through the domain at the velocity of the jet. By varying the

velocity of the co-flowing stream, u_∞, different mixing intensities are generated. Two co-flow velocities are considered - $u_\infty/u_o = 0.55$ (a) and $u_\infty/u_o = 0.33$ (b). For the DBP mass-fraction, we use two values defined such that the initial saturation ratio S at $T_o = 400$K is either $S_o = 1$ (case 1) or $S_o = 5$ (case 2). At these conditions the Prandtl number is $Pr = 0.69$ and the Schmidt number is $Sc = 2.6$. The simulated cases are summarized in Table 2.1.

2.3.2 Physical properties

The properties of DBP are taken from Nguyen *et al.* (1987) [58]. We adopt these values since they were also used in Wilck and Stratmann (1997) and Pyykönen and Jokiniemi (2000) in the estimation of the empirical correction factor for the DBP nucleation rate expression [61, 59]. The saturation mole fraction is $x_{sat} = \exp(21.497 - 11497/T)$, the surface tension is $\sigma = 0.0353 - 0.0000863 \times (T - 273.16)$, the condensed phase density is $\rho_c = 1063 - 0.826 \times (T - 273.16)$ and the DBP vapor is $\mathcal{D}_m = 3.984 \times 10^{-6}(T/273.16)^{1.5}$ As the focus of this paper is on nucleation modeling in the context of turbulent flow in general and DBP is just used as an example species, we content ourselves to adopting these values and do not embark on sensitivity studies with respect to these estimates. A discussion of various DBP property estimates and their implications on nucleation rate predictions can be found in Wilck *et al.* (1998) [62]. They show that property estimates are an important topic whenever comparisons to experimental data are made. The non-dimensional parameters given by Eq. (2.19) and Eq. (2.21) have values of $N_1 = 8.5 \times 10^{-9}$, $N_2 = 4.6 \times 10^{30}$, $N_3 = -4.6 \times 10^{18}$ and $N_4 = 13$ for the reference values of Case 1. As the inlet DBP mass-fraction is the only reference value unequal between the two cases, the second parameter is the only different value in Case 2, $N_2 = 2.3 \times 10^{31}$.

One detail of the inlet boundary conditions deserves special attention. In order to avoid pressure oscillations, the profiles of various flow quantities at the jet inlet do not have sharp changes. Instead, the values of velocity, temperature and vapor species concentration change smoothly over a small distance. Strictly speaking, the boundary conditions at the jet inlet ought to include the effects of the nozzle wall boundary layers that precede the simulation domain. In this case, however, the scope of this simulation setup is the dynamics in the turbulent eddies generated by the velocity difference

between the jet and the co-flow, not the entrance phenomena in the region strongly affected by preceding domain. Normally the smooth transition in the inlet profile is not an issue. However, since there is a large difference in DBP vapor pressures between the jet and the co-flow temperatures, there is a possibility of high supersaturations in the inlet profile transition region and nucleation right from the start. Some initial stage for the temperature and vapor species mixing process must be assumed at the beginning of the computational domain. It is possible to envision that the computational domain starts a short distance after the nozzle outlet. An approximation of one-dimensional transient conduction and diffusion in average conditions over the short distance from the actual nozzle outlet to the beginning of the computational domain provides a reasonable estimate of the initial stage of mixing. This approximation yields error function based profiles. The transition for T as a function of the distance from the centerline y is as follows:

$$T(y) = T_\infty + \frac{1 + erf(C_t(D/2 - |y|))}{2}(T_o - T_\infty), \tag{2.22}$$

where C_t is a constant that defines the width of the transition region. Here it is given a value $C_t = 17.25$. The equivalent transition for the vapor concentration Y is given as follows:

$$Y(y) = Y_\infty + \frac{1 + erf\left(\sqrt{Le_{1/2}}C_t(D/2 - |y|)\right)}{2}(Y_o - Y_\infty), \tag{2.23}$$

where $Le_{1/2}$ is the Lewis number estimated in the average conditions. The real scope of the simulation setup is nucleation after the initial shear layer. These inlet boundary conditions allow us to make rough estimates of the initial shear layer nucleation. The possible effects of nozzle boundary layer turbulence, though, are neglected.

2.3.3 Numerical specifications

The non-dimensionalized transport equations are solved using MacCormack-based, high-order, finite difference scheme [63, 64]. The accuracy of the method is second order in time and fourth order in space. The computational grid for the domain presented in Fig. 1 consists of $1280 \times 512 \times 480$ grid points, clustered about the shear layers in the y-direction. For time-averaging, the recording of the instantaneous values is started when the initial transitional features have disappeared after the co-flow has swept the domain once. Usually in these simulation, values are recored at each time step until

the co-flow has swept the domain twice. Here at least twice longer simulations were necessary due to the sensitive nature of nucleation. Even so, the time-averaged results are not perfect, and asymmetry with respect to the centerline is present.

The time step is determined by the simulation method based on the smallest scale transport phenomena. This is determined to be in dimensional units 10^{-8} s. According to Lesniewski and Friendlander (1998) the time required to reach steady-state nucleation in their their experiments, with conditions close to ours, is of the order of 10^{-8} s [50]. This means that we are at the limit of the validity of the steady-state equation, and with the highest nucleation rates probably beyond the limit. Therefore, nucleation rate predictions must be considered as upper limits in the absence of the kinetic restrictions of molecular cluster dynamics. Note that the way we determine the time scale for turbulent fluctuations provides a much lower time scale than the estimate of residence time in the shear layer employed by Lesniewski and Friendlander (1998).

2.3.4 Dilution process

Low concentration case

We begin the discussion of simulation results by considering the low concentration case (1) where the saturation ratio of DBP in the jet is $S = 1$ at $T = 400K$. The condensable vapor and temperature mix by diffusion at the interface of the two streams leading to supersaturation. The overall rate of nucleation does not reach high enough levels to bring about significant consumption of the DBP vapor in this or other cases since residence times in the domain are very short (in this case $0.114ms$ at the velocity of the jet). Instantaneous contours of the normalized temperature, $\theta = (T - T_\infty)/(T_o - T_\infty)$, are shown in Fig. 2.2. These results provide an indication of the amount of cooling that occurs. For example, there are still regions with fluid near the inlet temperature ($\theta = 1$) at the end of the computational domain in case 1a. However, in case 1b the flow has cooled considerably more, with isolated pockets of fluid with maximum temperatures of approximately 75% of the inlet temperature.

Depending on the mixing process and its state, various instantaneous saturation ratios and nucleation rates are observed. Instantaneous nucleation rate profiles are shown in Fig. 2.3. Appreciable nucleation does not start at the nozzle outlet, but later

in the shear layer. Visible in the instantaneous figures is the great local variation in the instantaneous nucleation rates. Indeed, clearly distinct eddy sections where nucleation takes place can be observed. It is also clearly visible that the narrow sharp-edged regions where high saturation ratios and nucleation rates exist are at the interface of the two streams where the molecular mixing processes take place. The initial nucleation rates are determined by the transition boundary condition in Eq. (2.22) and Eq. (2.23). While the instantaneous nucleation rates vary greatly, their maximum values typically determine the level of the the time-averaged rates, profiles of which are shown in Fig. 2.4. At the first half of the domain, though, the difference between the instantaneous and mean rates can be larger, since very high instantaneous rates are only observed occasionally. Also of note in Fig. 2.4 is the obvious effect of the increased mixing of case 1b. Not only does the increased large-scale mixing bring about higher nucleation rates, but it spreads the nucleation across a wider area by the end of the domain. In spite of the wide variation of instantaneous nucleation rates, their values are typically of the same order as the average rates. High instantaneous rates are only encountered occasionally, but they are dominant in the arithmetic averaging.

It is useful to look at the dilution process in temperature vs. DBP mass-fraction space. The dilution process involves a large number of mixing paths that are determined by both turbulent convective and molecular mixing mechanisms. Various saturation ratios and nucleation rates arise along these different mixing paths. We can visualize the dilution process by presenting instantaneous values as dots in this space. A normalized mass fraction is defined as $\phi = (Y - Y_\infty)/(Y_o - Y_\infty)$. In Fig. 2.5 each scatter plot contains only values from the second half of the domain along the flow direction (x) so that the effect of the initial profile assumption are minimal. Since pressure variations are small in our subsonic flow, the nucleation rates are essentially only dependent on two ambient condition characteristics: temperature and DBP mass-fraction, while other quantities in the nucleation rate expression can be expressed in terms of these. Thus, we can superimpose the nucleation rates in the same diagram where we have our mixing process visualized as points in the space. In the figures, iso-contours of nucleation rates are shown as lines of various logarithms of equal nucleation rate in particles/$(m^3 \cdot s)$. Since the diffusivity of heat is higher than that of DBP vapor, indicated by a Lewis number of $Le = 5.4$, temperatures between the two extremes are reached faster than

equivalent intermediate mass-fractions. The implication of this is visible the $\theta - \phi$ diagrams in Fig. 2.5. The dotted mixing region assumes a shape where, at the edges, the region is on the side of intermediate temperatures of the $\theta = \phi$ line, and in the center of the graph the "gradient" of the region is lower that of the $\theta = \phi$ line. The initial boundary condition is a curve of similar shape. As the flow proceeds, this curve widens to a region due to varying mixing situations experienced in the eddies. High nucleation rates can be seen in the $\theta - \phi$ diagram to occur at mid-range DBP mass-fraction. These highest nucleation rates are attained only toward the end of the domain where considerable cooling has occurred.

These instantaneous plots (along with the contours of Fig. 2.2) clearly indicate that mixing is more intensive in case 1b. More intensive mixing and lower average velocity means that the initial shear layer around the undisturbed wedge is shorter, the phenomena occur faster over a certain distance, and more growth of the $\theta - \phi$ mixing region towards higher nucleation rates takes place within the domain. Overall, the difference in the $\theta - \phi$ diagram is not very large. However, even the relatively small difference is significant since the nucleation rates vary on a logarithmic scale. This causes higher nucleation rates and number concentrations of particles to be generated in the high mixing case. An additional cause for higher time-averaged nucleation rates is that even in the relative sense there is more interface area between the two streams in the high mixing case in the area affected by the jet.

High initial saturation ratio case

In the high inlet saturation ratio flow, the DBP mass-fraction is increased such that $S = 5$ at $T = 400K$. The nucleation process under these conditions exhibits both qualitative and quantitative differences. The nucleation rates are much higher and more uniform than in the low mass-fraction case. To illustrate better the mixing structure and its relation to the nucleation dynamics, contour slices of the nucleation rate are shown along with iso-surfaces of vorticity (of value $\Omega = 0.75$) in Fig. 2.6. Here we see that at the beginning of the flow significant nucleation occurs immediately and exclusively at the interface between the hot and cool streams. This indicates that the molecular mixing process is dominant. Towards the middle of the domain there is significant nucleation at the interface but also now at the center of the mixing eddies,

away from the jet centerline. This now indicates that large-scale mixing is beginning to rival the molecular mixing taking place at the interface. Finally, the mixing becomes more complete and nucleation events are occurring frequently at locations away from the jet centerline, across the majority of the jet. Here, both mixing mechanisms act. Also of note, is the absence of the "islands" of nucleation seen in case 1. Due to the high super-saturation of the inlet stream, nucleation occurs at the interface immediately, and vapor is converted to particles via nucleation in a nearly steady manner as the flow progresses.

Time-averaged nucleation rate profiles for case 2 are presented in Fig. 2.7. Quantitatively now we see that the high nucleation rates near the nozzle persist downstream. They do not increase significantly as the flow progresses downstream, as was seen in the low saturation ratio case. For case 2a, shown in Fig. 2.7(a), the maximum nucleation rate at $x/D = 5$ is already at the level seen at $x/D = 20$. The results of case 2b, shown in 2.7(b), show similarly high nucleation rates. Intense nucleation occurs at the jet inlet and in the initial shear layer. The increased large-scale mixing does not affect the magnitude of the nucleation rates as it did for the low saturation ratio case. Instead, it acts to spread this intense nucleation across the width of the jet.

The temperature—mass-fraction maps for case 2 are shown in Fig. 2.8. Two trends are immediately evident. First, the nucleation rates are up to four orders of magnitude higher compared to case 1 and second, nucleation is more prevalent throughout the flow in case 2. These are both a natural consequence of the higher amounts of DBP vapor, and the resultant saturation ratio of the jet ($S = 5$). The increased vapor mass-fraction means more collisions and an increased number of stable nuclei. It also means that less mixing is required to achieve the conditions conducive for nuclei growth. The latter is also responsible for the relatively narrow scatter observed in the points in the temperature—mass-fraction map for case 2, compared to case 1. For example, Fig. 2.8 shows that nucleation begins then the temperature is as high as $\theta = 0.9$ whereas in case 1, no nucleation occurs until the flow has cooled to roughly $\theta = 0.6$. The nucleation rate differences between cases 2a and 2b are similar to those observed between cases 1a and 1b. The number of mixing paths leading to nucleation increases as the velocity ratio is increased. However, unlike case 1, all but a few result in particle nucleation.

Nucleation is an exothermic process. Previous research has shown that heat release

in chemically reacting flows slows the growth rate of large-scale, vortical structures and reduces entrainment [65]. Cross-stream profiles of the time-averaged temperature $\overline{\theta}$ are shown in Fig. 2.9. The effects of heat release during the vapor-to-particle conversion can be observed by comparing the low saturation case (1b) with the high saturation case (2b). Generally, higher temperatures are seen in the high saturation case, where nucleation rates are much higher. By $x/D = 10$ in the low saturation case, large-scale mixing has cooled the jet core to approximately 80% of the inlet temperature. In the high saturation case, however, the temperature is still nearly equal to the inlet value. Additionally, downstream the jet width is narrower in the high saturation case. These results indicate that the potential core is much longer when heat release is significant, and that the transition to turbulence is slower. This slower development results in reduced entrainment of cool, vapor-free fluid. Less entrainment as the jet develops means both higher temperatures and concentration values. This tends to favor mixing paths in the upper right corner of the temperature – mass-fraction maps of Fig. 2.8, and accounts for the dissimilar distribution shape as compared to the low saturation case.

Though the high concentration case shows valuable trends, it is actually the least realistic case where we are at the limits of the validity of the set of physical models we use. Very high nucleation rates mean that the use of steady-state nucleation equation may provide an insufficient representation of the nucleation process. The concentration of particles generated is such that the depletion of vapor due heterogeneous condensation, and coagulation start becoming significant. The modeling of these processes are left to future studies.

2.3.5 Particle field

In all of the cases, critical clusters have a size close to $2nm$ when nucleation rates are high, and the overall variation in critical diameter is not very large considering the range of nucleation rates covered. Since homogeneous nucleation is the only phenomenon accounted for, and since the nucleation rates vary on a logarithmic scale, particle concentrations are dominated by particles generated at the highest nucleation rates and particles generated during slower nucleation only account for a small fraction of particles observed at a certain location. As a consequence, aspects related to particle size distribution are not significant in these simulations, and particle mass and number

concentrations behave in a similar manner. Similar to nucleation rates, particles are concentrated in narrow regions. As particle diffusivities are low, their microlevel mixing is expected to remain low even as the flow continues beyond the simulated domain.

Particle number concentrations reflect the nucleation rates experienced in various cases and profiles are presented in Fig. 2.10. In the high saturation ratio flow, case 2 shown in Fig. 2.10(c) and 2.10(d), particle number concentrations reach levels (greater than 10^{13} particles/m^3) that are at the limits of the validity range of purely nucleation-dominated dynamics. In other cases, heterogeneous condensation is not fast enough to cause significant depletion of vapor within the time-scale of the system, and coagulation is not important either. Therefore, the predictions of particle number concentrations would remain unchanged even if these phenomena were also included in the model. Once significant nucleation starts, high particle number concentrations are reached rapidly.

When nucleation takes place at low concentration values or at low nucleation rates, islands of high nucleation rates result in isolated pockets of high particle concentrations. Figure 2.10 shows that at the end of the domain particle number concentrations are affected by the increase in the nucleation rates. When nucleation rates are low, this is dependent on the intensity of mixing by turbulent convection and large differences in particle number concentrations arise as the flow develops. For instance, in the low saturation ratio case, number concentrations on the order of 10^8 particles/m^3 can be observed in a narrow region at the end of the domain in the low mixing flows. In the high mixing flows, values of approximately 10^{10} particles/m^3 can be observed over a much wider area. As with the nucleation rate, though, the distributions for case 2 shown in Fig. 2.10(c) and 2.10(d) show little variation in peak value. The increased mixing intensity merely increases the area in which particles are produced.

The instantaneous nucleation rate, $\log_{10}(J)$, versus critical diameter, d_C, is shown in Fig. 2.11. The plots show that the smallest particles have the highest nucleation rate. Nucleation rates deemed insignificant, those below 10^4 particles/$(m^3 \cdot s)$, are not shown. For case 1, the critical diameters range from $2.1nm$ to $3.2nm$ in the low-mixing flow, shown in Fig. 2.11(a). When mixing is increased (by increasing the velocity ratio in case 1b) the nucleation rate increases and slightly smaller particles are produced. The minimum particle size decreases from $2.1nm$ to below $1.9nm$. Increased mixing speeds the nucleation process by creating conditions that are further from thermodynamic

equilibrium. Under these conditions, an increasing amount of vapor mass must undergo phase to change for equilibrium to return. Here also, molecular clusters have less time to grow before phase change occurs, resulting in smaller product particles. Results from case 2 are shown in Fig. 2.11(b). The increase in saturation-ratio results in both higher nucleation rates and smaller particles. This occurs because higher saturation ratio values represent a further departure from thermodynamic equilibrium. In case 2, the peak nucleation rates are below $d_c = 1.9nm$ under low mixing conditions (case 2a) and below $d_c = 1.8nm$ under high mixing conditions (case 2b). Also, the plot shows that below $J = 10^{17}\ particles/(m^3 \cdot s)$, lie two "legs" in the $\log J$-d_c space. For example, consider $J = 10^{10}$. Figure 2.11(b) suggests that particles of size $d_c = 2.4nm$ and $d_c = 3nm$ are forming at that rate. This can also be deduced from Fig. 2.8(b). If one follows the $\log_{10} J = 10$ iso-line, it is clear that particles form at high temperatures and mass-fractions (near $\theta = 0.75$ and $\phi = 0.8$) as well as low temperatures and mass-fractions (near $\theta = 0.15$ and $\phi = 0.02$). From Fig. 2.2(b), its clear that the former is in the core of the jet while the latter is near the intersection of the jet and the co-flowing stream.

2.4 Conclusions

Homogeneous nucleation during turbulent cooling and mixing was studied with direct numerical simulation (DNS). A three-dimensional planar jet of heated air doped with condensable dibutyl-phthalate (DBP) vapor was adopted as the system. Two different mixing intensities were generated by varying the co-flow velocity and the amount of DBP vapor was varied by increasing the saturation ratio. The simulations provide a demonstration of how nucleation is strongly dependent on the mixing phenomena. Nucleation occurs in limited narrow, regions where molecular mixing takes place and the instantaneous nucleation rates can be very different from the time-averaged ones. Minor changes in the dilution process easily bring about order-of-magnitude changes in nucleation rates and significantly differing nucleation events in the qualitative sense.

It is possible to identify phases in the overall nucleation process, though in some cases they may overlap. First, there can be nucleation right at the inlet of the domain. The nucleation dynamics right at the nozzle outlet was not the scope of these studies

and was treated here as a boundary condition. Second, the initial nucleation evolves along the edges of the unmixed core wedge shear layer. Third, a separate nucleation event takes place, starting away from the centerline, and rapidly spans the whole mixing region. This was the true scope of our studies, and in many situations it is this event that is dominant in the overall particle formation. As the jet and the mixing proceed, maximum instantaneous nucleation rates gradually grow higher. This is the result of the combined action of turbulent convection and molecular mixing. In the temperature–mass-fraction space, this can be seen as broadening of the mixing region towards higher nucleation rates. The rate of this broadening, and thus the rate of increase in the nucleation rates, depends on the intensity of mixing. A source of qualitative differences among calculated cases is the high sensitivity of DBP nucleation at low nucleation rates and at low concentrations. This causes distinct separate islands of nucleation to form. As the level of large-scale mixing increased, so did the nucleation rates. This shows that in case of low inlet DBP concentration the downstream nucleation driven by large-scale mixing far outweighs the initial shear layer nucleation. Additionally, it was seen that as the inlet DBP concentration was increased, the initial shear layer nucleation was comparable in magnitude to the downstream nucleation. Here, increased large-scale mixing did much less to augment nucleation rates.

The T-DBP(v) diagram indicates a pathway for generalizing the simulations. For many cases, the mixing process is sufficiently characterized by constant Reynolds, Prandtl, and Lewis (or Schmidt) numbers. Various combinations of these numbers could be used to generate non-dimensionalized mixing regions in the diagram for various flow situations. The nucleation rates of the species under consideration can then be superimposed on this diagram. Based on the simulations of this study and the observations on the effects of the dilution paths, it is subsequently possible to establish an idea of the nature of the nucleation process in the case under consideration.

The simulations of this paper are more meant to provide a general view of nucleation in turbulent eddies rather than to model a specific system. Since the simulation domain studied was limited in axial length and the simulations were carried out using DNS, it is not possible to make direct comparisons with experimental results, such as those of of Lesniewski and Friendlander (1998). Furthermore, the initial shear layer nucleation was not the focus of these simulations. However, one observation concerning

the experiments of Lesniewski and Friedlander is worth pointing out. When the DBP concentration was large enough, they observed a bimodal particle size distribution. The larger particles correspond to particles that formed in the initial shear layer and later grew by heterogeneous condensation, while the small mode was believed to have formed outside the shear layer. This observation agrees with our simulations where two distinct nucleation events were observed: initial shear layer nucleation along the unmixed wedge and nucleation later on when larger eddies have formed and turbulent mixing begins to dominate.

One of the advantages of the modeling methodology is that it is relatively straightforward to include additional phenomena, such as molecular cluster dynamics, heterogeneous condensation and coagulation. The simulation of increased turbulence and larger domains is also possible, though the computational demands are much greater and the range of computationally feasible Reynolds numbers is limited. In any case, the current simulations reveal many features of turbulent nucleation that are significant even when additional phenomena are involved as well.

Case	DBP Mass-fraction	Saturation ratio, S	Velocity ratio, U_o/U_∞
1a	$Y_{DBP} = 0.003$	1	1.82
1b	$Y_{DBP} = 0.003$	1	3
2a	$Y_{DBP} = 0.015$	5	1.82
2b	$Y_{DBP} = 0.015$	5	3

Table 2.1: Flow and jet parameters

Saturation mole fraction	$x_{sat} = exp(21.497 - 11497/T)$
Surface tension [N/m]	$\sigma = 0.0353 - 0.0000863(T - 273.16)$
Condensed phase density $[kg/m^3]$	$\rho_c = 1063 - 0.826(T - 273.16)$
Vapor diffusivity $[m^2/s]$	$\mathcal{D}_m = 3.984 \times 10^{-6}(T/273.16)^{1.5}$

Table 2.2: Physical properties of DBP adopted in this study.

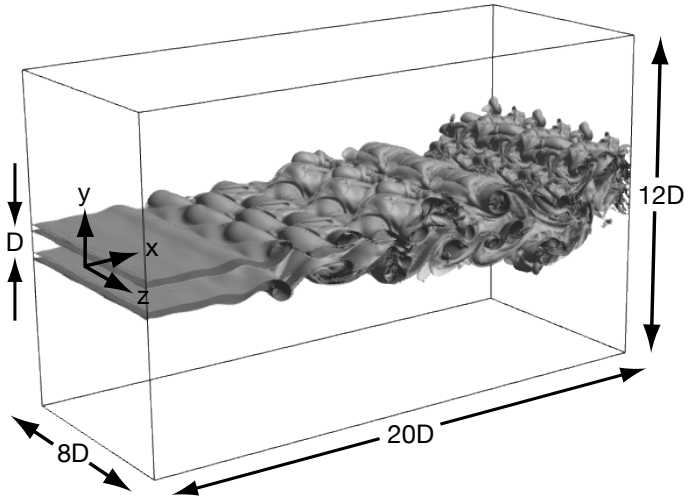

Figure 2.1: Flow configuration.

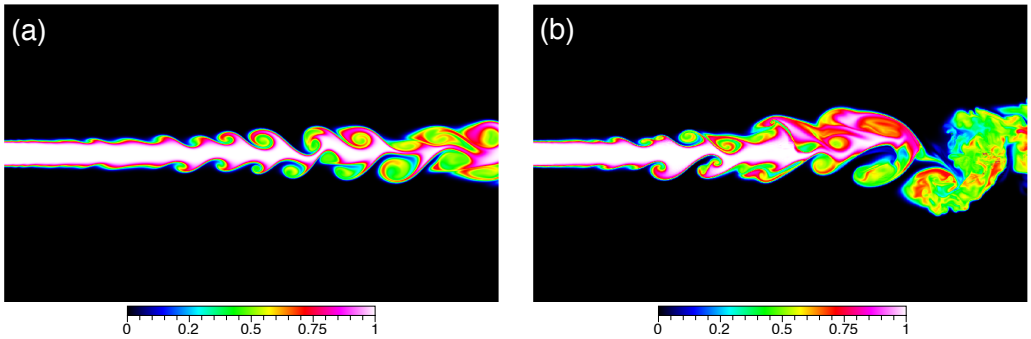

Figure 2.2: Instantaneous contours of the normalized temperature (θ) at $z = 0$: (a) Case 1a; (b) Case 1b.

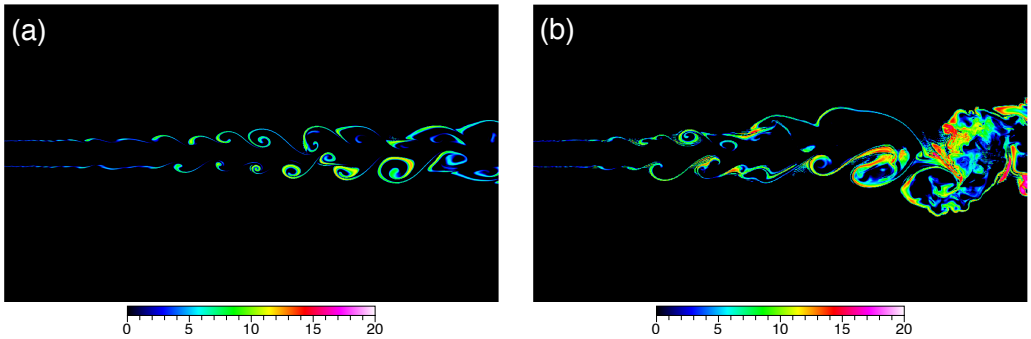

Figure 2.3: Instantaneous contours of the nucleation rate ($\log_{10}(J)$) at $z = 0$: (a) Case 1a; (b) Case 1b.

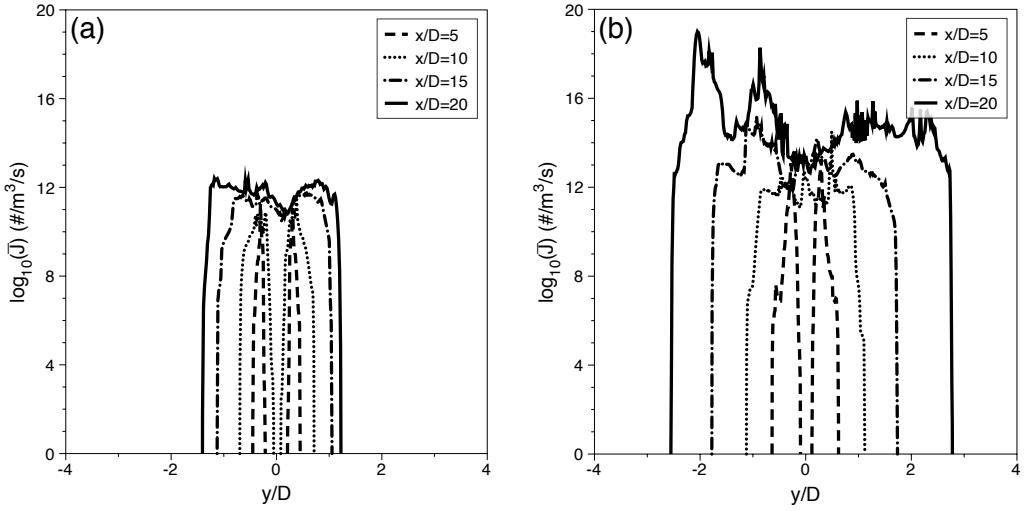

Figure 2.4: Cross-stream profiles of the time-averaged nucleation rate ($log_{10}(\overline{J})$) for (a) Case 1a; (b) Case 1b.

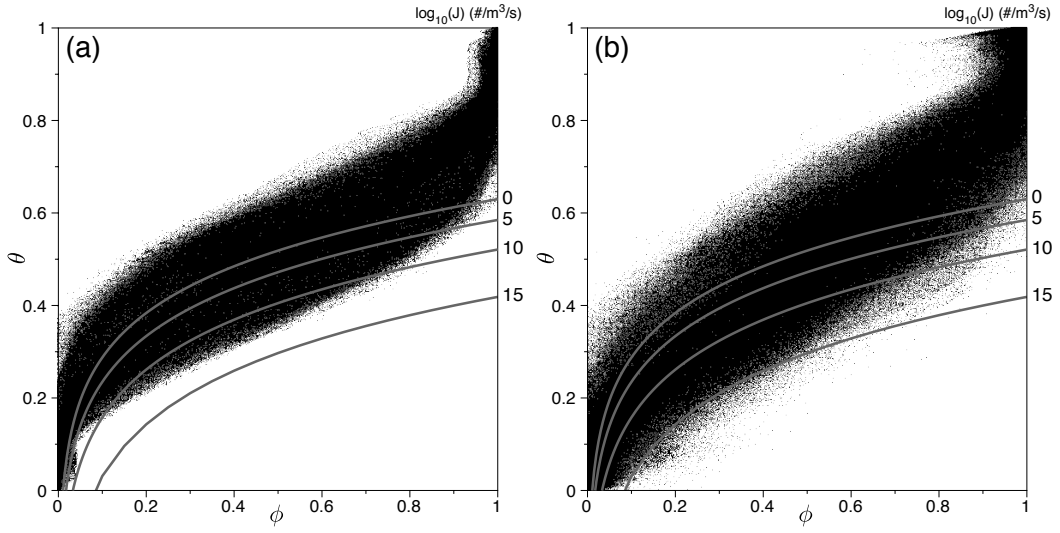

Figure 2.5: Temperature – mass-fraction ($\theta - \phi$) maps with lines of constant nucleation rate ($\log_{10}(J)$) for (a) Case 1a; (b) Case 1b.

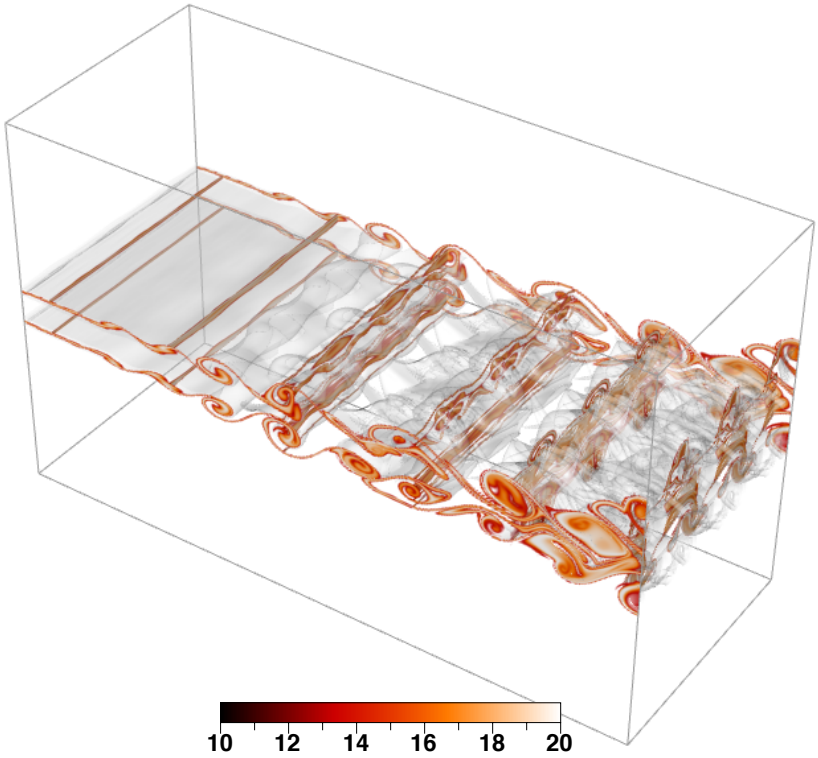

Figure 2.6: Contours of the nucleation rate ($log_{10}(J)$) shown with iso-surfaces of vorticity ($\Omega = 0.75$) for Case 2a.

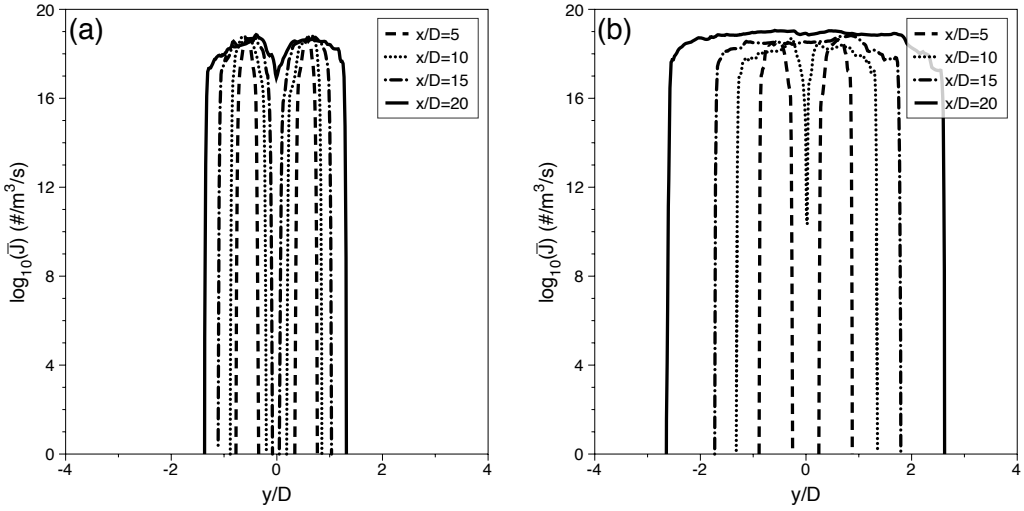

Figure 2.7: Cross-stream profiles of the time-averaged nucleation rate ($log_{10}(\overline{J})$) for (a) Case 2a; (b) Case 2b.

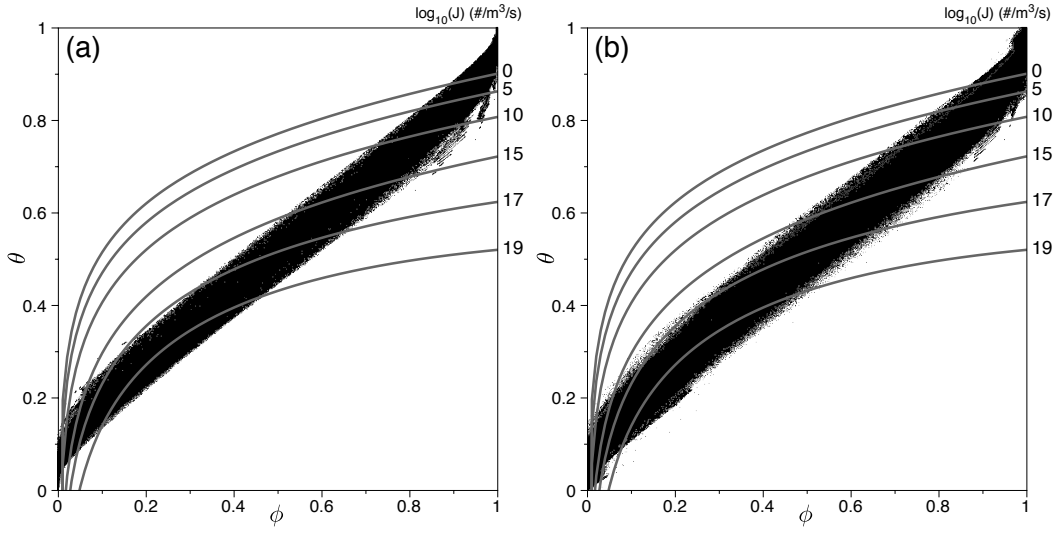

Figure 2.8: Temperature – mass-fraction ($\theta - \phi$) maps with lines of constant nucleation rate ($\log_{10}(J)$) for (a) Case 2a; (b) Case 2b.

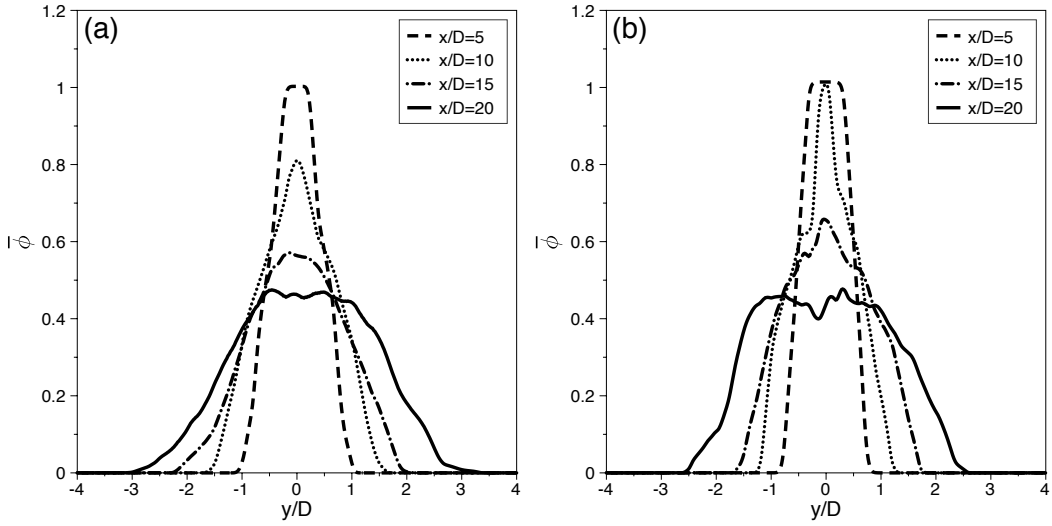

Figure 2.9: Cross-stream profiles of the time-averaged, normalized temperature ($\overline{\theta}$) for (a) Case 1b; (b) Case 2b.

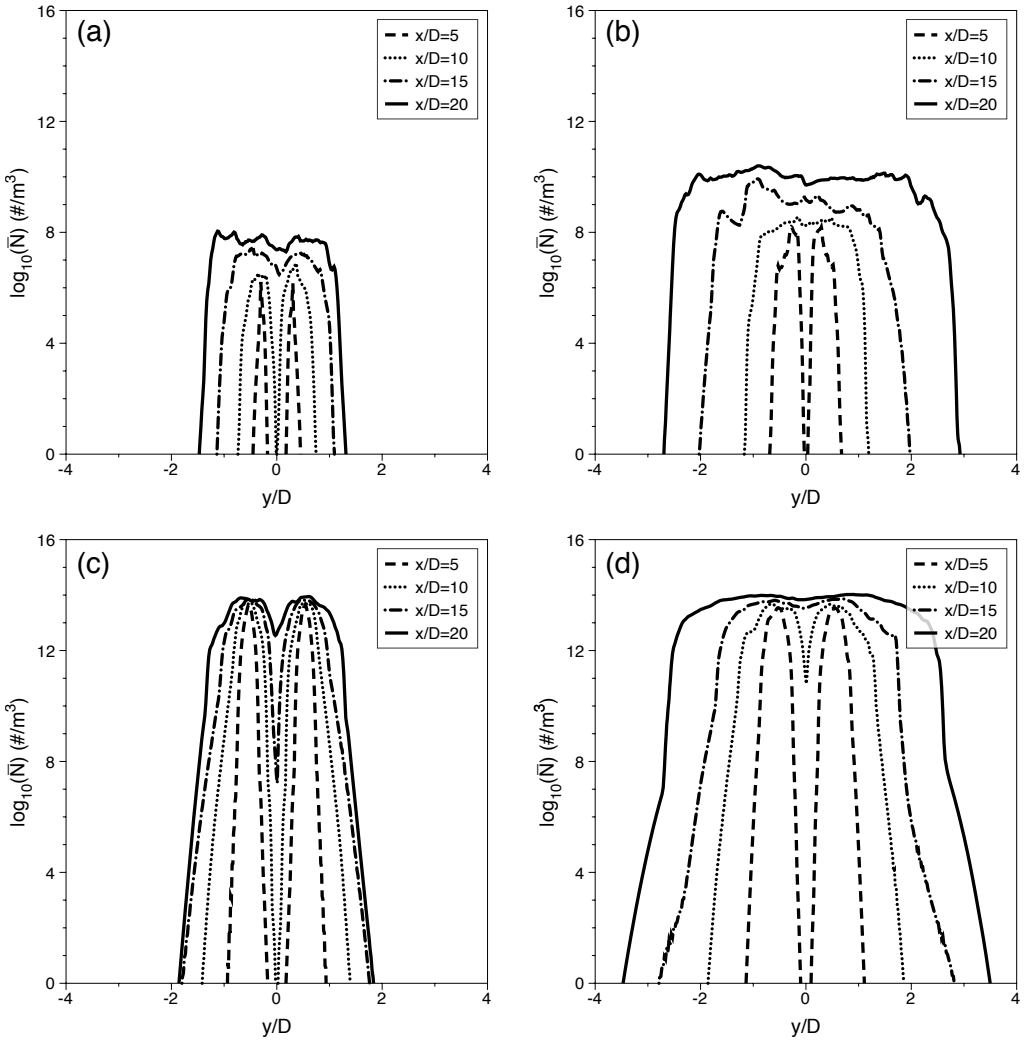

Figure 2.10: Cross-stream profiles of the time-averaged number concentration ($log_{10}(\overline{N})$) for (a) Case 1a; (b) Case 1b; (c) Case 2a; (d) Case 2b.

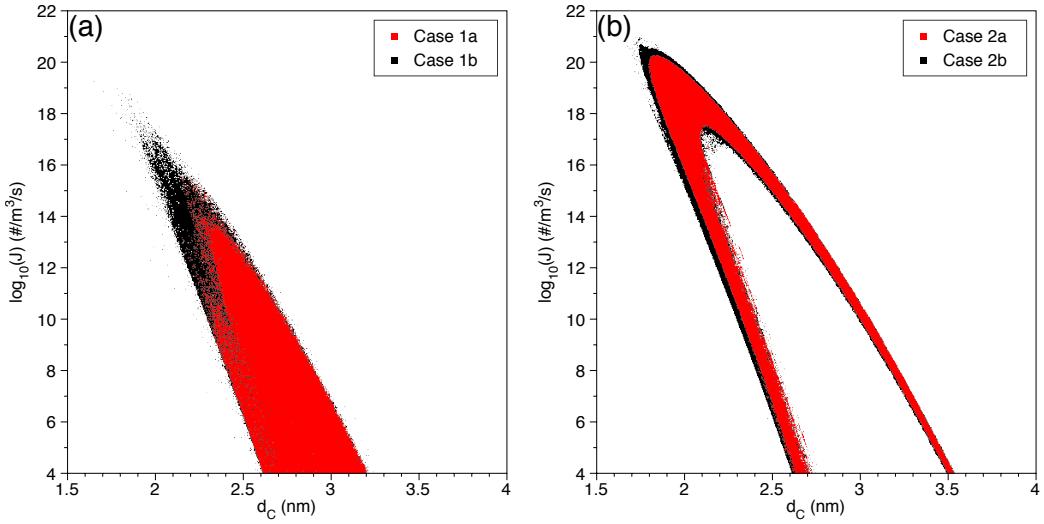

Figure 2.11: Scatter plots of the nucleation rate, $\log_{10}(J)$, as a function of critical diameter, d_c (nm).

Chapter 3

The effects of Lewis number on homogeneous nucleation

3.1 Introduction

Homogeneous nucleation is a phenomenon at work in such varied processes as combustion, nanoparticle synthesis and atmospheric particle dynamics. It has been the subject of a number of studies, most notably the work of Lesniewski and Friedlander (1995, 1998), who studied the homogeneous nucleation of dibutyl-phthalate (DBP) in shear flows [51, 50]. To augment their experimentation, simple computations were carried out, though to make these computationally amenable the thermal and vapor diffusivities were assumed to be equal. This would imply a Lewis number of unity, $Le = 1$. Many other studies have adopted this or similar assumptions [53, 39, 52]. Recent studies have incorporated probabilistic methods to simplify the simulation of homogeneous nucleation in turbulent flow. The work of Di Veroli and Rigopolous (2011) utilized a transported probability density function (PDF) method to capture the transport of temperature, mass-fraction and product particles in a planar jet [66]. The mixing model employed to simulate the micro-mixing of the scalars is the interaction by exchange with the mean (IEM) model. In their work, the diffusion of temperature and mass-fraction are treated identically, which is analogous to the $Le = 1$ assumption. In fact, they treat both the large-scale and small-scale mixing exactly the same. Indeed, it has been suggested that the effect of a non-unity Lewis number may play an important role in

gas-to-particle conversion [67, 68].

Direct numerical simulation (DNS) is used here as it involves no inherent models [31]. In this framework, no assumptions must be made about the mixing process and most importantly the thermal and concentration fields are fully resolved, as is the dilution process. This makes investigation of the validity of the $Le = 1$ assumption possible and is the goal of this work. Dibutyl-pthalate (DBP) is used here as it has been utilized in many previous experimental and simulation studies, and its large size is similar to large organic compounds of interest in combustion and atmospheric studies.

3.2 Formulation

The flow and enthalpy fields are described by the Navier-Stokes equations for compressible, non-isothermal flow, which yield the the velocity vector, $u_i(\bar{x}, t)$, the fluid pressure, $p(\bar{x}, t)$, the fluid density, $\rho(\bar{x}, t)$, and the enthalpy, $h(\bar{x}, t)$. The ideal gas law closes the system of equations. The DBP vapor mass fraction transport is modeled as a conserved scalar, $Y(\bar{x}, t)$, with a nucleation sink term $\dot{\omega}_{nucl}$. Utilizing the expression $dh = C_P dT$ to relate the temperature and enthalpy, the non-dimensionalized forms of the energy and species equations are given by

$$\frac{\partial \rho T}{\partial t} + \frac{\partial \rho u_j T}{\partial x_j} = \frac{\partial}{\partial x_j}\left(\frac{\mu}{RePr}\frac{\partial^2 T}{\partial x_j}\right) \tag{3.1}$$

$$\frac{\partial \rho Y}{\partial t} + \frac{\partial \rho u_j Y}{\partial x_j} = \frac{\partial}{\partial x_j}\left(\frac{\mu}{Re(Le \cdot Pr)}\frac{\partial Y}{\partial x_j}\right) - \frac{D}{\rho_o u_o Y_o}\dot{\omega}_{nucl} \tag{3.2}$$

where μ is the non-dimensional viscosity, D, ρ_o, u_o and Y_o are the reference length, density, velocity and mass-fraction values, respectively. Re is the Reynolds number, Pr is the Prandtl number and Le is the Lewis number. The Lewis number is simply the ratio of the thermal diffusivity to the mass diffusivity, which can be written as $Le = Sc/Pr$, where Sc is the Schmidt number. Assuming a Lewis number of unity means that these diffusivities are equal. This would imply that the temperature (which may also be modeled as a conserved scalar) and concentration fields would diffuse identically.

Nucleation is modeled following the kinetic approach of Girshick and Chiu [57]. This method applies a correction to the classical nucleation expression. Nucleating particles

have a critical diameter, d_C given by:

$$d_C = \frac{4\sigma v_m}{k_B T \ln(S)}, \tag{3.3}$$

where σ is the surface tension of the condensed species, v_m is its molecular volume, k_B is the Boltzmann constant, T is the temperature, and S is the saturation ratio of the vapor. Using the self-consistent correction of Girshick and Chiu, the nucleation rate J can be expressed as:

$$J = \frac{1}{S}\frac{(\rho Y)^2}{\rho_c m_m}\sqrt{\frac{2\sigma}{\pi m_m}}\exp\left(\frac{\sqrt[3]{36\pi v_m^2}\sigma}{k_B T} - \frac{\pi\sigma d_C^2}{3k_B T}\right) \tag{3.4}$$

where m_m is the mass of a molecule of condensable species and ρ_c is its condensed phase density. The sink term for nucleation $\dot{\omega}_{nucl}$ is the nucleation rate J multiplied by the empirical correction factor c_{nuc} and the mass of the nucleating cluster:

$$\dot{\omega}_{nucl} = c_{nuc}\frac{\pi}{6}\rho_c d_C^3 J. \tag{3.5}$$

3.3 Results

3.3.1 Flow configuration

The flow of interest is a three-dimensional heated planar jet comprised of a mixture of DBP vapor at $T_o = 400K$ issuing into a co-flow of approximately room-temperature ($T_\infty = 300K$) air. The jet issues from a nozzle of diameter D. At the inlet, the jet has a velocity u_o, density ρ_o, viscosity μ_o and a temperature T_o. The Reynolds number of the jet is $Re = \rho_1 u_1 D/\mu_1 = 4000$. The velocity of the co-flowing stream, u_∞, is varied to generate two levels of mixing: a low mixing case where $u_\infty/u_o = 0.55$ and a high mixing case in which $u_\infty/u_o = 0.33$. The inlet DBP vapor concentration, Y_o, is defined such that the initial saturation ratio is $S = 1$. For the system considered here the lewis number is $Le = k/(C_p\mathcal{D}) = 5.4$. Lewis numbers greater than unity indicate that thermal diffusion is greater than species diffusion. This will comprise the baseline case (1), for which case 1a will incorporate the low mixing conditions and case 1b will be carried out with the high mixing conditions. To assess the role of non-unity of Lewis number, we calculate a second case (2) where we set Le to unity, ie. $Le = 1$, by setting DBP vapor diffusivity equal to the thermal diffusivity of nitrogen instead of using the actual value.

3.3.2 Physical assumptions

Nucleation is inherently a non-equilibrium process. Clusters of molecules grow in size until the cohesive forces of the cluster outweigh the kinetic energy of the colliding molecules [17]. At this point, the cluster are said to be stable nuclei. As the nucleation rate expression of CNT is derived for steady-state conditions, the time scale of fluid and scalar fluctuations should be less than that required to reach steady-state nucleation. We have carried out temporal calculations that compute this molecular growth mechanism according to the work of McMurry [69, 70]. The conclusions of that work suggest that the flow may be considered "frozen" while nucleation is occurring, and this assumption has been used in other work [66]. The bulk properties of DBP are used in accordance with CNT. This includes the density of DBP and the surface tension. We adopt the expression given by $\sigma = 0.0353 - 0.0000863(T - 273.26)$ for the surface tension [58]. Additionally, the use of CNT often involves an empirical correction factor and in this work the value is taken to be $c_{nuc} = 3.2 \times 10^{-4}$, specific to DBP [59].

3.3.3 Numerical specifications and parameters

The transport equations are integrated using a hybrid MacCormack-based finite-difference scheme which is second order accurate in time and fourth order accurate in space [64, 71]. A domain size of $20D \times 12D \times 8D$ is covered by grid consisting of $1280 \times 512 \times 480$ in the x, y and z directions, respectively. Boundary conditions at the inflow plane $x/D = 0$ are prescribed in the form of velocity, enthalpy, and mass-fraction profiles as functions of y. Zero derivatives are imposed at the y-boundaries and periodicity is prescribed in the z-direction. Non-reflecting exit boundary conditions are used at the exit plane, $x/D = 20$, which allows acoustic pressure waves to exit the domain without disturbing the flow field [72]. The governing equations are integrated (in time) and instantaneous and mean quantities are computed. The mean quantities are denoted with an over-bar.

3.3.4 Fluid and scalar dynamics

The temperature and vapor mass-fraction fields largely determine the nucleation dynamics in a flow as seen by their non-linear relationship to the nucleation rate in eq. 3.4. For ease of presentation and comparison, the temperature and DBP mass fraction

are normalized via $\theta = (T - T_\infty)/(T_o - T_\infty)$ and $\phi = (Y/Y_o)$, respectively. Cross-stream profiles of the time-averaged temperature $\overline{\theta}$ and DBP mass fraction $\overline{\phi}$ are shown in fig. 3.1 for case 1 and case 2 under the high mixing conditions. Panels (a) and (b) show the temperature field evolution. As the flow develops, it cools and the temperature is diluted. This dilution has decreased the jet centerline temperature to approximately 50% of the inlet value by $x/D = 20$. The temperature fields for case 1 and case 2 are extremely similar as the same thermal diffusivity has been used for both. The evolution of the concentration field is shown in panels (c) and (d). The mass-fraction is diluted similar to the temperature as the flow develops. As the vapor in the $Le = 1$ case has an artificially higher diffusivity (equal to the thermal diffusivity) the mass-fraction diffuses exactly as the temperature does. In both cases, the centerline mass-fraction has dropped to half its inlet value by the end of the domain. Though the difference in the temperature and concentration fields when $Le = 1$ may appear insignificant on average, the nucleation source term is highly non-linear; the nucleation calculation at any one instant in time is extremely sensitive to the local variation in the temperature and concentration fields.

3.3.5 Nucleation dynamics

The amount of super-saturation of the DBP vapor, quantified by the saturation ratio S, is the driving force behind nucleation. The saturation ratio is defined as the ratio of the vapor partial pressure to its saturation pressure. When high saturation ratios (above unity) occur, the fluid-vapor system has strayed from thermodynamic equilibrium. The restore equilibrium, vapor mass moves from the gas to liquid or solid phase via the nucleation process. Higher saturation ratios thus require higher nucleation rates to restore equilibrium. Values of the calculated saturation ratio are superimposed upon iso-surfaces of vorticity under the high mixing conditions in fig. 3.2 to illustrate how the $Le = 1$ assumption affects saturation. In case 1, shown in fig. 3.2(a), the saturation ratio starts near zero at the inlet. As the flow develops and the hot and cool streams mix, the saturation ratio rises significantly. The maximum values are seen near the end of the domain, where turbulent mixing brings hot, vapor-laden fluid in contact with cooler, vapor-free fluid. This trend indicates that as the flow develops and turbulent mixing increases, the saturation ratio increases substantially. Figure 3.2(b) shows a

very different trend for the $Le = 1$ case. Here, high saturation ratio values occur almost immediately. These high values continue as the flow develops, decreasing slightly at the point the potential core collapses. This implies that molecular mixing indeed has a large effect on saturation. As saturation is the driving force behind nucleation, the $Le = 1$ assumption will affect calculated nucleation rates greatly.

3.4 Conclusions

Direct numerical simulation of the homogeneous nucleation of dibutyl-pthalate (DBP) was carried out. This work investigated the effects of both small-scale (molecular) and large-scale (convective) mixing. The effects of molecular mixing were investigated by varying the diffusivity of the vapor. The Lewis number (Le) is the ratio of thermal to vapor mass diffusivity. By setting the vapor diffusivity equal to the thermal diffusivity we simulated a case where $Le = 1$. This scenario is compared to a case where the correct diffusivities are used, which is $Le = 5.4$. The effects of large-scale mixing were investigated by varying the velocity ratio between the jet and co-flow.

Our results show that assuming $Le = 1$ can lead to calculated maximum nucleation rates that are three to five orders of magnitude lower than reality. Additionally, when the $Le = 1$ assumption is made, the particles produced at the highest nucleation rates are up to 15% larger. This is significant as the size of the particles produced at the highest nucleation rates often dominates the overall size distribution of particles. This means that any size distribution calculated under the $Le = 1$ assumption may be erroneous. These results show that small-scale mixing affects both the rate at which particles are produced and their size. As large-scale, convective mixing is increased, nucleation rates rise sharply in the $Le = 5.4$ case. In the $Le = 1$ case, an increase in large-scale mixing does not affect the results significantly. These results imply that large scale mixing does indeed affect nucleation. It also implies that when the $Le = 1$ assumption is made, the effects of large-scale mixing are not realized. These results bear in mind the DBP molecule is large and the simulated relative changes in vapor pressure are fairly high. The effect of non-unity Le is therefore stronger that it would be for some more diffusive species or with less sensitive nucleation kinetics.

Our results clearly show that both large-scale and molecular mixing have a significant

effect on nucleation. This work therefore shows that when probabilistic methods are used the mixing models should differentiate molecular mixing and turbulent or sub-grid scale mixing. These phenomena must be treated separately for the effects of mixing on nucleation to be fully realized.

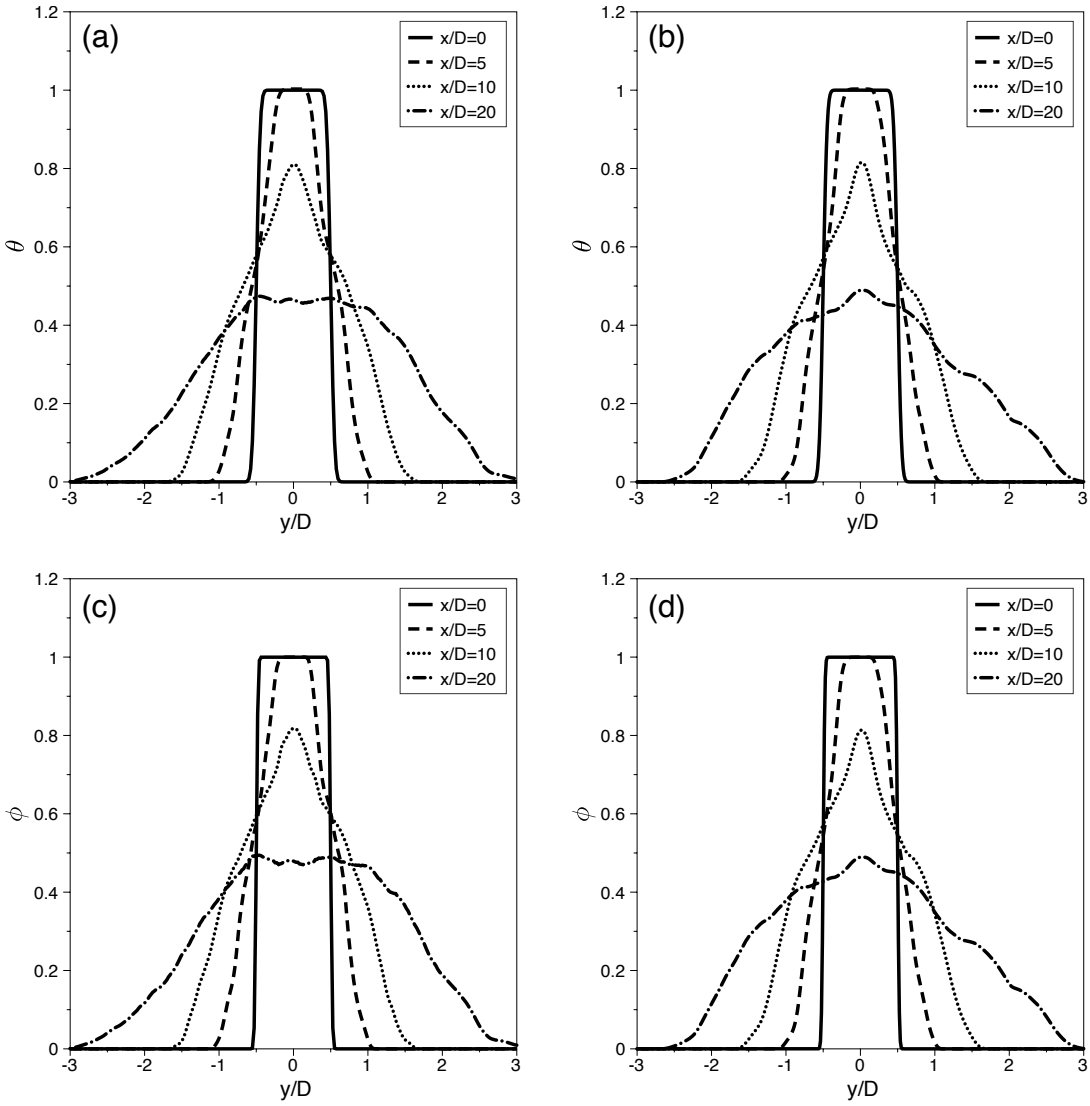

Figure 3.1: Cross-stream profiles of the normalized temperature, θ, and DBP mass-fraction, ϕ: (a) $\overline{\theta}$ case 1; (b) $\overline{\theta}$ case 2; (c) $\overline{\phi}$ case 1; (d) $\overline{\phi}$ case 2.

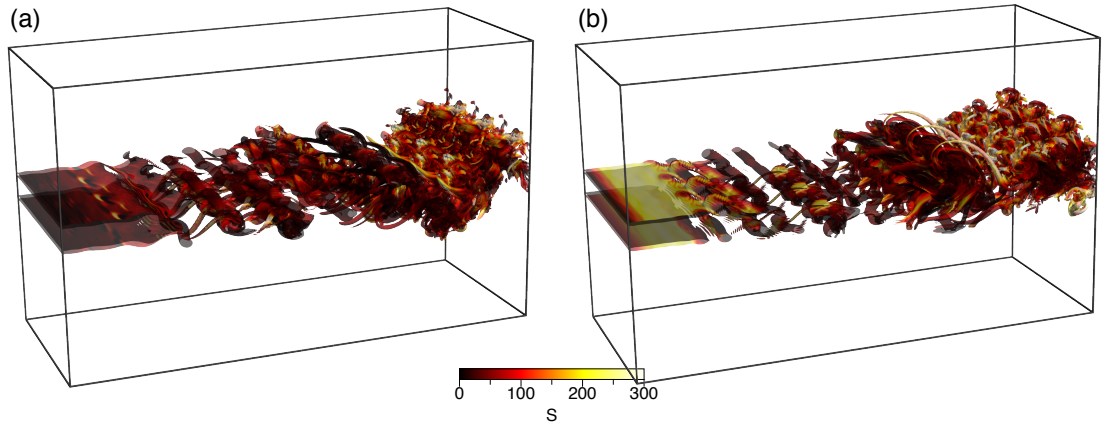

Figure 3.2: Values of the saturation ratio, S, imposed upon iso-surfaces of vorticity, $\Omega = 1.75$.

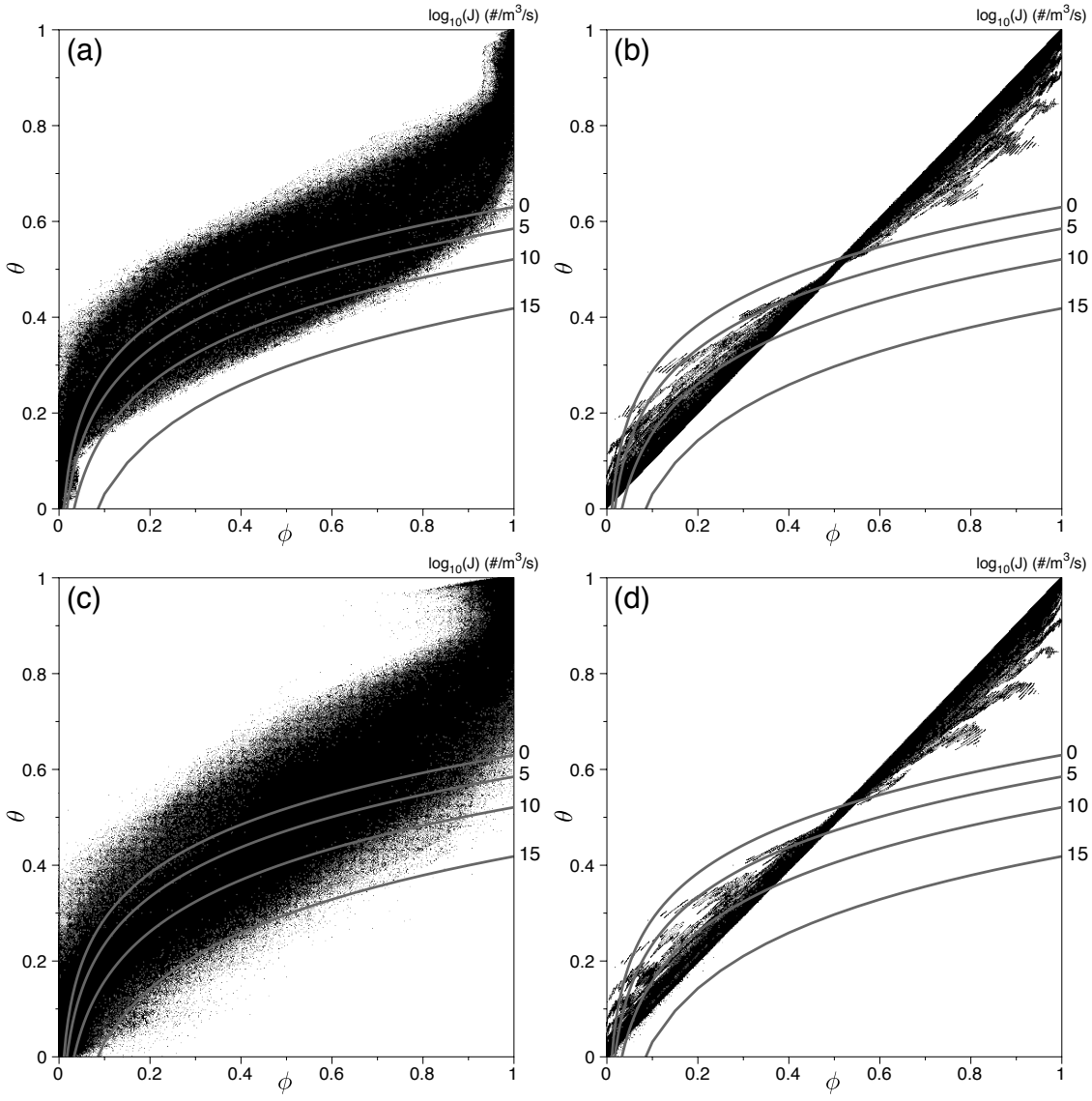

Figure 3.3: Temperature – mass-fraction scatter plots: (a) case 1a; (b) case 1b; (c) case 2a; (d) case 2b.

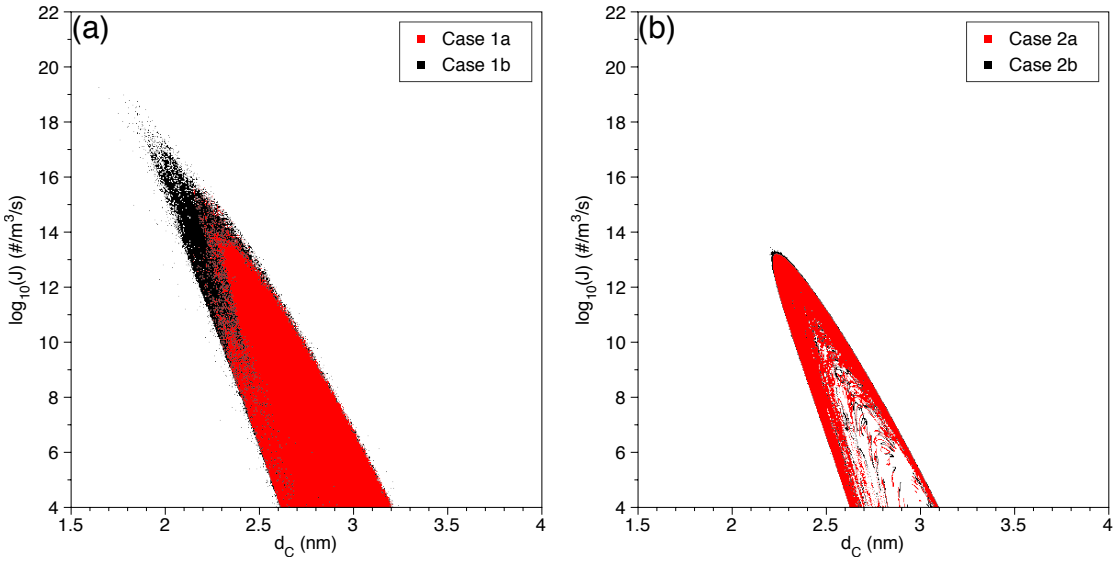

Figure 3.4: Nucleation rate – critical diameter scatter-plots: (a) case 1; (b) case 2

Chapter 4

The effects of unresolved scalar fluctuations during homogeneous nucleation

4.1 Introduction

Nucleation is understood to play a prominent role in such physical processes as condensation and evaporation, crystallization and the deposition of thin films, and its theoretical underpinnings were described as early as the late nineteenth century in Gibbs' theoretical thermodynamic works. While nucleation mechanisms have been given considerable attention in past studies, there are still aspects of the processes, including the effects of fluid turbulence, that are not yet completely understood [73, 74]. A better understanding of the interactions between the fluid dynamics and the nucleation physics is key to understanding particle nucleation and improved modeling of vapor-phase particle formation and growth in complex flows [8, 9, 7].

A number of experiments have been carried out that study the formation of nanoparticles via nucleation. Lesniewski and Friedlander (1998) investigated the nucleation and subsequent growth of dibutyl-phthalate (DBP) particles in a free turbulent jet [50]. Particle size distributions measured as a function of spatial location and scaling laws were developed that related final aerosol concentrations to initial flow velocity. Hämeri and

Kulmala (1996) also studied the homogeneous nucleation of DBP, though in laminar flow diffusion cloud chambers [75]. While some work has indeed explored DBP nucleation under turbulent conditions [76, 77, 78, 79, 80], the majority of research has been confined to laminar flow systems, leaving the effects of fluid turbulence and small-scale interactions to speculation. Simple calculations were first used to explore the effects of turbulence on homogeneous nucleation and to relate the location at which nucleation is most prevalent to flow characteristics. Lesniewski and Friedlander (1995) looked into the effects of turbulence on nucleation by carrying out calculations for a jet in which the Lewis number was unity (thermal and mass diffusivities are equal) [51]. They posited that turbulent fluctuations broadened nucleation across the shear layer as a result of pockets of un-mixed, relatively hot fluid being injected into cooler fluid. Additionally, they concluded that while turbulence greatly affected the distribution of the product particles, it had a less significant effect on the rate at which these particles were formed. The assumption that nucleation occurs exclusively in the shear layer contradicts the work of Clement (1985), which postulates that the Lewis number of unity assumption is inadequate for aerosol formation [81]. And more recently, it has been shown that the effects of turbulent fluctuations on nanoparticle growth in turbulent shear flows are indeed significant [56, 82].

Our intent is to elucidate the effects of small-scale or unresolved interactions on particle nucleation. To accomplish this we perform direct numerical simulation (DNS) of DBP nucleation in a turbulent wake. We then use the DNS data to perform an *a priori* analysis on the effect that the unresolved scalars — temperature and DBP mass-fraction — have on the nucleation rate. As the scope is this work is limited to the modeling and simulation of nucleation, only the scalars themselves are filtered and analyzed. This is in contrast to more complicated physical quantities often analyzed in experiment or theoretical studies on how fluctuations affect nucleation [83]. We utilize a spatial filter of varying width to separate the quantities into their means and fluctuations, compare the nucleation rate based on the exact and mean quantities, and evaluate unresolved scale quantities in a statistical manner. From this analysis, the effects of small-scale interactions (inherent in turbulent flow) on the nucleation are readily apparent.

4.2 Formulation

4.2.1 Fluid transport

The flow under consideration is governed by the compressible Navier-Stokes equations in which the fundamental transport variables are the velocities $u_i(x_i, t)$ in the x_i direction, pressure $p(x_i, t)$ and the total enthalpy $h(x_i, t)$. The conservation equations for the aforementioned variables are

$$\frac{\partial \rho}{\partial t} + \frac{\partial \rho u_j}{\partial x_j} = 0, \tag{4.1}$$

$$\frac{\partial \rho u_i}{\partial t} + \frac{\partial \rho u_i u_j}{\partial x_j} = -\frac{\partial p}{\partial x_i} + \frac{\partial \tau_{ij}}{\partial x_j} \tag{4.2}$$

and

$$\frac{\partial \rho h}{\partial t} + \frac{\partial \rho u_j h}{\partial x_j} = \frac{\partial}{\partial x_j}\left(\frac{k}{C_p}\frac{\partial h}{\partial x_j}\right) \tag{4.3}$$

where τ_{ij} is the viscous stress tensor for a Newtonian fluid, k is the thermal conductivity and C_p is the specific heat. The system is closed using the ideal gas equation of state, $p = \rho RT$, where R is the gas constant and T is the temperature, obtained via $dh = C_p dT$.

4.2.2 Species Transport

The flow consists of two gases, a condensible vapor and a non-condensible carrier, or background gas. The mass-fraction transport equation is given by

$$\frac{\partial \rho Y_i}{\partial t} + \frac{\partial u_j \rho Y_i}{\partial x_j} = \frac{\partial}{\partial x_j}\left(\mathcal{D}_i \frac{\partial \rho Y_i}{\partial x_j}\right) - \dot{\omega}_N, \tag{4.4}$$

where Y_i is the mass fraction of species i, $\mathcal{D}_i$ is the diffusion coefficient and $\dot{\omega}_N$ is the species sink due to particle nucleation. This term accounts for the conversion of the vapor to particles and will be zero for the carrier gas.

4.2.3 Particle nucleation

One of the more commonly used approaches to nucleation modeling is classical nucleation theory (CNT). Given the pressure, temperature, species concentration and material properties, CNT predicts a particular particle formation rate (particles $/(m^3 \cdot s)$).

The use of CNT is attractive as its mathematical simplicity renders itself amenable to use in large-scale simulations and has had success predicting nucleation rates observed in experiment [17]. Using CNT, and the correction factor of Girshick and Chiu (1990) [57], the rate of particle formation is given by

$$J_{kin} = \frac{(\rho Y)^2}{\rho_c m_m}\sqrt{\frac{2\sigma}{\pi m_m}}\frac{1}{S}\exp\left(\frac{\sqrt[3]{36\pi v_m^2}\sigma}{k_B T} - \frac{\pi\sigma {d_c}^2}{3k_B T}\right). \tag{4.5}$$

Here, ρ_c is condensed-phase density of DBP, σ is the surface tension, m_m, is the species molecular mass, v_m is the volume of a molecule, k_B is the Boltzmann constant, d_c is the critical diameter (or the diameter of the nucleating particle according to the Kelvin relationship [17]) given by

$$d_c = \frac{4\sigma v_m}{k_B T \ln(S)}, \tag{4.6}$$

and S is the saturation ratio, defined as the ratio of the vapor partial pressure of species i to the equilibrium (or saturation) vapor pressure at a given temperature, and given by

$$S = \frac{\rho RT}{p_{mix}}\frac{MW_{mix}}{MW_i}\frac{Y_i}{x_{sat}}, \tag{4.7}$$

where p_{mix} is the local, thermodynamic mixture pressure, MW_{mix} is the mixture molecular weight and x_{sat} is the saturation mole fraction for species i. The rate of aerosol mass being produced is obtained by multiplying the nucleation rate J_{kin} (particles/$(m^3 \cdot s)$) by the mass of a nucleating droplet (kg),

$$\dot{\omega}_N = c_{nuc}\frac{\pi}{6}\rho_c {d_c}^3 J_{kin} \tag{4.8}$$

where c_{nuc} is a material-specific, empirical correction factor. Such factors are used to account for both inaccurate material properties and insufficient nucleation models and are applied to nucleation rate expressions to match observed rates for a given species [59, 84].

4.3 Results

4.3.1 Flow configuration

The flow of interest is a three-dimensional planar wake. The plane wake is comprised of gas issuing through nozzle, or slot, of height D at a velocity of U_o and temperature

T_o into a co-flowing stream with velocity U_∞ and temperature T_∞. The velocity ratio is $U_o/U_\infty = 0.25$, and the Reynolds number, based on the velocity difference $\Delta U = U_\infty - U_o$ is $Re = \rho_o \Delta U D/\mu_o = 4000$. The gas is comprised of a mixture of dibutylphthalate (DBP) and nitrogen. The mass fraction of the condensible vapor DBP is $Y_{DBP} = 7.09 \times 10^{-3}$, which is chosen to achieve a saturation ratio at the inflow plane of $S_o = 1$. The temperatures are $T_o = 400K$ and $T_\infty = 300K$ and the saturation ratio at the nozzle, or the inflow plane, is $S_o = 1$. The Lewis number is $Le = k/(C_p \mathcal{D}) = 5.43$, evaluated at the reference conditions, namely T_o. Lewis numbers greater than unity indicate that thermal diffusion is greater than species diffusion.

4.3.2 Physical assumptions

Nucleation is an unsteady, non-equilibrium, process. Homogeneous nucleation theory suggests that molecular clusters grow in size due to collisions. The clusters are said to be stable, and nucleate at the critical diameter, d_c when the surface energy of the resultant cluster is greater than the kinetic energy of the collisional pairs [17]. The time needed for this "nucleation process" is finite and may interact the with the time-scales of the flow [85]. We have performed temporal simulations that compute molecular-cluster growth using the collision-based method following the work of McMurry [69, 70]. The results of these simulations show that particles of the size produced in this work (less than approximately $3nm$) form stable clusters within $10^{-9}s$. The convective time scale in this work, based upon the Kolmogorov length scale, is much larger, approximately $10^{-4}s$. These results suggest that the nucleation time-scale is sufficiently fast such that the flow can be considered to be "frozen" while nucleation occurs. A recent work utilized this frozen eddy assumption [66]. The heat release is taken into account by calculating the enthalpy based upon the DBP vapor mass fraction as nucleation converts vapor to particulate mass. This does not, however, take into account the heat released during the nucleation process. This approach alters the temperature field based upon the change in mass-fraction, which in turn affects the calculated nucleation rate. Though this heat release is accounted for, it is not significant under these flow conditions as relatively little vapor mass is converted to particles via nucleation.

The assumptions inherent in CNT and the kinetic model of [57] are acknowledged and subsequently adopted in this work. Namely, these involve the nature of cluster

formation at the molecular level. It is assumed that the molecular clusters that create nuclei are homogeneous, spherical, contain no charge and retain the same properties of the bulk material [57]. The bulk properties of DBP are used here in accordance with CNT. This includes the density of DBP and the surface tension. We adopt the expression given by Nguyen, *et al.* (1987) for the surface tension, $\sigma = 0.0353 - 0.0000863(T - 273.26)$ and saturation mole fraction, $x_{sat} = \exp(21.497 - 11497/T)$ [58]. Of note, the expression utilized for the saturation mole fraction leads to the appearance of an exponential term in the denominator of Eq. 4.7. The use of a bulk value for the surface tension at the nano-scale becomes suspect [17]. Indeed, utilization of a size-dependent surface tension has been shown to affect nucleation rates for certain chemical species, though these expressions involve assumptions of their own [86, 87]. Additionally, while evaporation or "de-nucleation" can often be significant [88], it is not considered here. Finally, the use of CNT often involves an empirical correction factor. In this work the value is taken to be $c_{nuc} = 3.2 \times 10^{-4}$, specific to DBP [59].

4.3.3 Numerical specifications and parameters

The transport equations are integrated using a hybrid MacCormack-based finite-difference scheme which is second order accurate in time and fourth order accurate in space [64, 71]. A domain size of $16D \times 10D \times 4D$ is covered by a grid consisting of $1152 \times 704 \times 288$ points in the x, y and z directions. A schematic is shown in Fig. 4.1. As this DNS simulation is used as a baseline in this work, the length scale of the smallest turbulent motion (Kolmogorov microscale) must be resolved. Here, an approximate of the Kolmogorov length scale $\eta = Re^{-1/4}D$ is used [89]. Using the parameters of this flow, the Kolmogorov length scale is approximately one order of magnitude larger than the grid spacing, which shows that the DNS resolution used is sufficient.

Boundary conditions at the inflow plane $x/D = 0$ are prescribed in the form of velocity, enthalpy, and mass-fraction profiles as functions of y. Zero derivatives are imposed at the y-boundaries and periodicity is prescribed in the z-direction. Non-reflecting exit boundary conditions are used at the exit plane, $x/D = 16$. This allows acoustic pressure waves to exit the domain without disturbing the flow field [72]. Both instantaneous and time-averaged quantities are examined. The time-averaged quantities contain approximately $17,500$ samples and are denoted by an over-bar.

4.3.4 Fluid and scalar dynamics

The flow-field is illustrated in Fig. 4.2. Instantaneous contours of vorticity magnitude are shown at $z = 0$, $y = 0$ and $y/D = 0.5$ in panels (a), (b) and (c), respectively. The contours in Fig. 4.2(a) show a typical Karman vortex street in which vortices pair and roll up, and after which three-dimensional instability ensues resulting in the appearance of vortex tubes and the breakdown of regular vortices [90]. As the vortices grow, they bring hot and cool fluids — as well as DBP-laden fluid and DBP-free fluid — into contact. The three-dimensionality of the flow, evidenced in Fig. 4.2(b) and Fig. 4.2(c), suggests that mixing in the span-wise direction begins by $x/D = 5$. The contours also show that the shear layers merge by $x/D = 8$.

The manner in which the temperature and species fields evolve as the flow develops significantly affects particle formation. Molecules collide and if the surface tension binding them together is greater than the kinetic energy of the molecules then that cluster of molecules is said to be stable for future growth [17]. If not then the cluster disassociates into its constituent molecules. The collisions are proportional to the concentration and the kinetic energy is proportional to the temperature. The temperature is non-dimensionalized via $\theta = (T - T_\infty)/(T_o - T_\infty)$ and the DBP mass fraction is normalized via $\phi = (Y_{DBP} - Y_{DBP_\infty})/(Y_{DBP_o} - Y_{DBP_\infty})$. Cross-stream profiles of the time-averaged temperature $\overline{\theta}$ and DBP mass fraction, $\overline{\phi}$ are shown in Fig. 4.3. The profiles are quite similar and show that between $x/D = 2$ and $x/D = 4$ transport is primarily due to diffusion as the quantities diffuse across the height of the wake. Differences in diffusive transport are evident even at $x/D = 2$. If one looks at the region near the interface of the two streams, $y/D = \pm 0.5$, its evident that the gradients (in the cross-stream y-direction) are sharper in the mass-fraction, $\overline{\phi}$, than in the temperature $\overline{\theta}$. This is due to the non-unity Lewis number, $Le = 5.43$. This dissimilar molecular scale transport results in high concentration at a lower temperature and is what Clement (1985) refers to in describing nucleation when the Lewis number is unity [81]. With $Le = 1$, the profiles would almost be identical which would decrease the saturation ratio (given by Eq. 4.7), a measure of the driving force towards particle formation. Between $x/D = 4$ and $x/D = 8$, large-scale convective transport becomes significant. For example, at the centerline $y/D = 0$ the temperature drops by roughly 75%. Similarly, the non-dimensional mass fraction decreases from $\overline{\phi} = 0.98$ at $x/D = 4$ to $\overline{\phi} = 0.25$ at $x/D = 8$. Further

downstream, the wake grows as the faster co-flowing fluid entrains and dilutes the DBP-laden vapor. The result is by $x/D = 16$, the temperature and concentration are within 12% of the values in the co-flowing streams. The effect of a non-unity Lewis number is most obvious in the laminar region of the flow. Once turbulent mixing becomes more prominent, the gradients in temperature and concentration drive augment nucleation and the importance of the Lewis number diminishes slightly. However, it still remains important.

4.3.5 Particle nucleation rate

Generally, the dynamics of the temperature and the mass-fraction are such that the saturation ratio increases as the jet travels downstream. This is primarily through cooling and dilution. The saturation ratio is a function of temperature, mass-fraction, and the saturation mole fraction, x_{sat}, for DBP. It is the latter that causes the significant changes in S. A scatter plot of the instantaneous nucleation rate, $\log_{10}(J)$, vs saturation ratio, S, is shown in Fig. 4.4(a). The data shows that the nucleation rate increases with increasing saturation ratio, though not linearly. Nucleation rates above $J = 1$ particle/$(m^3 \cdot s)$ require the saturation ratio to be higher than approximately $S = 20$, which is 200% higher than the inlet condition (at $x/D = 0$). A large saturation ratio value indicates a location that has departed far from thermodynamic equilibrium. A return to equilibrium entails a phase change of an increasing amount of mass or high nucleation rate. An increasingly large departure from equilibrium is needed for higher nucleation rates to occur. Large-scale convective transport and molecular mixing, evidenced in Fig. 4.3, lead to saturation ratios in excess of $S = 1500$, which in turn leads to nucleation rates as high as $J = 1 \times 10^{17}$ particles/$(m^3 \cdot s)$. Additionally, it is important to note that for a given nucleation rate there are a range of saturation ratio values. And, in fact, there are multiple conditions in the flow that can produce the same nucleation rate.

A slightly different view of the nucleation dynamics is presented in the temperature-mass-fraction scatter plot shown in Fig. 4.4(b). This reflects how various combinations of temperature and mass-fraction result in the nucleation of particles of various sizes. As the wake travels downstream, the fluid emanating from the nozzle traverses trajectories which begin at the upper right (hot and concentrated) and end near the lower left (cool

and dilute). The figure shows that the critical particle sizes vary from $d_p = 2nm$ to $d_p = 3nm$. The rate at which the small $2nm$ diameter particles form is some 5 to 7 orders of magnitude greater than the rate at which the larger $3nm$ diameter particles form. The figure also shows that as the temperature decreases, the particle diameter also decreases [91]. At high mass-fractions, changes in the temperature have a more significant effect on the nucleation rate as compared to low mass-fractions. The reason for this conclusion can be seen by fixing the mass-fraction at a high value ($\phi = 0.6$, for example) and decreasing the temperature. As the temperature decreases, you will pass through lines of constant nucleation rate, the rate increasing a number of orders of magnitude. Conversely, at very low mass-fraction values ($\phi = 0.2$, for example) a similar decrease in temperature yields a smaller increase in nucleation rate. Similarly, at low temperatures, changes in the mass-fraction have a more substantial effect on the nucleation rate, compared to the same changes at high temperatures. In laminar flows, molecular transport is the mechanism by which the fluid elements traverse this space, illustrating the importance of the Lewis number. A Lewis number of unity, $Le = 1$, means that changes in the temperature are met with commensurate changes in the mass-fraction. With $Le = 5.38$, the rate at which the fluid cools is greater than the rate at which it is diluted, resulting in greater saturation ratios than in the $Le = 1$ scenario. That is the rate-of-descent through Fig. 4.4(b) is more steep with $Le = 5.38$ than it is with $Le = 1$, yielding more nucleation [81].

Contours of the nucleation rate are shown in Fig. 4.5. Two views are presented. The first contains instantaneous nucleation, $\log(J)$, at time $t^\star = 82$ shown in Fig. 4.5(a), and the second contains the time-averaged nucleation rate, $\overline{J}$, shown in Fig. 4.5(b). The log is shown purely to elucidate how particle nucleation occurs as the flow develops. This is because the values have significant variation ($10^2 < J < 10^{18}$) and the high values would completely obfuscate the dynamics within the developing wake. The instantaneous contours show that within the first four diameters, nucleation is confined to the interface of the two streams where molecular diffusive transport is the dominant mechanism. Again, this is enhanced by the non-unity Lewis number [81]. However, as the vortices form and roll-up and the two streams mix (between $x/D = 4$ and $x/D = 10$) nucleation across the width of the wake increases significantly. Molecular transport is greatly aided by large-scale convective transport which brings the faster-moving, cooler,

DBP-free fluid into contact with the slower-moving, hotter, DBP-laden fluid. As a result the nucleation rate is as high as $J = 10^{14}$ particles/$(m^3 \cdot s)$ across the height of the wake by $x/D = 8$. The flow travels further downstream, becomes turbulent, and both the nucleation rate and the extent of the flow in which nucleation is taking place increase. This reflects the merging of the shear-layers and the large-scale mixing of the hot, low-speed, DBP-laden fluid, with the cooler, DBP-free high-speed stream. Instead of thin bands of nucleation, there are "large blobs" of gas that are now producing DBP nanoparticles. If one considers the time-averaged nucleation rate, shown in Fig. 4.5(b), its clear that nucleation prior to the collapse of the wake potential core is insignificant compared to the post-collapse nucleation field. Between $x/d = 8$ and $x/D = 16$, the nucleation rate increases slightly, but the greater change is the growth, or spreading, of the wake and the accompanying spread of nucleation. Across the height of the wake, from $-2.5 < y/D < 2.5$, the nucleation rate is fairly uniform with values between $J = 10^{14}$ and $J = 10^{15}$.

4.3.6 Analysis of the SGS nucleation

Nucleation is sensitive to temperature and concentration fluctuations. This is observed by considering the dependence on the square of the mass-fraction, Y, and the exponential temperature dependence in Eq. (4.5). Understanding the effects of the fluctuations is key to improving the predictive ability of modeling tools. Here we define large or resolved scale quantities and small or unresolved subgrid-scale quantities in a manner consistent with large eddy simulation [92, 93]. The large or resolved-scale variables are obtained via

$$\langle A(\vec{x},t)\rangle_\ell = \int_{-\infty}^{\infty} h_s(x^o,\vec{x})A(x^o,t)dx^o \tag{4.9}$$

where $h_s(\vec{x},t)$ is the spatial filter function and $\langle A(\vec{x},t)\rangle_\ell$ is the spatially-filtered quantity [93]. The filter employed here is the commonly-employed top-hat or "moving average" filter with width Δ_F [92, 94]. The flows considered here are of variable density which means that density-weighted or Favre-filtered quantities must be used. These quantities are defined via

$$\langle A(\vec{x},t)\rangle_L = \frac{\langle \rho A(\vec{x},t)\rangle_\ell}{\langle \rho\rangle_\ell} \tag{4.10}$$

and fluctuations are defined as $A' = A - \langle A \rangle_L$ [95]. To elucidate the effects of the unresolved, small-scale fluctuations on nucleation, we compute the nucleation rate based on the resolved-scale quantities and obtain the SGS component via subtraction. The large-scale nucleation rate, J_L^F is given by

$$J_L^F = \frac{\left(\langle \rho \rangle_\ell \langle Y_{DBP} \rangle_L\right)^2}{\rho_{cL}^F m_m} \sqrt{\frac{2\sigma_L^F}{\pi m_m}} \frac{1}{S_L^F} \exp\left(\frac{\sqrt[3]{36\pi v_m^2}\sigma_L^F}{k_B \langle T \rangle_L} - \frac{\pi \sigma_L^F {d_{cL}^F}^2}{3 k_B \langle T \rangle_L} \right) \tag{4.11}$$

where S_L^F, d_{cL}^F and σ_L^F are the resolved-scale saturation ratio, critical diameter, and surface tension, respectively, obtained using the filtered temperature, mass-fraction, density and pressure. The SGS nucleation rate is defined as the difference between the two rates, $J_L^{SGS} = J - J_L^F$. Negative values of J^{SGS} indicate that the SGS interactions act to decrease particle nucleation, while positive values of J^{SGS} indicate that the interactions act to increase particle nucleation. We utilize two filter widths in this study. In case 1, the DNS data is filtered using a filter width of $\Delta_F = 4 \times \Delta_{DNS}$ and in case 2 a value of $\Delta_F = 8 \times \Delta_{DNS}$ is utilized, where Δ_{DNS} is the grid spacing employed in the DNS. These values are chosen as they compare favorably with resolutions used for LES of similar flows [34, 29, 96, 97]. Scatter plots of the normalized, filtered temperature, $\langle \theta \rangle_L$, and mass-fraction, $\langle \phi \rangle_L$, versus their exact counterparts (θ and ϕ) are shown in Fig. 4.6. Figure 4.6(a) shows that for high temperatures, the filtered value is lower than the exact, $\langle \theta \rangle_L < \theta$. At low temperatures the trend reverses and the filtered value is generally higher than the exact, $\langle \theta \rangle_L > \theta$. This trend is more pronounced when the larger filter width is used (in case 2). Figure 4.6(b) shows a similar trend for the mass-fraction. These results indicate that the filtering acts to create a more homogeneous dependent variable field.

Scatter plots of the saturation ratio obtained using the filtered temperature and mass-fraction, S_L^F, versus the exact saturation ratio, S, are shown in Fig. 4.7. Figure 4.7(a) shows that for case 1, at low values of saturation ratios, $S_L^F > S$. However, as S increases, this trend reverses. For example, at $S = 200$, S_L^F ranges from $S_L^F = 50$ to $S_L^F = 600$, with the majority of values above $S_L^F = 200$. Conversely, at $S = 600$ the majority of the values lie between $S_L^F = 250$ and $S_L^F = 700$. Again, with a small number of higher outliers. Similar results for case 2 are presented in Fig. 4.7(b). Here, as in case 1, use of the filtered temperature and mass-fraction tends to lead to an over-prediction of the lowest saturation ratio values, and an under-prediction at the higher saturation

ratio values. The increased filter-width used in case 2 is responsible for the complete absence of values above $S_L^F = 900$. Mixing — diffusion, large-scale convective, or as mimicked by the spatial filtering — creates a more homogeneous dependent variable field and provides fewer opportunities for the system to be as far from thermodynamic equilibrium. Thus, as small-scale fluctuations are removed, the highest saturation ratio values are greatly reduced.

A comparison between the nucleation rate J_L^F and the exact nucleation rate J for case 1 is shown in Fig. 4.8(a). While the maximum value of J_L^F is slightly lower than the exact nucleation rate, the lower values tend to be over-predicted. In the majority of the flow, where nucleation rates are relatively low, the flow is not yet well-mixed. The use of the spatially filtered dependent variables mimics more mixed temperature and mass-fraction fields, most often resulting in greatly increased nucleation rates. The highest nucleation rates only occur once transition to turbulence begins. Here, the flow is well-mixed, and the filtering process affects the temperature and mass-fraction fields less. This results in less scatter at the highest nucleation rate values. For example, when the exact nucleation rate is $J = 10^2$ particles/$(m^3 \cdot s)$ the nucleation rate based on the filtered temperature and mass-fraction varies between $J_L^F = 1$ to $J_L^F = 10^{14}$ particles/$(m^3 \cdot s)$. This shows an opportunity for an over-prediction of as much as 12 orders of magnitude. However, this trend reverses as the nucleation rate increases. At higher nucleation rates, the degree of variability decreases and the trend is for J_L^F to be lower than the exact rate J. At a nucleation rate of $J = 10^{15}$ particles/$(m^3 \cdot s)$, the nucleation rate based on the filtered temperature and mass-fraction varies between $J_L^F = 10^{11}$ particle/$(m^3 \cdot s)$ to $J_L^F = 10^{16}$ particles/$(m^3 \cdot s)$. When the filter-width is increased, the trends are similar but the magnitudes are increased. The results for case 2 are shown in Fig. 4.8(b). The non-linear nature of Eq. (4.5) and Eq. (4.7) can be seen by examining the correlation coefficient values for the nucleation rate. The definition used here is the covariance of the variables in question (J and J_L^F, for example) divided by the product of their standard deviations, $r = cov(J, J_L^F)/\sigma_J \sigma_{J_L^F}$ [98]. The correlation coefficient for the nucleation rate for case 1 is $r = 0.60$. The increased filter width of case 2 shows a much larger effect, yielding a correlation coefficient of $r = 0.39$ for the nucleation rate. These results suggest that the nucleation rate is quite sensitive to small fluctuations in temperature and mass-fraction.

The difference between the exact nucleation rate, J, and the nucleation rate based on the filtered temperature and DBP mass-fraction, J_L^F is the SGS nucleation rate, J^{SGS}. Probability density functions (PDFs) of the J^{SGS} are constructed to provide a more quantitative description of the SGS interactions. The SGS nucleation values are separated into positive and negative values for ease of presentation. Negative J^{SGS} values ($J^{SGS} < 0$) mean that the unresolved SGS interactions act to reduce the nucleation of nanoparticles while positive values ($J^{SGS} > 0$) mean that the unresolved SGS interactions act to increase nanoparticle nucleation. The PDF of the SGS nucleation rate for case 2 is shown in Fig. 4.9. The PDF shows that while there are more than twice as many negative SGS values ($J^{SGS} < 0$) as there are positive SGS values ($J^{SGS} > 0$), the positive contributions are as much as two orders of magnitude greater than the negative contributions. This PDF provides a comprehensive overview of the effect of the unresolved temperature and mass-fraction interactions on homogeneous nucleation. The SGS interactions predominantly act to increase nucleation.

4.3.7 Sensitivity of nucleation to scalar fluctuations

To elucidate more clearly how changes or fluctuations in the fluid temperature and DBP mass-fraction affect the nucleation rate, PDFs of the SGS nucleation rate conditioned on the normalized temperature fluctuation, $\theta' = \theta - \langle\theta\rangle_L$, and the normalized DBP mass-fraction fluctuation, $\phi' = \phi - \langle\phi\rangle_L$ are constructed. (Note: if the SGS interactions did not affect the nucleation rate, then J^{SGS} would be zero and the scatter shown in Fig. 4.7 and Fig. 4.8 would be straight lines.) The fluctuations are such that positive values of θ' and ϕ' reflect small-scale heating and increased concentration, respectively, while negative values reflect small-scale cooling and dilution.

PDFs of the SGS nucleation rate conditioned on the temperature fluctuation θ' for case 2 are presented in Fig. 4.10. Again, for clarity, the SGS nucleation is separated into positive and negative contributions. Positive SGS nucleation values are shown in Fig. 4.10(a) and negative SGS nucleation values are shown in Fig. 4.10(b). If we look to where the SGS interactions act to decrease nucleation, Fig. 4.10(a) shows that locations where the temperature is increased by up to 10% are most prominent while locations where the temperature is decreased by up to 10% decrease the nucleation rate by the highest magnitude, $J^{SGS} = -1.6 \times 10^{12}$ particles/$(m^3 \cdot s)$. Turning to the

PDF of the positive SGS nucleation rate, Fig. 4.10(b) suggests that locations where SGS cooling decreases the temperature by up to 10% result in SGS nucleation rates as high as $J^{SGS} = 10^{14}$ while locations where SGS heating increases the temperature by up to 10% result in SGS nucleation rates as high as $J^{SGS} = 10^{12}$. Ie. SGS cooling results in the most significant change to the nucleation rate. This is expected as a decrease in temperature means a decrease in the kinetic energy of the DBP molecules, and therefore an increase in the number of stable DBP clusters available for future growth. Additionally, a decrease in temperature results in a lower DBP saturation mole fraction, x_{sat}, which allows super-saturation (and thus nucleation) to occur at lower DBP vapor concentrations.

PDFs of the SGS nucleation rate are also conditioned on the DBP mass-fraction fluctuation and the results for case 2 are presented in Fig. 4.11. Turning our attention to locations where the SGS nucleation is negative ($J^{SGS} < 0$), shown in Fig. 4.11(a), a fluctuation corresponding to a 10% increase in mass-fraction is the most frequent value, corresponding to $J^{SGS} = 1.6 \times 10^{12}$ particles/$(m^3 \cdot s)$. However, there are a cluster of values corresponding to $J^{SGS} = 6.3 \times 10^{12}$, the most prominent of which occurs when the fluctuation decreases the normalized DBP mass-fraction by as much as 10%. Looking back at Fig. 4.4, the data suggest that if such changes in the mass-fraction results in such large SGS nucleation values, then the mass-fraction itself must be relatively low – somewhere in the range $0.01 < \phi < 0.15$. The PDFs presented in Fig. 4.11(b) show that locations where SGS dilution occurs act contribute the most to positive SGS nucleation. The reason for this is not obvious considering that a decrease in DBP mass-fraction (while the temperature is constant) results in a decrease in the saturation ratio and therefore a decrease in the nucleation rate. However, the data presented in Fig. 4.4 suggests that if the decrease in mass-fraction is accompanied by a decrease in temperature then the nucleation rate does indeed increase. At high DBP mass-fractions the magnitude of the temperature decrease needed is less than that needed at lower mass-fractions. More simply put, mixing which results in dilution and cooling yields more nucleation when the mass-fraction is high.

4.4 Conclusions

Direct numerical simulation (DNS) of the nucleation of dibutyl-pthalate (DBP) particles in a turbulent wake was performed. Classical nucleation theory (CNT) is employed to model the formation of particles from DBP vapor. An *a priori* analysis of the DNS data was performed to elucidate the effects of unresolved or subgrid-scale (SGS) interactions on nanoparticle nucleation. The temperature, pressure, density and mass-fraction fields are spatially filtered — using two filter-widths — and the saturation ratio and nucleation rates are computed. Those quantities are compared to the exact saturation ratio and nucleation rate, thus isolating the effects of SGS scalar-scalar interactions on nanoparticle nucleation. As the filter-width is increased, so too is the magnitude of the unresolved or SGS terms.

The simulation data shows that nucleation initially occurs at the interface of the slow, hot, DBP-laden stream, and the cooler, high-speed DBP-free stream. This is where diffusion-driven mixing occurs resulting in an increase in the saturation ratio. However, as the flow develops convective mixing or entrainment becomes the dominant mixing mechanism and the nucleation rate increases significantly and is no longer confined to the shear layers. So while shear layer nucleation is indeed present, the increase in nucleation rate once the potential core collapses is several orders of magnitude greater [50]. Consideration of nucleation rates in the temperature—mass-fraction space suggests that a Lewis number of unity ($Le = 1$) results in reduced nucleation as postulated by Clement (1985) [81]. The results also show that the effects of the unresolved or SGS fluctuations are quite significant, though decreasingly so as the nucleation rate increases. At low nucleation rates, the fluctuations primarily serve to decrease particle formation, while at the highest nucleation rates, the SGS fluctuations act to increase particle formation. And, statistical analyses reveal that vapor dilution and cooling occurs where the SGS fluctuations increase.

Analysis of the DNS dataset suggests that fluid turbulence, simulation resolution and fluctuations can be as significant as nucleation theories (CNT, scaled nucleation theory, etc.) in the accuracy of predicting particle formation rates. Additionally, the importance of molecular mixing — vis a vis the Lewis number — on nucleation suggests that modeling approaches such as gradient-diffusion type closures which employ unity Lewis

number assumptions can significantly under-predict particle formation in the transition region of turbulent flows [66]. As nucleation tends to scavenge vapor via condensation, and affect subsequent particle formation and growth rates, careful modeling is required and probability-based approaches that are able to account for unequal diffusivities can be of great utility [99].

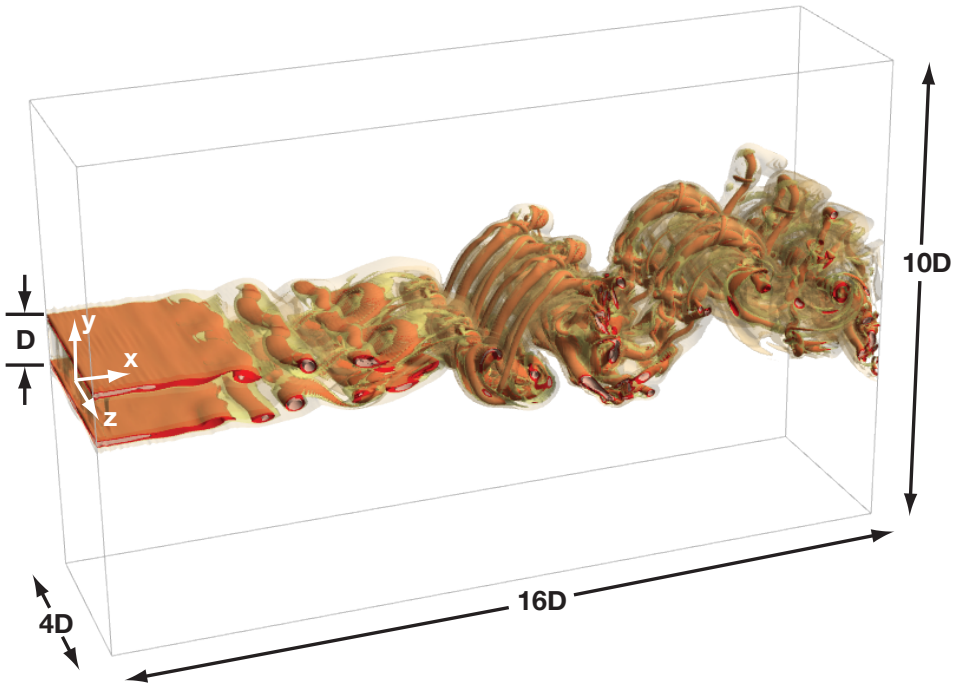

Figure 4.1: Flow schematic

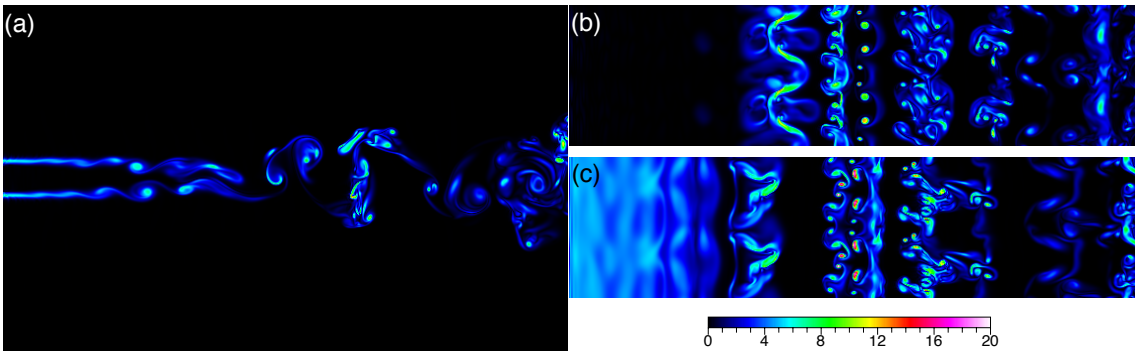

Figure 4.2: Instantaneous contours of vorticity magnitude at time $t^\star = 81.79$: (a) $z = 0$; (b) $y = 0$; and (c) $y/D = 0.5$.

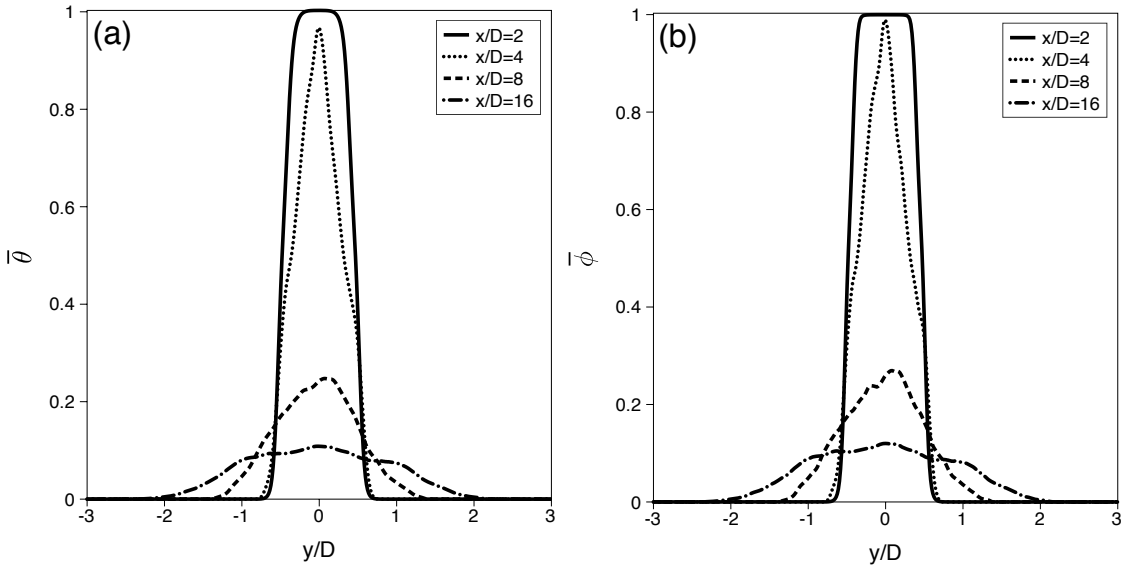

Figure 4.3: Cross-stream profiles of the time-averaged (a) normalized temperature, $\overline{\theta}$, and (b) normalized DBP mass fraction, $\overline{\phi}$.

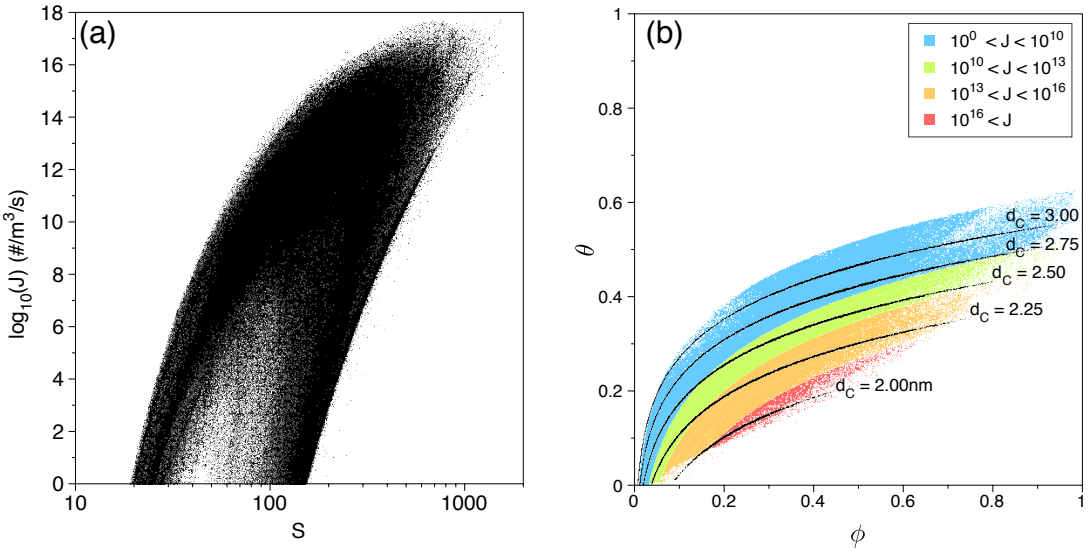

Figure 4.4: (a) Scatter plot of the nucleation rate, $\log_{10}(J)$, vs saturation ratio, S; (b) Scatter plot of the normalized temperature, θ versus normalized mass-fraction ϕ with lines of constant critical diameter, d_C.

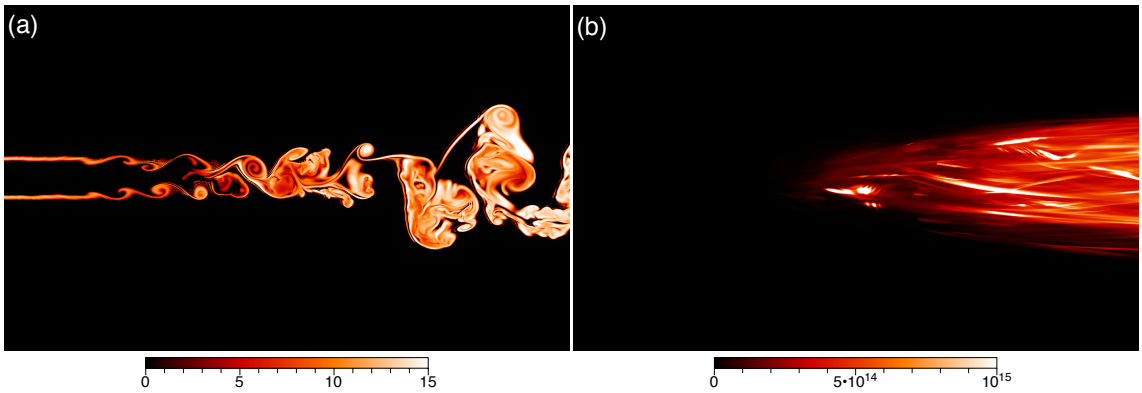

Figure 4.5: Contours of the nucleation rate particles/$(m^3 \cdot s)$: (a) instantaneous $\log_{10}(J)$ on plane $z = 0$, at time $t^\star = 81.79$; (b) time-averaged, $\overline{J}$.

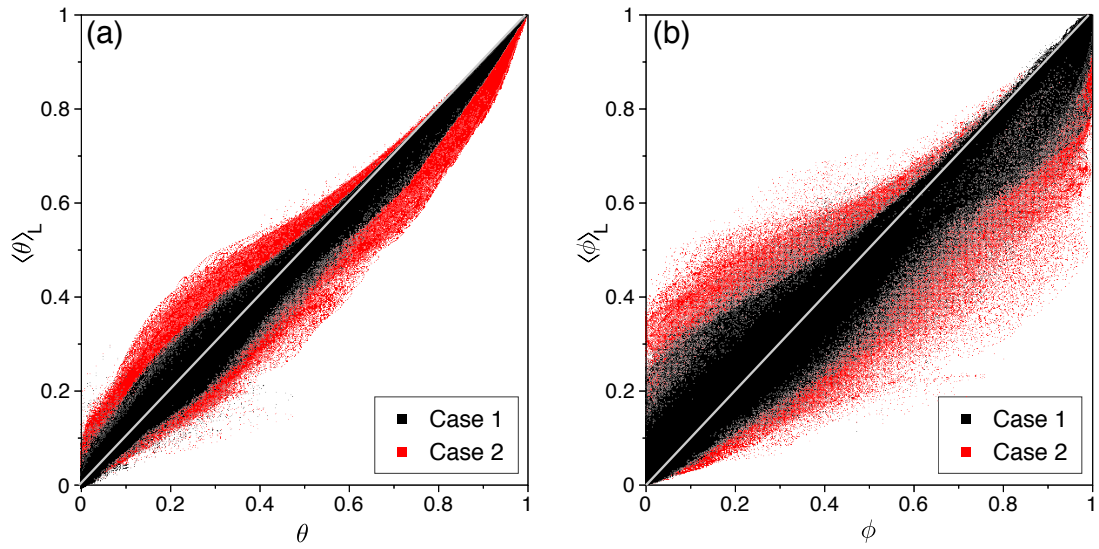

Figure 4.6: Scatter plots of (a) the normalized, filtered temperature, $\langle\theta\rangle_L$, versus exact normalized temperature, θ, and (b) the normalized, filtered DBP mass-fraction, $\langle\phi\rangle_L$, versus the exact normalized DBP mass fraction, ϕ, at time $t^\star = 81.79$. The line of equal values is shown in gray.

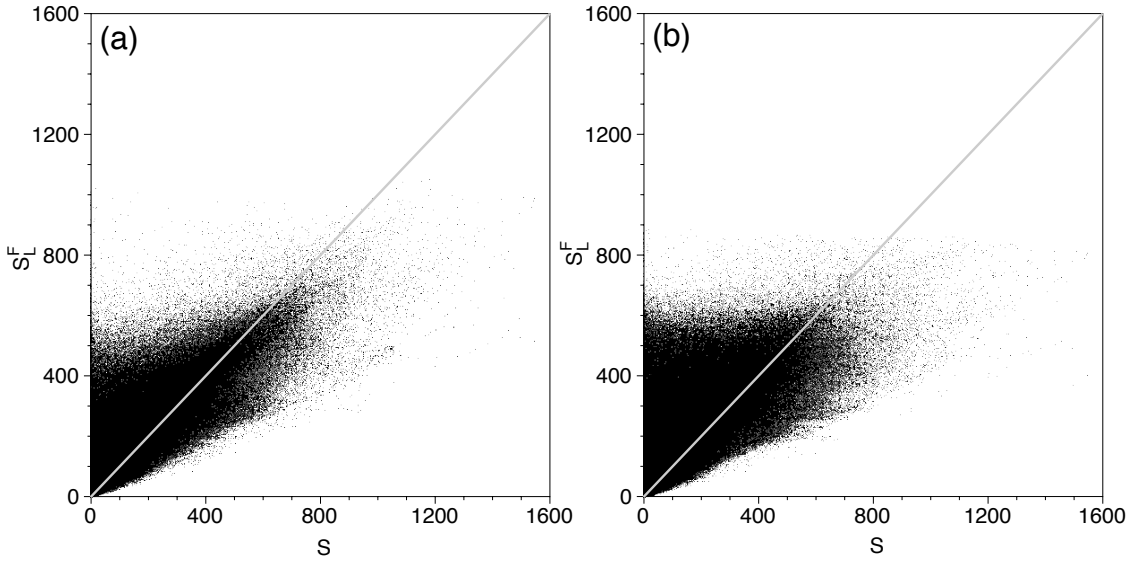

Figure 4.7: Scatter plots of the saturation ratio based on the filtered temperature and DBP mass-fraction, S_L^F, versus the exact saturation ratio, S at time $t^\star = 81.79$: (a) Case 1; (b) Case 2.

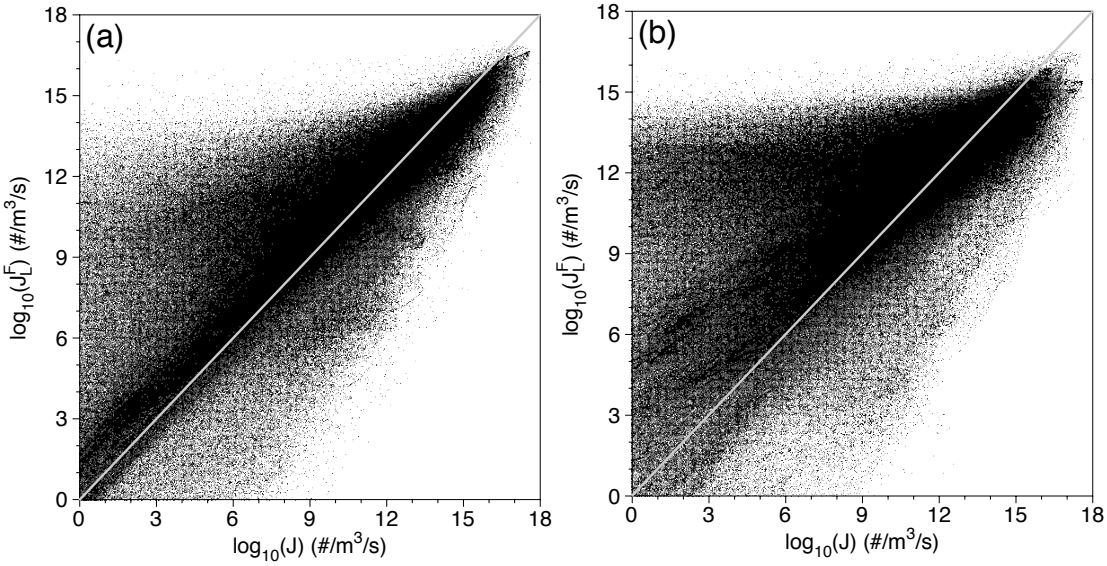

Figure 4.8: Scatter plots of nucleation rate based based on the filtered temperature and DBP mass-fraction, J_L^F, versus exact nucleation rate J at time $t^\star = 81.79$: (a) Case 1; (b) Case 2.

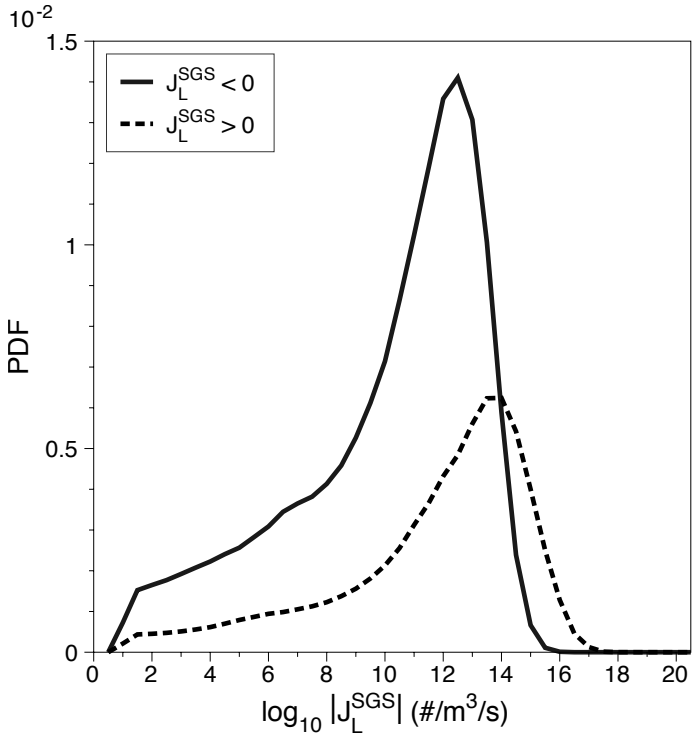

Figure 4.9: Probability density function of the subgrid-scale nucleation rate J_L^{SGS} for case 2.

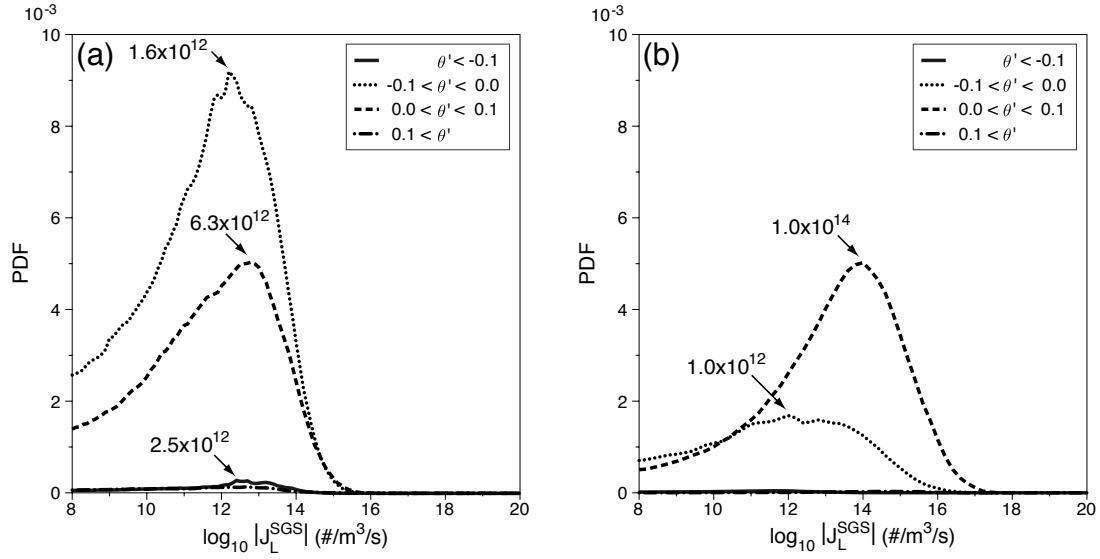

Figure 4.10: Probability density functions of the magnitude of the SGS nucleation rate, J_L^{SGS}, conditioned on the normalized temperature fluctuation, θ' (Case 2): (a) $J_L^{SGS} < 0$; (b) $J_L^{SGS} > 0$.

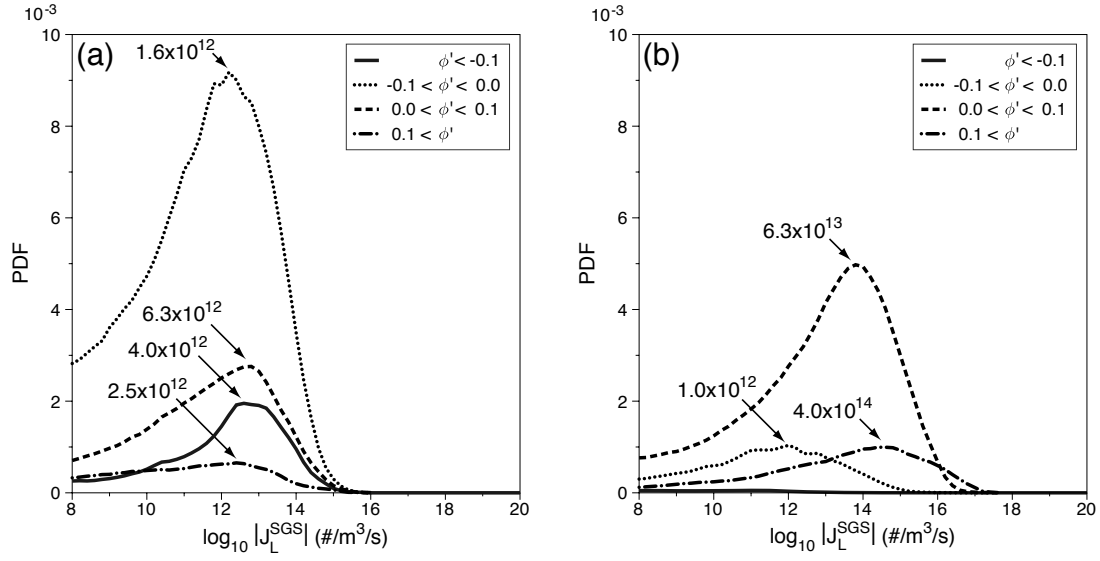

Figure 4.11: Probability density functions of the magnitude of the SGS nucleation rate, J_L^{SGS}, conditioned on the normalized mass-fraction fluctuation, ϕ' (Case 2): (a) $J_L^{SGS} < 0$; (b) $J_L^{SGS} > 0$.

Chapter 5

Large eddy simulation of homogeneous nucleation

5.1 Introduction

Nucleation is a phase-change phenomenon that occurs in processes that range from atmospheric cloud formation to industrial production of chemicals, powders and coatings [12, 17]. Since the seminal cloud chamber nucleation experiments were carried out by Wilson (1927), countless experiments, calculations and simulations of nucleation have been undertaken [15]. While these studies have provided valuable insight into nucleation there are still aspects of the process, including the effects of turbulence, that are still not fully understood [100, 74]. Lesniewski and Friedlander (1998) carried out an often cited experiment in which dibutyl-phthalate (DBP) was produced via homogeneous nucleation in a free jet [50]. The structure of nucleation was described, showing nucleation occurred both in the initial shear layer and in the well-mixed downstream region. DBP particle size distributions were calculated and scaling laws were developed to relate number concentration to position in the jet. Many calculations and simulations have sought to repeat these results and simulate nucleation in more general flows. Given the physical size of typical experiments and the range of scales involved, large-eddy simulation (LES) is the computation method most often used to investigate these and other complex, multiphase flows.

While LES is able to capture the large scales of motion, the subgrid-scale (SGS)

motions and interactions must be modeled. A number of LES studies have been carried out to investigate nucleation. Housiadas *et al.* (2004) utilized LES data to compute particle nucleation in a planetary boundary layer [53]. Their work suggested that small-scale turbulence affects nucleation rates considerably, but they assert that this effect has diminished influence on average rates. The LES simulation that produced the data utilized for their calculations used a gradient-diffusion type model for the unresolved fluid-scalar interactions. This model was applied identically to the thermal and mass fields. Nucleation calculations have also been directly implemented in LES studies. Yin *et al.* (2007) carried out LES of nanoparticle nucleation in impinging jets, showing that nucleation takes place primarily in the interface region between hot and cold streams [101, 102]. Their methodology was also been used to simulate vehicle exhaust dynamics, an aerosol system that included nucleation [103, 104]. These simulations all used a Smagorinsky-type closure with a constant eddy viscosity to model the subgrid-scale stress, while subgrid-scale fluid-scalar interactions were neglected [105]. Most closely related to the present work, Zhou and Chan (2011) simulated the free jet experiment of Lesniewski and Friedlander (1998) using LES and an equivalent mean nucleation method (EMNM) [106]. This method allowed the average nucleation rate to be calculated but relied on the time-averaged flow-field to calculate the average rate. Additionally, the same gradient-diffusion type mixing model was used for both the temperature and mass-fraction, while SGS contributions to the nucleation rate were neglected. Though these simulations (among others) have afforded more understanding of the nucleation process, the most sophisticated closures were Smagorinsky-type, gradient-diffusion models. These were used to model the subgrid-scale fluid-thermal and fluid-vapor interactions and subsequently their contribution to nucleation. SGS scalar-scalar interactions in the nucleation source term are often ignored.

Modeling of the SGS interactions has the possibility to obfuscate the nucleation process, as it has been shown that the effects of turbulent fluctuations on nanoparticle growth in turbulent shear flows are indeed significant [56, 82]. The intent of this work is to assess the ability of LES to accurately predict homogeneous nucleation using Smagorinsky-type, zero-equation, gradient-diffusion models for the SGS fluid-thermal and fluid-vapor interactions, while neglecting the scalar-scalar interactions in the nucleation source term. This assessment is carried out by comparing LES data to that

obtained via DNS for the same flow conditions. Two LES resolutions are used to determine how sensitive the nucleation calculation is to the range of scales modeled.

5.2 Formulation

5.2.1 Fluid and scalar fields

The flows investigated in this work are governed by the compressible Navier-Stokes equations. The conservation equations for the the velocities $u_i(x_i, t)$ in the x_i direction, pressure $p(x_i, t)$ and the enthalpy $h(x_i, t)$ are

$$\frac{\partial \rho}{\partial t} + \frac{\partial \rho u_j}{\partial x_j} = 0, \tag{5.1}$$

$$\frac{\partial \rho u_i}{\partial t} + \frac{\partial \rho u_i u_j}{\partial x_j} = -\frac{\partial p}{\partial x_i} + \frac{\partial \tau_{ij}}{\partial x_j} \tag{5.2}$$

and

$$\frac{\partial \rho h}{\partial t} + \frac{\partial \rho u_j h}{\partial x_j} = \frac{\partial}{\partial x_j}\left(\frac{k}{C_p}\frac{\partial h}{\partial x_j}\right) \tag{5.3}$$

where ρ is the fluid density, τ_{ij} is the viscous stress tensor for a Newtonian fluid, k is the thermal conductivity and C_p is the specific heat. The system is closed using the ideal gas equation of state, $p = \rho RT$, where R is the gas constant and T is the temperature, which is obtained via $dh = C_p dT$.

The flow consists of a condensible vapor and a non-condensible carrier species. The mass-fraction transport equation for these is

$$\frac{\partial \rho Y_i}{\partial t} + \frac{\partial \rho u_j Y_i}{\partial x_j} = \frac{\partial}{\partial x_j}\left(\mathcal{D}_i \frac{\partial \rho Y_i}{\partial x_j}\right) - \dot{\omega}_N, \tag{5.4}$$

where Y_i is the mass fraction of species i, $\mathcal{D}_i$ is its diffusion coefficient and $\dot{\omega}_N$ is the species sink due to particle nucleation, which accounts for the conversion of vapor to particles. This is set to zero for the carrier gas. These equations are solved in their exact form in the DNS.

5.2.2 Particle nucleation

Nucleation is modeled following the kinetic approach of Girshick and Chiu (1990)[57]. This method applies a correction to the classical nucleation expression that forces the

Gibbs free energy for monomers to zero.Nucleating particles have the size of a critical cluster (of diameter d_C) determined by:

$$d_C = \frac{4\sigma v_m}{k_B T \ln(S)}, \tag{5.5}$$

where σ is the surface tension of the condensed species, v_m is its molecular volume, k_B is the Boltzmann constant, T is the temperature and S is the saturation ratio of the condensable vapor. The saturation ratio is defined as the ratio of the vapor partial pressure of species i to the equilibrium (or saturation) vapor pressure at a given temperature, and given by

$$S = \frac{\rho R T}{p_{mix}} \frac{MW_{mix}}{MW_i} \frac{Y_i}{x_{sat}}, \tag{5.6}$$

where p_{mix} is the local, thermodynamic mixture pressure, MW_{mix} is the mixture molecular weight and x_{sat} is the saturation mole fraction for species i. With the self-consistent correction of Girshick and Chiu, the nucleation rate J can then be expressed as:

$$J = \frac{(\rho Y)^2}{\rho_c m_m} \sqrt{\frac{2\sigma}{\pi m_m}} \frac{1}{S} \exp\left(\frac{\sqrt[3]{36\pi v_m^2}\sigma}{k_B T} - \frac{\pi \sigma {d_c}^2}{3 k_B T} \right) \tag{5.7}$$

where m_m is the mass of a molecule of condensable species and ρ_c is its condensed phase density.

The sink term for nucleation $\dot{\omega}_N$ is the nucleation rate J multiplied by the empirical correction factor c_{nuc} (which is material-specific) and the mass of a critical cluster:

$$\dot{\omega}_N = c_{nuc} \frac{\pi}{6} \rho_c d_C^3 J. \tag{5.8}$$

5.2.3 Large eddy simulation

In LES, a filtering operation is used to decompose the flow variables into the sum of a filtered or resolved component $\langle A(\boldsymbol{x}, t) \rangle_\ell$ and the subgrid-scale (SGS) component $A(\boldsymbol{x}, t)'$ [93, 42, 107], i.e.

$$A(\boldsymbol{x}, t) = \langle A(\boldsymbol{x}, t) \rangle_\ell + A(\boldsymbol{x}, t)' \tag{5.9}$$

where

$$\langle A(\boldsymbol{x}, t) \rangle_\ell = \int_{-\infty}^{\infty} \mathcal{G}(\boldsymbol{x}', \boldsymbol{x}) A(\boldsymbol{x}', t) d\boldsymbol{x}' \tag{5.10}$$

and where $\mathcal{G}$ denotes the filter function of width Δ_G, which has the properties prescribed by Aldama (1990) and Vreman, *et al.* (1994), namely that for filter functions $\mathcal{G}(\boldsymbol{x}', \boldsymbol{x}) = G(\boldsymbol{x}' - \boldsymbol{x})$ we have $G(\boldsymbol{x}) = G(-\boldsymbol{x})$ and $\int_{-\infty}^{\infty} G(\boldsymbol{x}) d\boldsymbol{x} = 1$ [92, 108] . As the flows considered here are of variable density, flow variables must be density-weighted and a Farve-filtered quantity is defined as

$$\langle A(\boldsymbol{x}, t) \rangle_L = \frac{\langle \rho A(\boldsymbol{x}, t) \rangle_\ell}{\langle \rho \rangle_\ell} \tag{5.11}$$

and fluctuations are defined as

$$A(\boldsymbol{x}, t)'' = A(\boldsymbol{x}, t) - \langle A(\boldsymbol{x}, t) \rangle_L \tag{5.12}$$

following the work of Jaberi, *et al.* (1999) [95].

To obtain the governing equations used in LES, the filtering operation is applied to the Navier-Stokes equations, yielding equations that describe the large-scale motions of the flow, while SGS closures are needed to model the effects of the unresolved or residual motions and their interactions. The filtered, compressible continuity equation is then

$$\frac{\partial \langle \rho \rangle_\ell}{\partial t} + \frac{\partial \langle \rho \rangle_\ell \langle u_j \rangle_L}{\partial x_j} = 0, \tag{5.13}$$

and the filtered momentum equation is given by

$$\frac{\partial \langle \rho \rangle_\ell \langle u_i \rangle_L}{\partial t} + \frac{\partial \langle \rho \rangle_\ell \langle u_i \rangle_L \langle u_j \rangle_L}{\partial x_j} = -\frac{\partial \langle p \rangle_\ell}{\partial x_i} + \frac{\partial \langle \tau_{ij} \rangle_\ell}{\partial x_j} - \frac{\partial T_{ij}}{\partial x_i} \tag{5.14}$$

in which T_{ij} denotes the subgrid stress, given by

$$T_{ij} = \langle \rho \rangle_\ell \left(\langle u_i u_j \rangle_L - \langle u_I \rangle_L \langle u_j \rangle_L \right). \tag{5.15}$$

The equation of state is given here by

$$\langle p \rangle_L = \langle \rho \rangle_\ell R \langle T \rangle_L \tag{5.16}$$

where $R = \sum R_i \langle Y_i \rangle_L / MW_i$.

The filtering operation is similarly applied to the enthalpy and species transport equations. The enthalpy transport equation becomes

$$\frac{\partial \langle \rho \rangle_\ell \langle h \rangle_L}{\partial t} + \frac{\partial \langle \rho \rangle_\ell \langle u_j \rangle_L \langle h \rangle_L}{\partial x_j} = \frac{\partial}{\partial x_j} \left(\frac{k}{C_p} \frac{\partial \langle h \rangle_L}{\partial x_j} \right) - \frac{\mathcal{M}_j^h}{\partial x_j} \tag{5.17}$$

where $\langle h \rangle_L$ is the filtered enthalpy and $\mathcal{M}_j^h$ is the subgrid fluid-thermal flux. This represents the unresolved or subgrid-scale interactions between the thermal and fluid field, given by

$$\mathcal{M}_j^h = \langle \rho \rangle_\ell \left(\langle u_j h \rangle_L - \langle u_j \rangle_L \langle h \rangle_L \right). \tag{5.18}$$

Similarly, the species mass-fraction transport equation in LES is

$$\frac{\partial \langle \rho \rangle_\ell \langle Y_i \rangle_L}{\partial t} + \frac{\partial \langle \rho \rangle_\ell \langle u_j \rangle_L \langle Y_i \rangle_L}{\partial x_j} = \frac{\partial}{\partial x_j} \left(\mathcal{D}_i \frac{\partial \langle \rho \rangle_\ell \langle Y_i \rangle_L}{\partial x_j} \right) - \frac{\mathcal{M}_j^i}{\partial x_j} - \langle \dot{\omega}_N \rangle_L, \tag{5.19}$$

where $\langle Y_i \rangle_L$ is the filtered mass-fraction for species i, $\mathcal{M}_j^i$ is the subgrid fluid-species flux and $\langle \dot{\omega}_N \rangle_L$ is the filtered nucleation sink term. The subgrid-scale species flux is given by

$$\mathcal{M}_j^i = \langle \rho \rangle_\ell \left(\langle u_j Y_i \rangle_L - \langle u_j \rangle_L \langle Y_i \rangle_L \right). \tag{5.20}$$

5.2.4 Subgrid-scale closures

The subgrid-scale viscosity (or eddy viscosity), ν_t, described by Smagorinsky is used to close the residual stress tensor in Eq. 5.14 [107]. Following the work of Colucci *et al.* a modified kinetic energy viscosity (MKEV) model is used to obtain an expression for the SGS viscosity and subgrid stress [109, 110]. The variable-density form of the model yields a SGS viscosity of

$$\nu_t = C_R \Delta_G \mathcal{E}^{1/2} \tag{5.21}$$

where

$$\mathcal{E} = |\langle u_i^\star \rangle_L \langle u_i^\star \rangle_L - \langle \langle u_i^\star \rangle_L \rangle_{\ell'} \langle \langle u_i^\star \rangle_L \rangle_{\ell'}|, \tag{5.22}$$

$\langle \mathcal{S}_{ij} \rangle_L$ is the resolved strain rate tensor and $u_i^\star = u_i - \mathcal{U}_i$, where $\mathcal{U}_i$ is a reference velocity in the u_i direction. The subscript ℓ' denotes a secondary level filter with a larger size than the grid filter, and is denoted by $\Delta_{G'}$. C_R is a model constant. The subgrid stress is given by

$$T_{ij} = -2\nu_t \langle S_{ij} \rangle_L, \tag{5.23}$$

where $\langle S_{ij} \rangle_L$ is the strain rate tensor based upon the resolved velocities,

$$\langle S_{ij} \rangle_L = \frac{1}{2} \left(\frac{\partial \langle u_i \rangle_L}{\partial x_j} + \frac{\partial \langle u_j \rangle_L}{\partial x_i} \right). \tag{5.24}$$

The SGS thermal flux is modeled using a gradient-diffusion type model where the flux is proportional to the gradient of the filtered variable [110, 111]. This approach yields

$$\mathcal{M}_j^h = -\Gamma_t^h \frac{\partial \langle h \rangle_L}{\partial x_j}. \tag{5.25}$$

Here, the SGS thermal diffusivity is defined as $\Gamma_t^h = \nu_t / Pr_t$, which is a function of the eddy viscosity. The turbulent Prandtl number, Pr_t, is assumed to be constant. The SGS species flux is defined in a similar manner, where

$$\mathcal{M}_j^i = -\Gamma_t^i \frac{\partial \langle Y_i \rangle_L}{\partial x_j}. \tag{5.26}$$

The SGS species diffusivity is $\Gamma_t^i = \nu_t / Sc_t$, where Sc_t is the turbulent Schmidt number.

To define the filtered nucleation sink term a large-scale nucleation rate, J_L^F, is defined. This is computed from the filtered quantities explicitly solved for in LES, and is given by

$$J_L^F = \frac{\left(\langle \rho \rangle_\ell \langle Y_{DBP} \rangle_L\right)^2}{\rho_{cL}^F m_m} \sqrt{\frac{2\sigma_L^F}{\pi m_m}} \frac{1}{S_L^F} \exp\left(\frac{\sqrt[3]{36\pi v_m^2}\,\sigma_L^F}{k_B \langle T \rangle_L} - \frac{\pi \sigma_L^F {d_{cL}^F}^2}{3 k_B \langle T \rangle_L} \right) \tag{5.27}$$

where S_L^F, d_{cL}^F, ρ_{cL}^F and σ_L^F are the large-scale saturation ratio, critical diameter, condensed-phase density and surface tension, calculated using the filtered temperature, mass-fraction, density and pressure. This then yields a species sink term of simply

$$\langle \dot{\omega}_N \rangle_L = c_{nuc} \frac{\pi}{6} \rho_{cL}^F \left(d_{cL}^F\right)^3 J_L^F. \tag{5.28}$$

It is important to note that the above sink term assumes the subgrid-scale portion of the nucleation rate is zero, hence the modifier "large-scale." Carrying out the filtering operation on the nucleation sink term would yield an unclosed expression, containing undefined terms such as the average nucleation rate. As simplifications may not easily be made to such a non-linear sink term, the large-scale nucleation expression is used to allow straightforward calculation. Neglecting the scalar-scalar interactions in the nucleation source term also allows the effects of the SGS interactions on nucleation to be clearly illustrated.

5.3 Results

5.3.1 Flow configuration and physical assumptions

The flow studied here is a three-dimensional planar wake where gas issues through a nozzle of height D at a velocity of U_o and temperature T_o into a co-flowing stream with velocity U_∞ and temperature T_∞. The velocity ratio is $U_o/U_\infty = 0.25$, and the Reynolds number based on the velocity difference $\Delta U = U_\infty - U_o$ is $Re = \rho_o \Delta U D/\mu_o = 4000$. The gas is comprised of a mixture of dibutyl-phthalate (DBP) and nitrogen. The inflow saturation ratio of the wake is set to $S_o = 1$, which yields a DBP mass fraction of $Y_{DBP} = 7.09 \times 10^{-3}$. The wake and co-flow temperatures are are $T_o = 400K$ and $T_\infty = 300K$, respectively. The Lewis number for this system is $Le = k/C_p\mathcal{D}_{DBP} = 5.4$, which indicates greater thermal diffusion than species mass diffusion.

In this work, bulk properties of DBP are used in accordance with classical nucleation theory (CNT). The expressions given by Nguyen *et al.* (1987) for the surface tension, $\sigma = 0.0353 - 0.0000863(T - 273.26)$ and saturation mole fraction, $x_{sat} = \exp(21.497 - 11497/T)$ are adopted here [58]. Additionally, the use of CNT often involves an empirical correction factor c_{nuc}, and in this work the value is taken to be $c_{nuc} = 3.2 \times 10^{-4}$, specific to DBP [59].

5.3.2 Numerical specifications and parameters

The transport equations are integrated using a hybrid MacCormack-based finite-difference scheme which is second order accurate in time and fourth order accurate in space [64, 71]. Boundary conditions at the inflow plane $x/D = 0$ are prescribed in the form of velocity, enthalpy, and mass-fraction profiles as functions of y. Zero derivatives are imposed at the y-boundaries and periodicity is prescribed in the z-direction. An exit boundary conditions is used that allows acoustic pressure waves to exit without disturbing the flow field [72]. Instantaneous and time-averaged quantities are stored as the flow develops. The latter are denoted by an over-bar.

Three cases are investigated in this work. The first is the direct numerical simulation (DNS). A domain size of $16D \times 10D \times 4D$ is covered by $1152 \times 704 \times 288$ grid points in the x, y and z directions, respectively in the DNS. Large eddy simulation (LES) is carried out on the same domain in the remaining two cases. The second case, denoted

LES A, utilizes $192 \times 128 \times 48$ grid points while the third, LES B, uses a resolution of $128 \times 64 \times 32$. For case LES A, the turbulent Schmidt number for the DBP vapor is $Sc_t = 0.8$ and the turbulent Prandtl number is $Pr_t = 0.8$. In case LES B, these values are set to $Sc_t = 0.7$ and $Pr_t = 0.7$. The SGS eddy viscosity constant for both LES cases is set to $C_R = 0.02$. These LES model constants are set to match the time-averaged flow field and thermal and vapor mass-fraction fields as closely as possible to the DNS.

5.3.3 Scalar dynamics

The thermal and concentration fields largely dictate the nucleation dynamics, as evidenced by their non-linear relationship to the nucleation rate in Eq. 5.7 and Eq. 5.27. More physically, nucleation is a result of molecular collisions. The balance between the colliding molecules' kinetic energy and the cohesive energy of the newly formed cluster dictates whether a stable nuclei is formed. This process is directly influenced by both the temperature and concentration fields as increased concentration yields a higher number of collisions and increased fluid temperature results in higher molecular kinetic energy. Any effect on these scalars by the SGS modeling thus has the potential to affect the nucleation calculation.

The temperature is non-dimensionalized via $\theta = (T - T_\infty)/(T_o - T_\infty)$ for ease of presentation. Cross-stream profiles of the time-averaged temperature $\overline{\theta}$ are shown in Fig. 5.1(a). As the wake develops, the hot and cool streams mix and the wake cools. At $x/D = 4$, cooling occurs primarily as a result of thermal diffusion between the hot and cool streams. Between $x/D = 4$ and $x/D = 8$ the flow cools more significantly as large-scale convective mixing ensues. By $x/D = 16$, the flow transitions to turbulence and becomes well-mixed. Both LES cases show good agreement with the DNS at $x/D = 4$. At $x/D = 8$ both the DNS and LES A cases have cooled to approximately 30% of the inlet value. However, LES B has only cooled to half the inlet value. This indicates that the lower-resolution LES case has entrained less cool fluid. The wake fluid in all three cases has cooled to below 15% of the inlet temperature and the wake has spread to approximately $y/D = \pm 2$ by the outlet at $x/D = 16$.

Similar to the temperature, the DBP mass fraction is normalized via $\phi = (Y_{DBP} - Y_{DBP_\infty})/(Y_{DBP_o} - Y_{DBP_\infty})$. Cross-stream profiles of the time-averaged DBP mass fraction, $\overline{\phi}$ are presented in Fig. 5.1(b). The DBP dilution trend shown here is similar to

the cooling shown in Fig. 5.1(a), though not as effective. This is a direct result of the non-unity Lewis number. At $x/D = 4$ – where mixing via molecular diffusion is most dominant – the mass-fraction shows steeper profiles than the temperature. It is in these areas that the higher thermal diffusivity is resulting in fluid that is cooling faster than it is diluting. By $x/D = 8$, the flow has diluted a significant amount, again as a result of convective mixing. The fluid has diluted further by $x/D = 16$ as the flow transitions to turbulence. The profiles for all three cases agree well at $x/D = 4$. At $x/D = 8$, the DBP mass-fraction in LES B is higher than the other cases, indicative of less entrainment and mixing, just as in the temperature profiles. At $x/D = 16$, the wake has spread similarly in all three cases. The LES cases, however, have diluted slightly less, with values up to 25% higher than the DNS. These profiles show that the LES cases are magnifying the non-unity Lewis number slightly, resulting in fluid that is just as cool as the DNS but less dilute. These results indicate the the LES cases capture the mean fluid and scalar fields reasonably well. Differences in how the DNS and LES resolve the instantaneous values of temperature and mass-fraction, however, can have a large effect on the saturation of the flow.

5.3.4 Fluid super-saturation

As the flow cools and dilutes, the fluid becomes super-saturated, defined by a saturation ratio of $S > 1$. Super-saturation implies the fluid-vapor system is no longer in thermodynamic equilibrium. A return to equilibrium entails a phase change, in this case homogeneous nucleation. Larger values of the saturation ratio indicate a larger departure from equilibrium, and necessitate higher nucleation rates to return to equilibrium. Thus, the highest saturation ratio values are indicative of where the highest nucleation rates will occur. Volume-rendered surfaces of the instantaneous saturation ratio, S, are presented in Fig. 5.2. These plots give a qualitative view of how saturation is affected when the SGS fluid-scalar interactions are modeled in LES. Figure 5.2(a) shows the saturation ratio as calculated by the DNS. A thin region of high saturation occurs immediately at the inlet, where the hot and cool streams meet. As the flow mixes, dilutes and cools, larger areas of high saturation form. By the end of the domain, the high saturation regions span the width of the wake with values generally above $S = 250$. Isolated areas above $S = 750$ can also be seen. In the LES A case, shown in Fig. 5.2(b),

much higher saturation ratio values are observed. Across the wake in the second half of the domain, values commonly reach $S = 1,000$. Isolated areas show peak values above $S = 1,500$. The surfaces for case LES B are shown in Fig. 5.2(c). In this case, the level of super-saturation is very significantly higher than both the DNS and the higher-resolution LES, with values nearing $S = 10,000$. Qualitatively, large "islands" of extremely high saturation form. This is in stark contrast to the DNS, which showed relative uniformity across the wake.

Cross-stream profiles of the time-averaged saturation ratio give a more quantitative view, and are shown in Fig. 5.3. Case LES A is compared to the DNS in Fig. 5.3(a). At the inlet, the contours are in good agreement. Here, the region of high saturation is narrow and confined to the interface between the hot and cool streams. At $x/D = 4$, the LES profile exhibits a peak value nearly one-half order of magnitude higher, though slightly narrower than the DNS profile. High saturation here is still occurring in the shear layers. By $x/D = 8$ the shear layers have met and the high saturation region spans the entire wake. The LES A values are approximately one half order of magnitude higher than the DNS. By the time the flow reaches the outlet at $x/D = 16$, the area of high saturation has widened significantly, with the LES A values one half to one order of magnitude higher than the DNS. Fig. 5.3(b) compares the LES B data to that of the DNS. The trend is very similar to Fig. 5.3(a) until $x/D = 8$. Here, LES B yields significantly higher saturation ratio values – in excess of three orders of magnitude – than the DNS. These highest values are in line with the initial shear layer location, at approximately $y/D = \pm 0.5$. By $x/D = 16$, these peaks remain, but have spread past $y/D = \pm 1$. These peaks coincide with the large "islands" of high super-saturation seen in Fig. 5.2(c), and again display a very different super-saturation field from the DNS. Even at the wake center, the lower-resolution LES predicts saturation ratio values a full order of magnitude higher than the DNS.

To better understand how cooling and dilution affect saturation, probability density functions (PDFs) of the saturation ratio are constructed. The first, shown in Fig. 5.4, is conditioned on the temperature. Saturation ratio values below $S = 1$ are omitted and peak saturation ratio values are noted for each distribution. The trends show that the highest saturation occurs at the coolest temperatures. More precisely, no high saturation occurs at high temperatures. For example, in the DNS distributions of Fig. 5.4(a), no

saturation ratio values above $S = 100$ occur when the temperature is above $\theta = 0.5$. This indicates that significant cooling is a prerequisite for high saturation. For fluid at the coolest temperatures, below $\theta = 0.25$, the distribution is quite wide. This distribution contains both the maximum at approximately $S = 1000$ and values at $S = 1$. This shows that cooling itself does not guarantee high super-saturation. The distribution for LES A is shown in Fig. 5.4(b) and LES B is shown in Fig. 5.4(c). The LES distributions show the same general trend but reach higher saturation ratio values for the coolest fluid. LES A yields a maximum saturation ratio of approximately $S = 4,000$, while LES B has a maximum of over $S = 10,000$. While the most prevalent value in the DNS ($S = 250$) is lower than both LES cases, it is of the same order of magnitude. The second set of PDFs is conditioned on the DBP mass-fraction and is shown in Fig. 5.5. In contrast to the PDFs conditioned on the temperature, the highest saturation ratio values do not exclusively coincide with the lowest concentration values. For the DNS, shown in Fig. 5.5(a), mass-fraction values up to $\phi = 0.5$ can yield saturation ratio values near the maximum of the $\phi < 0.25$ range. Even the most vapor-laden fluid – that with a value in the $0.75 < \phi < 1$ range – shows the possibility of saturation ratio values near $S = 100$. This makes sense physically, as a high saturation ratio will occur when fluid with a moderate amount of DBP vapor has cooled significantly. The LES distributions again display the same trend as the DNS. However, as the LES resolution is reduced from LES A to LES B, the fluid with the highest vapor mass fraction ($\phi < 0.25$) shows a progressively higher maximum saturation ratio value.

5.3.5 Nanoparticle nucleation

Contours of the instantaneous nucleation rate, $\log_{10}(J)$, are shown in Fig. 5.6. The structure of nucleation can be seen by first focusing on the DNS result, shown in Fig. 5.6(a). Nucleation occurs exclusively at the interface of the hot and cool stream within the first four diameters downstream of the inlet. This coincides with the regions of high saturation ratio near the inlet shown in Fig. 5.2(a). Once eddies begin to form, roll up and merge – between $x/D = 4$ and $x/D = 12$ – larger areas of nucleation form. After $x/D = 12$ nucleation becomes widespread across the wake, occurring in large structures. These structures are not homogeneous, however, with very fine areas of high nucleation. Maximum nucleation rates of approximately $J = 10^{16}\ particles/(m^3 \cdot s)$ are achieved

in this region. The same general structure is seen in the contours of LES A, shown in Fig. 5.6(b). However, as the eddies begin to merge after $x/D = 4$, nucleation is more widespread than in the DNS. By the end of the domain, after $x/D = 12$, the areas of significant nucleation – greater than $J = 10^{16}$ $particles/(m^3 \cdot s)$ – are more intense than the DNS. In case LES B, shown in Fig. 5.6(c), the nucleation rate has reached values of nearly $J = 10^{20}$ $particles/(m^3 \cdot s)$ by $x/D = 8$. By the end of the domain the areas of significant nucleation are large and span the width of the wake. These differences show that the structure of nucleation is qualitatively different in the LES, especially at low resolution. The fine structures seen in the DNS are absent. This is a consequence of both resolution that is not able to capture such small features and subgrid-scale models that greatly increase calculated saturation ratio values.

Contours of the time-averaged nucleation rate, $\log_{10}(\overline{J})$, are also shown in Fig. 5.6. The DNS contours, shown in Fig. 5.6(d), show that once the shear layers merge, nucleation becomes quite uniform across the wake. Here, values of the nucleation rate at $x/D = 8$ of $J = 10^{13}$ $particles/(m^3 \cdot s)$ increase to $J = 10^{15}$ $particles/(m^3 \cdot s)$ by the end of the domain. The nucleation rate is less uniform in the LES cases. The contours for case LES A are shown in Fig. 5.6(e). Here, the peak nucleation rate of approximately $J = 10^{18}$ $particles/(m^3 \cdot s)$ is reached at $x/D = 10$. Maxima downstream are located near the wake edges, with a center value approximately one order of magnitude lower. Case LES B is shown in Fig. 5.6(f) and exhibits a similar behavior, with a peak nucleation rate of nearly $J = 10^{20}$ $particles/(m^3 \cdot s)$. This is five orders of magnitude higher than the DNS. Additionally, the location of the maximum nucleation rate values coincides with that of the maximum saturation ratio values seen in Fig. 5.3(b). This is further evidence that the over-prediction of the saturation ratio is driving the difference in calculated nucleation rates between the LES cases and the DNS.

To quantify these differences, PDFs are constructed of the instantaneous nucleation rate and are shown in Fig. 5.7. The distributions for both LES cases exhibit a peak value of $J = 10^{13}$ $particles/(m^3 \cdot s)$. This is one order of magnitude higher than the DNS. Additionally, as the LES resolution is reduced, the maximum nucleation rate increases from $J = 10^{17}$ $particles/(m^3 \cdot s)$ in the DNS to $J = 10^{20}$ $particles/(m^3 \cdot s)$ in LES B. While the most common values of the nucleation rate are orders of magnitude lower, it is the highest nucleation rates that dominate the time-averaged values and will impact

the product particle field the most.

5.3.6 Distribution of nucleated particles

Scatter plots of the instantaneous nucleation rate versus the critical diameter are presented in Fig. 5.8. Nucleation rates below $J = 10^8\ particles/(m^3 \cdot s)$ are deemed insignificant and are not shown. Generally, the plots show that as the nucleation rate increases, smaller particles are produced. Physically, the higher nucleation rates are a result of higher super-saturation. As saturation ratio values rise, signaling a further departure from thermodynamic equilibrium, the nucleation process speeds up. The molecular clusters that grow to form stable nuclei thus have less time to grow. This results in smaller particles, produced at high nucleation rates. This trend is present in all three cases. In the DNS case, shown in Fig. 5.8(a), the critical diameter ranges from $2.9nm$ to a minimum just below $2nm$, which is produced at a rate of approximately $J = 10^{18}\ particles/(m^3 \cdot s)$. The LES A and LES B data are shown in Fig. 5.8(b) and Fig. 5.8(c), respectively. The minimum particle size produced decreases progressively from the DNS to LES A and LES B. This follows the trend of the saturation ratio and nucleation rates increasing from the DNS to the LES cases. As as the LES data reaches lower particle sizes at higher nucleation rates, the maximum size remains the same, widening the range of sizes produced. The LES cases therefore produce a particle field with more polydispersity than the DNS.

PDFs of the critical diameter d_C are constructed for all three cases and are shown in Fig. 5.9. Here the shift to lower product particle sizes in the LES cases is clear and quantifiable. The most prevalent particle size produced in the DNS is $2.4nm$. This corresponds to a nucleation rate of at most $J = 10^{14}\ particles/(m^3 \cdot s)$ in Fig. 5.8(a). In both LES cases the most prevalent critical diameter has dropped to $2.2nm$. Likewise, this size corresponds to a maximum nucleation rate less than $J = 10^{16}\ particles/(m^3 \cdot s)$ in Fig. 5.8(b) and Fig. 5.8(c). For this reason, it is more useful to examine the minimum size of each distribution. The minimum size of $1.8nm$ produced in the DNS drops to $1.6nm$ in LES A and to $1.3nm$ in LES B. While the values of the PDF are small near the minimum size, these particles are produced at the highest nucleation rates, as described in Fig. 5.8. These smallest particles are produced at nucleation rates orders of magnitude higher than the peak PDF values. Therefore, the progressive shift to smaller

minimum particle sizes in the LES cases reflects a significant alteration of the product particle field.

5.4 Conclusions

Large-eddy simulation (LES) of the nucleation of dibutyl-phthalate (DBP) particles in turbulent wakes was performed. Classical nucleation theory (CNT) is employed to compute the rate of particle formation along with the size of the particles that are produced. Results of the LES were compared to direct numerical simulation (DNS) results. One-equation, gradient-diffusion closures are used for the subgrid-scale (SGS) fluid-thermal and fluid-vapor interactions in the LES. Here also, the scalar-scalar interactions in the nucleation source term are neglected. As the resolution of the LES is lowered, the magnitude of the length-scales that require modeling increases. For this reason, LES is carried out at two resolutions.

The mean flow, temperature and vapor mass-fraction fields are captured well by the higher resolution LES, while the lower resolution LES shows slightly less entrainment. By contrast, the super-saturation of the fluid calculated from the instantaneous temperature and mass-fraction is not captured accurately in the LES cases. Qualitatively, the LES saturation field is quite different from the DNS, especially in the lower-resolution LES. Here, large "islands" of extremely high super-saturation form near the wake periphery, a structure not seen in the more uniform DNS data. The higher-resolution LES over-predicts the maximum saturation ratio by a factor of four, while the lower-resolution LES is higher by a factor of ten. This in turn leads to a gross over-prediction of the maximum instantaneous nucleation rate. The nucleation field also shows qualitative differences from the DNS, with more uniform areas of high nucleation. Driven by the over-prediction of the saturation ratio, time-averaged nucleation rates are three orders of magnitude larger in the higher-resolution LES and up to five orders of magnitude higher in the lower-resolution LES. Additionally, the LES predicts a particle field with smaller sizes and increased polydispersity. The most prevalent particle size is 8% smaller than the DNS and the minimum size – which is produced at the highest nucleation rates – is up to 27% smaller. These results show that the SGS fluid-scalar and scalar-scalar interactions have a significant effect on nucleation. Moreover, the formulation examined

here is not sufficient for simulation of homogeneous nucleation in this system. As more of the SGS interactions are modeled or ignored, vis-a-vis decreased LES resolution, the magnitude of the error becomes more severe.

LES, in spite of the aforementioned shortcomings, is computationally attractive as it requires considerably lower computational resources than DNS. While the DNS case here required approximately $41,000$ CPU-hours, the higher-resolution LES required 72 CPU-hours and the lower-resolution LES required only 17 CPU-hours. The LES is thus faster than the DNS by a factor of over 500, up to a factor of over 2000. These lower compute times are significant, making nucleation calculations via LES amenable to flows that are of engineering interest. Improvements to the predictive capabilities of LES when complex, non-linear source terms are present (similar to the nucleation source term here) have been made through the use of probabilistic methods, particularly in the area of combustion [34, 112, 95]. Though probabilistic methods have been applied to LES of nucleation in a limited number of cases, simple mixing models are often used [66]. It is evident from these results that care must be taken when modeling the SGS interactions and mixing, as the physics therein greatly affect nucleation calculations. It is also clear that SGS closures for homogeneous nucleation would greatly advance simulation capabilities, yielding faster, more accurate simulations through the use of LES in similar systems.

	DNS	LES A	LES B
Resolution	2.3×10^8	1.2×10^6	2.6×10^5
	$(1152 \times 704 \times 288)$	$(192 \times 128 \times 48)$	$(128 \times 64 \times 32)$
Turbulent Prandtl number, Pr_t	N/A	0.8	0.7
Turbulent Schmidt number, Sc_t	N/A	0.8	0.7
Eddy viscosity constant, C_R	N/A	0.02	0.02
Computational cost (CPU-hours)	41,000	72	17

Table 5.1: Simulation parameters

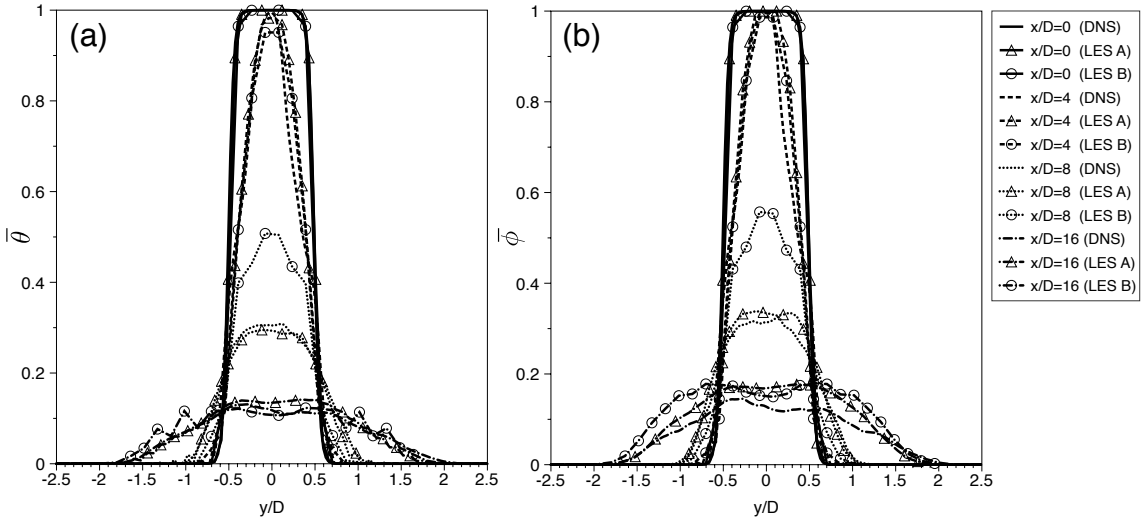

Figure 5.1: Cross-stream profiles of time-averaged (a) temperature, $\overline{\theta}$, and (b) DBP mass-fraction, $\overline{\phi}$, at four axial locations.

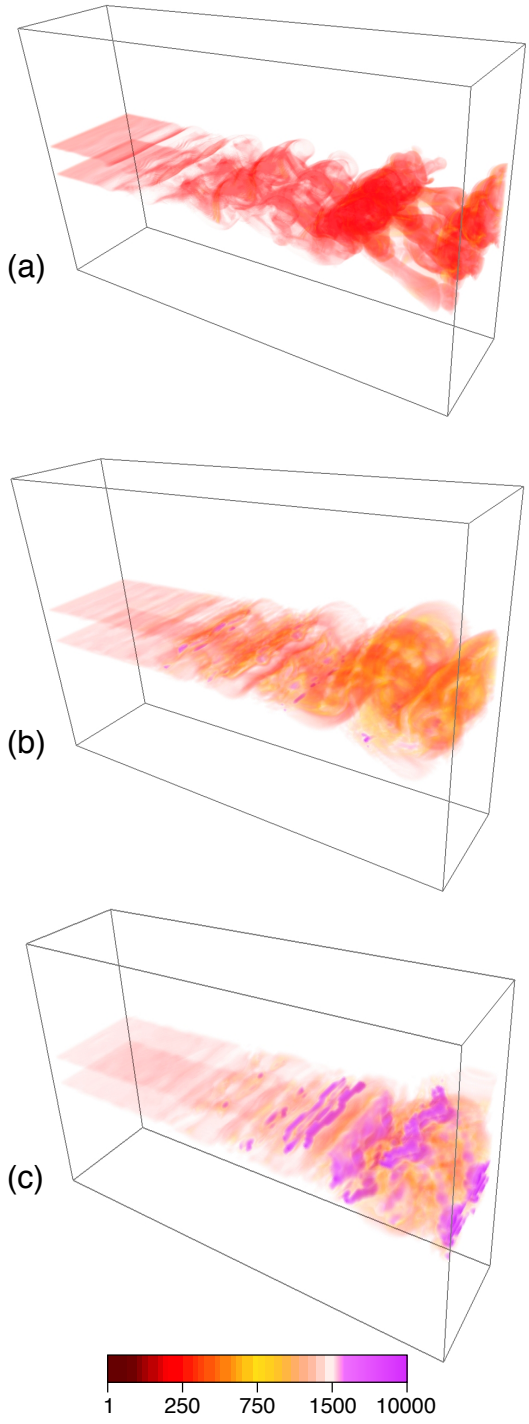

Figure 5.2: Volume rendered surfaces of the instantaneous saturation ratio, S: (a) DNS; (b) LES A; (c) LES B.

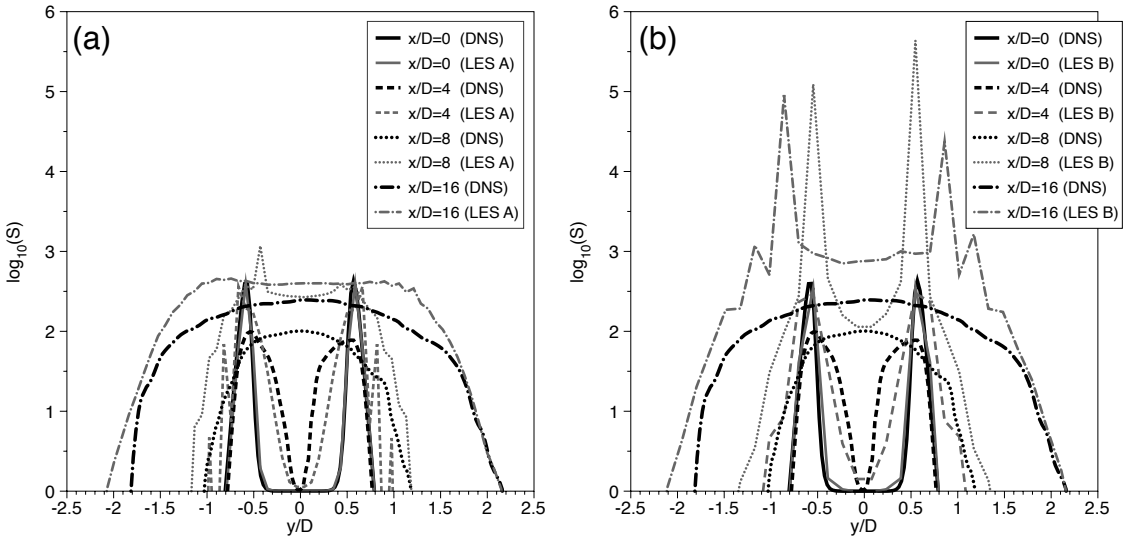

Figure 5.3: Cross-stream profiles of the time-averaged saturation ratio, $\overline{S}$, for the DNS and (a) LES A; (b) LES B at four axial locations

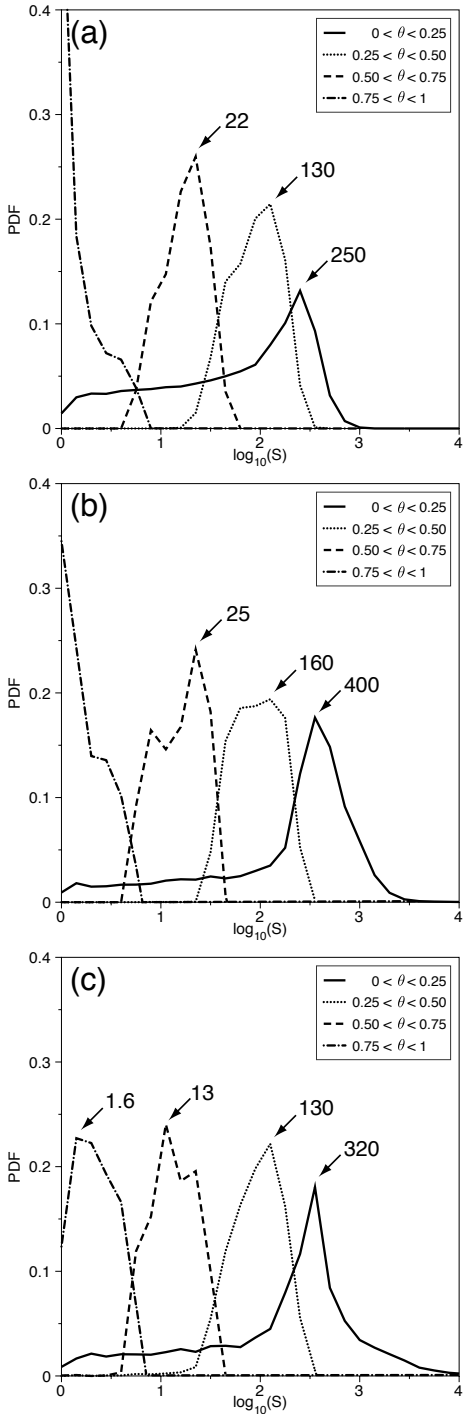

Figure 5.4: Probability density function of the saturation ratio, S, conditioned on the temperature, θ: (a) DNS; (b) LES A; (c) LES B.

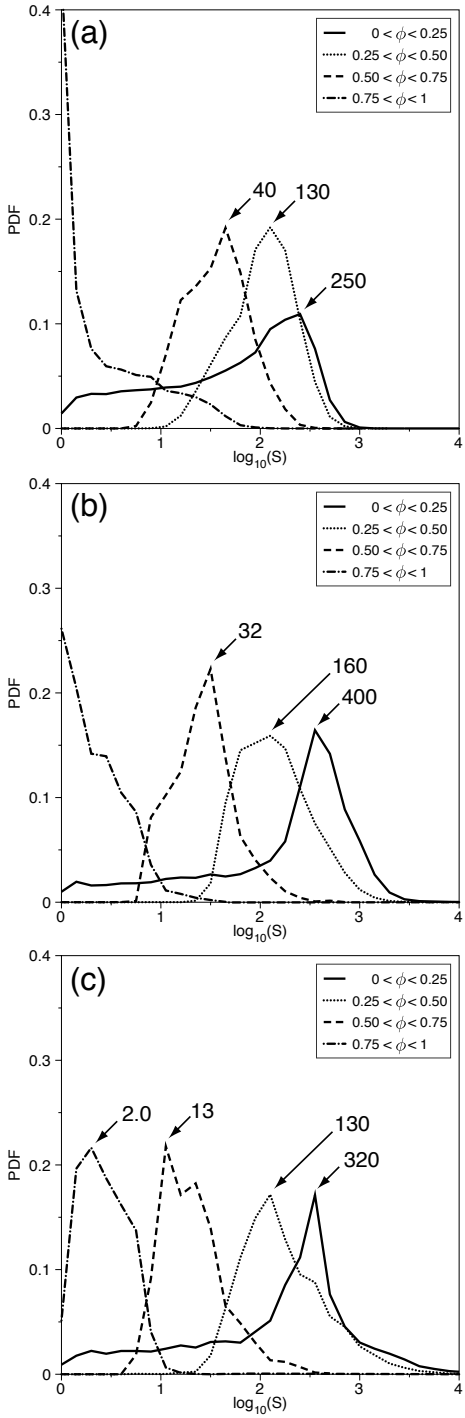

Figure 5.5: Probability density function of the saturation ratio, S, conditioned on the DBP mass-fraction, ϕ: (a) DNS; (b) LES A; (c) LES B.

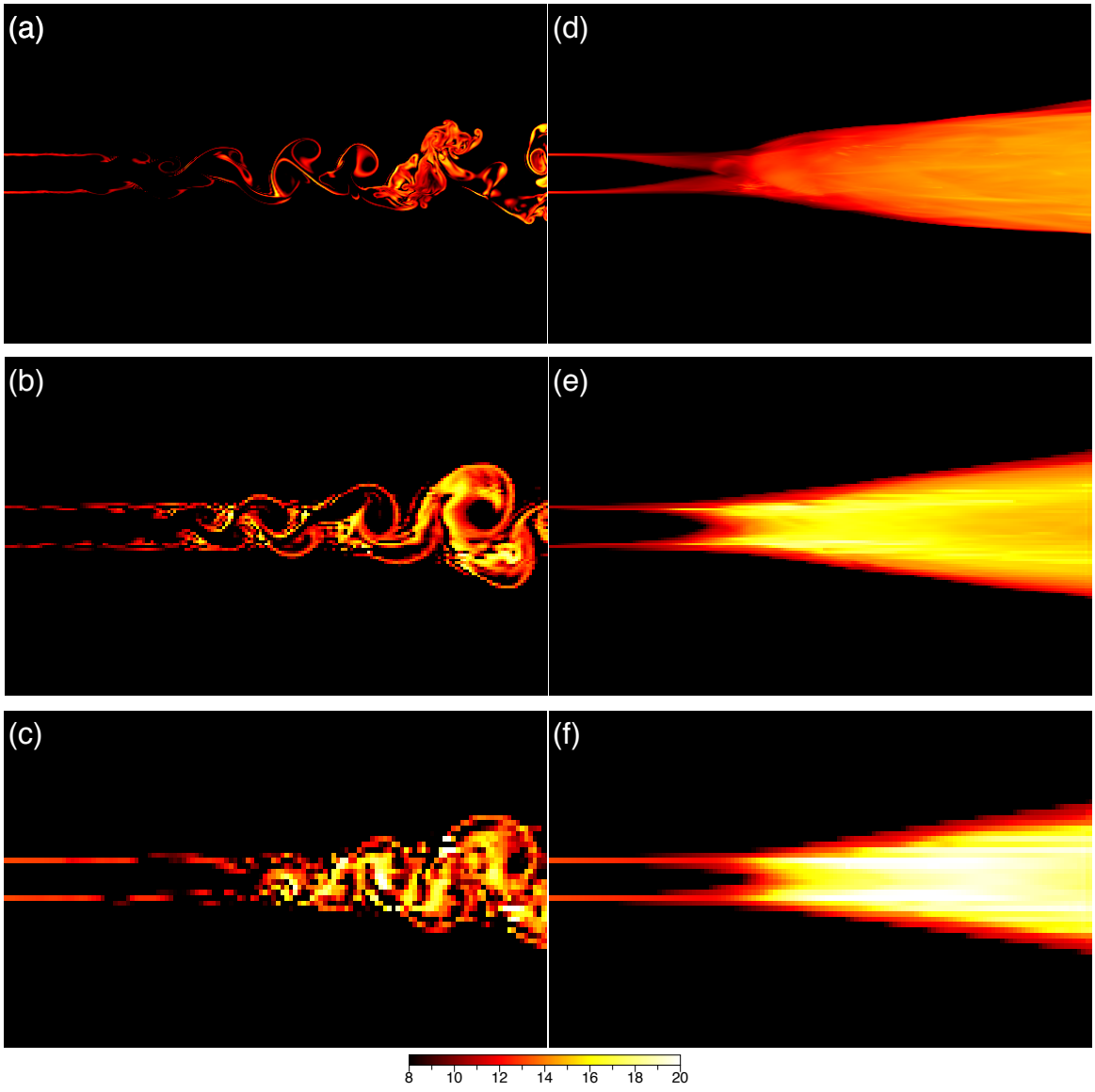

Figure 5.6: Instantaneous contours of the nucleation rate, $\log_{10}(J)$ $(particles/(m^3 \cdot s))$, at z=0: (a) DNS; (b) LES A; (c) LES B. Contours of the time-averaged nucleation rate, $\log_{10}(\overline{J})$ $(particles/(m^3 \cdot s))$: (d) DNS; (e) LES A; (f) LES B.

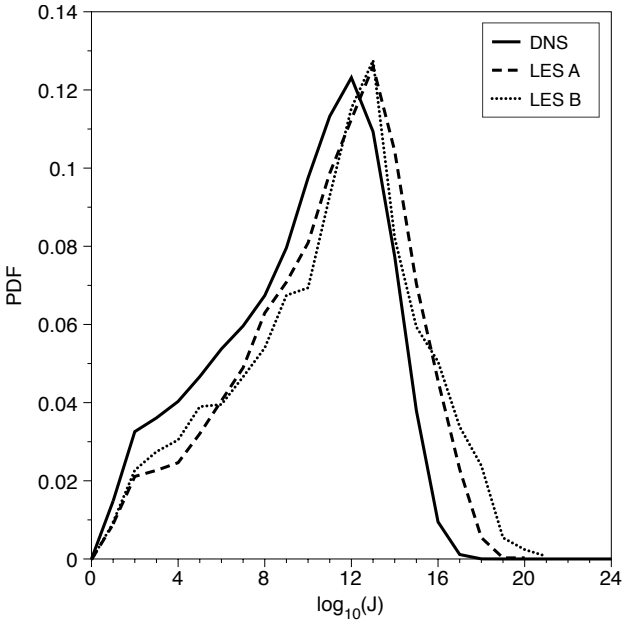

Figure 5.7: Probability density function of the nucleation rate, $\log_{10}(J)$ $(particles/(m^3 \cdot s))$.

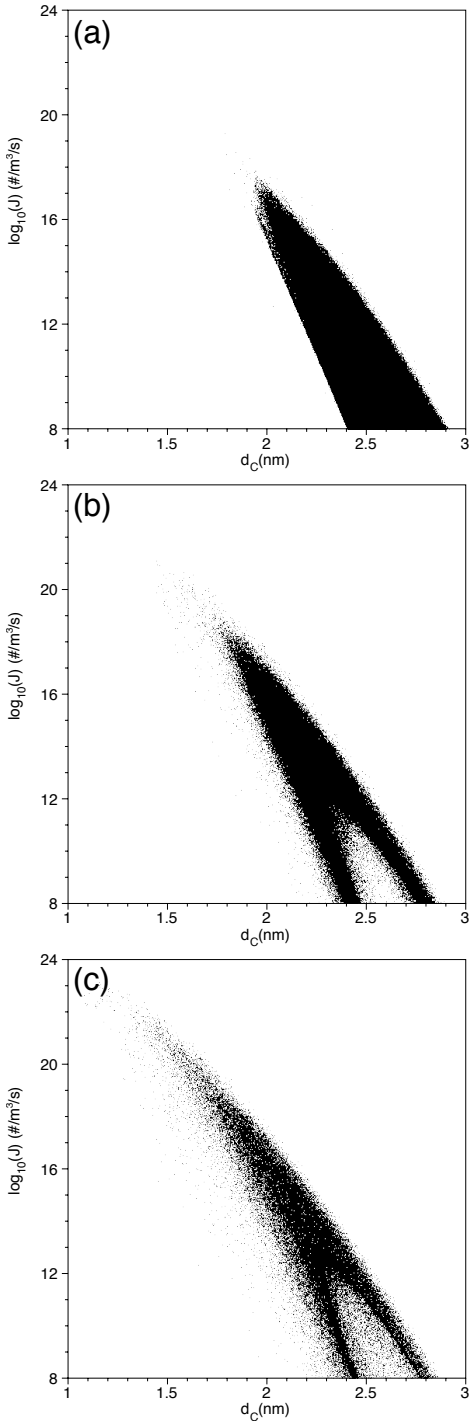

Figure 5.8: Nucleation rate – critical diameter scatter-plots: (a) DNS; (b) LES A; (c) LES B.

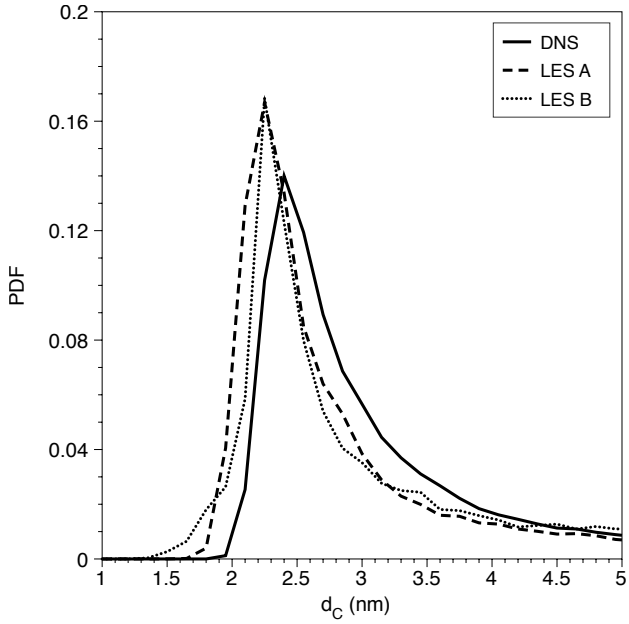

Figure 5.9: Probability density function of the critical diameter, d_C (nm).

Chapter 6

Conclusions and future work

The work detailed here was carried out to further our knowledge of homogeneous nucleation in the context of numerical simulation. Direct numerical simulation (DNS) and large eddy simulation (LES) were utilized. First, a qualitative assessment of the structure of nucleation was carried out via DNS. As the flow left the nozzle, mixed initially and then transitioned to turbulence, three distinct nucleation regimes were seen. These correlate well with past experimental observation. The DNS data was next used to show that both the level of large-scale mixing and the level of vapor concentration affect nucleation; an increase in either results in an increase in nucleation. These results demonstrate how sensitive the nucleation process is to mixing phenomena. Small changes in the dilution process were shown to affect the predicted nucleation by many orders or magnitude. When it is assumed that the vapor mass and temperature diffuse equally, the prediction of nucleation rates and particle sizes were shown to be drastically altered. Maximum nucleation rates were lowered and larger particles were produced. The DNS data was next used for an *a priori* analysis of the effects of turbulent concentration and temperature fluctuations. The fluctuations (which are not resolved in LES) were shown to greatly affect both nucleation rates and product particle sizes. These results implied that LES of nucleation may not capture the nucleation process accurately. Finally, LES of homogeneous nucleation was carried out. The LES was compared to the DNS data and was shown to greatly over-predict nucleation rates and under-predict product particle sizes once the flow transitioned to turbulence. As a result, LES was

shown to be an inadequate tool to simulate homogeneous nucleation with the condensable species adopted here. These results provide valuable insight into the nucleation process, as well as show the current limits of our simulation capabilities.

A probability-based approach termed the filtered density function (FDF) method has been shown by others to more accurately capture the small-scale fluctuations that were shown in this work to significantly affect nucleation. The use of this type of method should predict nucleation more accurately than LES, while keeping computational costs reasonable. The use of mixing models capable of differential diffusion of the Lagrangian particles in composition space is paramount to making nucleation calculations via LES more accurate. Since the advent of the coalescence and dispersion (CD) model by Curl in 1963 [113] many mixing models have been introduced, including the interaction with the mean (IEM) or linear mean-square estimation (LMSE), Fokker-Planck based (FP), mapping closure (MC), multiple mapping conditioning (MMC) and parametrization of one-dimensional scalar profiles (PSP) models [37, 38, 114, 115]. Though much progress has been made and new models are still emerging [116], there is still research to be done in the area of modeling micro-scale mixing and improvements to be made [117]. Nevertheless, mixing models provide the final closure needed in an LES-FDF method and realize the small-scale interactions needed to accurately simulate complicated source terms such as in combustion, or in this case nucleation. However, this work has shown that assuming temperature and mass diffuse equally is insufficient for accurate simulation of homogeneous nucleation. The current FDF methodology and mixing models require the Lagrangian particles that are used to resolve the turbulent fluctuations in temperature and mass-fraction to diffuse equally. This work has shown that the assumption of equal diffusivities is not sufficient. As a result, the FDF method was not adopted here. In future work, a successful LES-FDF method could be applied not only to nucleation, but to various source terms encompassing a wide variety of physics.

References

[1] J. Frenkel. *Kinetic theory of liquids*. Oxford Press, 1946.

[2] E. E. Finney and R. G. Finke. Nanocluster nucleation and growth kinetic and mechanistic studies: A review emphasizing transition-metal nanoclusters. *J. Colloid Interface Sci.*, 317:351–374, 2008.

[3] Xiaochun Cao, Jun Ma, Xuehua Shi, and Zhijun Ren. Effect of TiO2 nanoparticle size on the performance of PVDF membrane. *Applied Surface Science*, 253(4):2003–2010, 2006.

[4] A.P. Chernyshev. Effect of nanoparticle size on the onset temperature of surface melting. *Materials Letters*, 63(17):1525–1527, 2009.

[5] Z. Tang, D. Geng, and G. Lu. Size-controlled synthesis of colloidal platinum nanoparticles and their activity for the electrocatalytic oxidation of carbon monoxide. *J. Colloid Interface Sci.*, 287:159–166, 2005.

[6] A. Mayer, M. Vadon, B. Rinner, A. Novak, R. Wintersteiger, and E. Fröhlich. The role of nanoparticle size in hemocompatibility. *Toxicology*, 258:139–147, 2009.

[7] F. Aristizabal, J. R. Munz, and D. Berk. Modeling of the production of ultra fine aluminium particles in rapid quenching turbulent flow. *J. Aeros. Sci* ., 37(2):162–186, 2006.

[8] V. Jaenisch, F. Stratmann, D. Nilsson, and P. H. Austin. Influence of turbulent mixing processes on new particle formation rates. *J. Aerosol Sci.*, 29:S1063–S1064, 1998.

[9] E. D. Nillsson, U. Rannik, M. Kulmala, G. Buzorious, and C. D. O'Dowd. Effects of continental boundary layer evolution, convection, turbulence and entrainment, on aerosol formation. *Tellus B*, 53:441–461, 2001.

[10] P. C. Reist. *Aerosol Science and Technology.* McGraw-Hill, New York, NY, 2nd edition, 1993.

[11] W. C. Hinds. *Aerosol technology: properties, behavior and measurement of airborne particles.* John Wiley and Sons, New York, NY, 1999.

[12] D. Kashchiev. *Nucleation: basic theory with applications.* Butterworth Heinemann, 2000.

[13] J. W. Gibbs. On the equilibrium of heterogeneous substances. *transactions of the Connecticut academy of arts and sciences, third series*, XVI(96):343–524, 1878.

[14] M. Volmer and A. Weber. Keimbildung in übersättigten gebilden. *Zeitschrift für physikalische Chemie, Abt. A*, 119:227–301, 1926.

[15] C. T. R. Wilson. On the cloud method of making visible ions and the tracks of ionizing particles. Nobel Lecture, December 1927.

[16] R. Becker and W. Döring. Kinetische behandlung der keimbildung in übersättigten dämpfern. *Ann. Phys. (Leipzig)*, 24:719–752, 1935.

[17] K. S. Friedlander. *Smoke, Dust and Haze: Fundamentals of Aerosol Dynamics.* Oxford University Press, New York, NY, 2000.

[18] W. C. Reynolds. The potential and limitations of direct and large eddy simulations. In J. L. Lumley, editor, *Whither Turbulence? Turbulence at the Crossroads*, volume 357 of *Lecture Notes in Physics*, pages 313–343. Springer-Verlag, New York, NY, 1990.

[19] S. Cant. High-performance computing in computational fluid dynamics: progress and challenges. *Phil. Trans. R. Soc. Lond. A.*, 360:1211–1225, 2002.

[20] N. Kasagi. Progress in direct numerical simulation of turbulent transport and its control. *Int. J. Heat and Fluid Flow*, 19:125–134, 1998.

[21] S. C. Garrick, S. Modem, M. R. Zachariah, and K. E. J. Lehtinen. Simulation of particle coagulation in temporally developing mixing layers. In C. Liu, L. Sakell, and T. Beutner, editors, *DNS/LES - Progress and Challenges*, pages 621–628. Greyden Press, Columbus, OH, 2001.

[22] G. Wang and S. C. Garrick. Modeling and simulation of titania formation and growth in temporal mixing layers. *J. Aeros. Sci* ., 37(4):431—451, 2006.

[23] S. C. Garrick and G. Wang. Modeling and simulation of titanium dioxide nanoparticle synthesis with finite-rate sintering in planar jets. *Journal of Nanoparticle Research*, pages 1–12, 2010. 10.1007/s11051-010-0097-x.

[24] N. Georgiadis, D. P. Rizzetta, and C. Fureby. Large-eddy simulation: current capabilities, recommended practices, and future research. *AIAA J.*, 48(8), 2010.

[25] M. C. Paul, M. M. Molla, and G. Roditi. Large–eddy simulation of pulsatile blood flow. *Medical Engineering and Physics*, 31:153–159, 2009.

[26] J. Jiang and K. Zhao. Airflow and nanoparticle deposition in rat nose under various breathing and sniffing conditions—a computational evaluation of the unsteady and turbulent effect. *J. Aeros. Sci* ., 41, 2010.

[27] D. Marchisio. Large eddy simulation of mixing and reaction in a confined impinging jets reactor. *Computers and Chemical Engineering*, 33:408–420, 2008.

[28] H. Pitsch. Large-eddy simulation of turbulent combustion. *Ann. Rev. Fluid Mech.*, 38:453–482, 2006.

[29] S. C. Garrick, F. A. Jaberi, and P. Givi. Large eddy simulation of scalar transport in a turbulent jet flow. In D. Knight and L. Sakell, editors, *Recent Advances in DNS and LES*, volume 54 of *Fluid Mechanics and its Applications*, pages 155–166. Kluwer Academic Publishers, The Netherlands, 1999.

[30] J. Loeffler, S. Das, and S. C. Garrick. Large eddy simulation of titanium dioxide nanoparticle formation and growth in turbulent jets. submitted to *Aerosol Sci. and Technol.*, 2010.

[31] P. Givi. Model free simulations of turbulent reactive flows. *Prog. Energy Combust. Sci.*, 15:1–107, 1989.

[32] S. B. Pope. Computations of turbulent combustion: Progress and challenges. In *Proceedings of 23rd Symp. (Int.) on Combustion*, pages 591–612. The Combustion Institute, Pittsburgh, PA, 1990.

[33] D.C. Haworth. Progress in probability density function methods for turbulent reacting flows. *Prog. Energy Combust. Sci.*, 36, 2010.

[34] P. J. Colucci, F. A. Jaberi, P. Givi, and S. B. Pope. Filtered density function for large eddy simulation of turbulent reacting flows. *Phys. Fluids*, 10(2):499–515, 1998.

[35] S. B. Pope. PDF methods for turbulent reactive flows. *Prog. Energy Combust. Sci.*, 11:119–192, 1985.

[36] M.R.H. Sheikhi, T.G. Drozda, P. Givi, F.A. Jaberi, and S. B. Pope. Large eddy simulation of a turbulent nonpremixed piloted methane jet flame (sandia flame d). *Proc. Combust. Inst.*, 30, 2005.

[37] B. Merci, D. Roekaerts, B. Naud, and S. B. Pope. Comparative study of micromixing models in transported scalar PDF simulations of turbulent nonpremixed bluff body flames. *Combust. Flame*, 146, 2006.

[38] B. Merci, D. Roekaerts, and B. Naud. Study of the performance of three micromixing models in transported scalar pdf simulations of a piloted jet diffusion flame ("Delft Flame III"). *Combust. Flame*, 144:476–493, 2006.

[39] B. D. Shaw. Asymptotic evaluation of probability density functions for mean aerosol particle formation rates by homogeneous nucleation in turbulent gas jets. *J. Aerosol Sci.*, 35(2):177–184, 2004.

[40] A. Garmory and E. Mastorakos. Aerosol nucleation and growth in a turbulent jet using the stochastic fields method. *Chemical Engineering Science*, 63:4078–4089, 2008.

[41] M. D. Carrara and P. E. DesJardin. A filtered mass density function approach for modeling separated two-phase flows for les ii: Simulation of a droplet laden temporally developing mixing layer. *Int. J. Multiphase Flow*, pages 748–766, 2008.

[42] S. B. Pope. *Turbulent Flows*. Cambridge University Press, Cambridge, UK, 2000.

[43] Y. Xiong and S. E. Pratsinis. Formation of agglomerate particles by coagulation and sintering - part I. A two-dimensional solution of the population balance equation. *J. Aerosol Sci.*, 24(3):283–300, 1993.

[44] E. G. Moody and L. R. Collins. Effect of mixing on the nucleation and growth of titania particles. *Aerosol Sci. Technol.*, 37(5):403–424, 2003.

[45] G. Wang and S. C. Garrick. Modeling and simulation of titania formation and growth in temporal mixing layers. submitted to *J. Aerosol Sci.*, 2003.

[46] I. Kennedy. Models of soot formation and oxidation. *Prog. Energy Combust. Sci.*, 23:95–132, 1997.

[47] M. J. Zimberg, S. H. Frankel, J. P. Gore, and Y. R. Sivathanu. A study of coupled turbulence, soot chemistry and radiation effects using the linear eddy model. *Combustion and Flame*, 113(3):454–469, 1998.

[48] P. P. Wegener and A. A. Pouring. Experiments on condensation of water vapor by homogeneous nucleation in nozzles. *Phys. Fluids.*, 7:352–361, 1964.

[49] Y. Bayazitoglu, R. F. Brotzen, and Y. Zhang. Metal vapor condensation in a converging nozzle. *Nanostructured Materials*, 7(7):789–803, 1996.

[50] T. Lesniewski and S. K. Friedlander. Particle nucleation and growth in a free turbulent jet. *Proc. R. Soc. Lond. A*, 454:2477–2504, 1998.

[51] T. Lesniewski and S. K. Friedlander. The effect of turbulence on rates of particle formation by homogeneous nucleation. *Aerosol Sci. Technol.*, 23(2):174–182, August 1995.

[52] J. Wu and S. Menon. Aerosol dynamics in the near field of engine exhaust plumes. *J. Appl. Meteor.*, 40:795–809, 2001.

[53] C. Housiadas, Y. Drossinos, and M. Lazaridis. Effect of small-scale turbulent fluctuations on rates of particle formation. *J. Aerosol Sci.*, 35:545–559, 2004.

[54] S. Miller and S. C. Garrick. Nanoparticle coagulation in a planar jet. *Aerosol Sci. Technol.*, 38(1):79–89, 2004.

[55] S. C. Garrick and M. Khakpour. The effects of differential diffusion on nanoparticle coagulation in temporal mixing layers. *Aerosol Sci. Technol.*, 38(8):851–860, August 2004.

[56] S. Das and S. C. Garrick. The effects of turbulence on nanoparticle growth in turbulent reacting jets. *Phys. Fluids*, 22, October 2010.

[57] S. L. Girshick and C. Chiu. Kinetic nucleation theory: A new expression for the rate of homogeneous nucleation from an ideal supersaturated vapor. *J. Chem. Phys.*, 93(2):1273–1277, 1990.

[58] H. V. Nguyen, K. Okuyama, T. Mimura, Y. Kousaka, R. Flagan, and S. Seinfeld. Homogeneous and heterogeneous nucleation in a laminar flow aerosol generator. *J. Colloid Interf. Sci.*, 119:491–504, 1987.

[59] J. Pyykönen and J. Jokiniemi. Computational fluid dynamics based sectional aerosol modelling schemes. *J. Aerosol Sci.*, 31(5):531–550, 2000.

[60] F. Raes and A. Janssens. Ion-induced aerosol formation in a H2O-H2SO4 system–II. Numerical calculations and conclusions. *J. Aerosol. Sci.*, 17(4):715–722, 1986.

[61] M. Wilck and F. Stratmann. A 2-d multicomponent model aerososl and its application to laminar flow reactors. *J. Aerosol Sci.*, 28:959–972, 1997.

[62] M. Wilck, K. Hämeri, F. Stratmann, and M. Kulmala. Determination of homogeneous nucleation rates from laminar-flow diffusion chamber data. *J. Aerosol. Sci.*, 29(8):899–911, 1998.

[63] R. W. MacCormack. The effect of viscosity in hypervelocity impact catering. AIAA Paper 69-354, 1969.

[64] C. A. Kennedy and M. H. Carpenter. Several new numerical methods for compressible shear-layer simulations. *Appl. Num. Math.*, 14:397–433, 1994.

[65] P. A. McMurtry, J. J. Riley, and R. W. Metcalfe. Effects of heat release on the large scale structures in a turbulent reacting mixing layer. *J. Fluid Mech.*, 199:297–332, 1989.

[66] G. Y. Di Veroli and S. Rigopoulos. Modeling of aerosol formation in a turbulent jet with the transported population balance equation-probability density function approach. *Phys. Fluids*, 23:043305, 2011.

[67] D.E. Rosner and M. Epstein. Fog formation conditions near cool surfaces. *J. Colloid Interf. Sci*, 28(1):61–65, 1968.

[68] C. Clement. Aerosol formation from heat and mass transfer in vapour-gas mixtures. *Proc. R. Soc. Lond. A*, 398:307–309, 1985.

[69] P. H. McMurry. New particle formation in the presence of an aerosol: rates, time scales and sub-0.01 μm size distributions. *J. Coll. Interf. Sci.*, 95(1):72–80, 1983.

[70] P. H. McMurry. Photochemical aerosol formation from SO_2: A theoretical analysis of smog chamber data. *J. Coll. Interf. Sci.*, 78(2):513–527, 1980.

[71] M. H. Carpenter. A high-order compact numerical algorithm for supersonic flows. In K. W. Morton, editor, *Twelfth International Conference on Numerical Methods in Fluid Dynamics*, volume 371 of *Lecture Notes in Physics*, pages 254–258. Springer-Verlag, New York, NY, 1990.

[72] D. H. Rudy and J. C. Strikwerda. A nonreflecting outflow boundary condition for subsonic navier-stokes calculations. *J. Comp Phys.*, 36:55–70, 1980.

[73] M. Frenklach. Reaction mechanism of soot in flames. *Phys. Chem. Chem. Phys*, 4:2028–2037, 2002.

[74] E. Bodenschatz, S. P. Malinowski, R. A. Shaw, and F. Stratmann. Can we understand clouds without turbulence? *Science*, 327:970–971, February 2010.

[75] K. Hämeri and M. Kulmala. Homogeneous nucleation in a laminar flow diffusion chamber: The effect of temperature and carrier gas on dibutyl phthalate vapor nucleation rate at high supersaturations. *J. Chem. Phys.*, 105(17):7696–7704, 1996.

[76] M. P. Anisimov and G. C. Cherevko. Gas-flow diffusion chamber for vapour nucleation studies. relations between nucleation rate, critical nucleus size and entropy of transition from a metastable into a stable state. *J. Aerosol Sci.*, 16:97–107, 1985.

[77] D.R. Warren, K. Okuyama, Y. Kousaka, J. H. Seinfeld, and R. C. Flagan. Homogeneous nucleation in supersaturated vapor containing foreign seed aerosol. *J. Colloid Interf. Sci.*, 116:563–581, 1987.

[78] K. Okuyama, Y. Kousaka, D. R. Warren, R. C. Flagan, and J. H. Seinfeld. Homogeneous nucleation by continuous mixing of high temperature vapor with room temperature gas. *Aerosol Sci. Technol.*, 6:15–27, 1987.

[79] J. Pyykönen, M. Miettinenb, O. Sippulab, A. Leskinenb, T. Raunemaab, and J. Jokiniemi. Nucleation in a perforated tube diluter. *J. Aerosol Sci.*, 38:172–191, 2007.

[80] A. J. Fager, J. Liu, and S. C. Garrick. Hybrid simulations of metal particle nucleation: A priori and a posteriori analyses of the effects of unresolved scalar interactions on nanoparticle nucleation. *Phys. Fluids*, 24:075110–1 – 075110–18, 2012.

[81] C. F. Clement. Aerosol formation from heat and mass transfer in vapour-gas mixtures. *Proc. R. Soc. Lond.*, 398:307–339, 1985.

[82] S. C. Garrick. Effects of turbulent fluctuations on nanoparticle coagulation in shear flows. *Aerosol Sci. and Technol.*, 45:1271–1285, 2011.

[83] R. C. Easter and L. K. Peters. Binary homogeneous nucleation: Temperature and relative humidity fluctuations, nonlinearity, and aspects of new particle production in the atmosphere. *J. Appl. Meteor.*, 33:775–784, 1994.

[84] K. Harstad and J. Bellan. Modeling of multicomponent homogeneous nucleation using continuous thermodynamics. *Combust. Flame*, 139:252–262, 2004.

[85] P. P. Wegener and K. R. Sreenivasan. The effect of cooling rate on binary nucleation. *Appl. Sci. Res.*, 37:183–194, 1981.

[86] A. A. Onischuk, P. A. Purtov, A. M. Baklanov, V. V. Karasev, and S. V. Vosel. Evaluation of surface tension and Tolman length as a function of droplet radius from experimental nucleation rate and supersaturation ratio: Metal vapor homogeneous nucleation. *J. Chem. Phys.*, 124, 2006.

[87] J. Liu and S. C. Garrick. Comment on "evaluation of surface tension and Tolman length as a function of droplet radius from experimental nucleation rate and supersaturation ratio: Metal vapor homogeneous nucleation". *J. Chem. Phys.*, 132(1), 2010.

[88] F. C. Goodrich. Nucleation rates and the kinetics of particle growth ii. the birth and death process. *Proc. R. Soc. Lond. A*, 277(1369):167–182, 1964.

[89] H. Tennekes and J. L. Lumley. *A First Course in Turbulence*. MIT Press, Cambridge, MA, 1972.

[90] A. Roshko. On the development of turbulent wakes from vortex streets. Technical report, NACA, 1954.

[91] V. A. Shneidman. Theory of time dependent nucleation and growth during a rapid quench. *J. Chem. Phys.*, 103(22):9772—9783, Dec. 1995.

[92] A. A. Aldama. Filtering techniques for turbulent flow simulations. volume 49 of *Lecture Notes in Engineering*. Springer-Verlag, New York, NY, 1990.

[93] M. Germano. Turbulence: The filtering approach. *J. Fluid Mech.*, 238:325–336, 1992.

[94] S. C. Garrick. Large eddy simulations of a turbulent reacting mixing layer. AIAA Paper 95-0010, 1995.

[95] F. A. Jaberi, P. J. Colucci, S. James, P. Givi, and S. B. Pope. Filtered mass density function for large eddy simulation of turbulent reacting flows. *J. Fluid Mech.*, 401, December 1999.

[96] L. Y. M. Gicquel, P. Givi, F. A. Jaberi, and S. B. Pope. Velocity filtered density function for large eddy simulation of turbulent flows. *Phys. Fluids*, 14(3):1196–1214, 2002.

[97] P. Givi. Filtered density function for subgrid scale modeling of turbulent combustion. *AIAA J.*, 44(1):16–23, January 2006.

[98] A. J. Hayter. *Probability and Statistics for Engineers and Scientists*. PWS Publishing Company, Boston, MA, 1996.

[99] S. Viswanathan, H. Wang, and S. B. Pope. Numerical implementation of mixing and molecular transport in LES/PDF studies of turbulent reacting flows. *J. Comp. Phys.*, 230:6917–6957, 2011.

[100] R. Zhang. Getting to the critical nucleus of aerosol formation. *Science*, 328, 2010.

[101] Z. Q. Yin, J. Z. Lin, K. Zhou, and T. L. Chan. Numerical simulation of the formation of pollutant nanoparticles in the exhaust twin-jet plume of a moving car. *Int. J. of Nonlinear Sciences and Numerical Simulation*, 8(4):535–543, 2007.

[102] Z. Yin and J. Lin. Numerical simulation of the formation of nanoparticles in an impinging twin-jet. *Journal of Hydrodynamics, Ser. B*, 19(5):533–541, 2007.

[103] M-Z. Yu, J-Z. Lin, and T-L. Chan. Effect of precursor loading on non-spherical tio2 nanoparticle synthesis in a diffusion flame reactor. *Chem. Eng. Sci.*, 64(9):2317–2329, 2008.

[104] T. L. Chan, Liu Y. H., and C. K. Chan. Direct quadrature method of moments for the exhaust particle formation and evolution in the wake of the studied ground vehicle. *J. Aerosol Sci.*, 41:553–568, 2010.

[105] G. Dong and T. L. Chan. Large eddy simulation of flow structures and pollutant dispersion in the near-wake region of a light-duty diesel vehicle. *Atmospheric Environment*, 40:1104–1116, 2006.

[106] K. Zhou and T. L. Chan. Simulation of homogeneous particle nucleation in a free turbulent jet. *Aerosol Sci. Technol.*, 45(8):973–987, 2011.

[107] J. Smagorinsky. General circulation experiments with the primitive equations. I. The basic experiment. *Monthly Weather Review*, 91(3):99–164, 1963.

[108] B. Vreman, B. Geurts, and H. Kuerten. Realizability conditions for the turbulent stress tensor in large-eddy simulation. *J. Fluid Mech.*, 278:351–362, 1994.

[109] R. M. Kerr, J. A. Domaradzki, and G. Barbier. Small-scale properties of nonlinear interactions and subgrid-scale energy transfer in isotropic turbulence. *Phys. Fluids*, 8(1):197–208, 1996.

[110] J. Colucci, P. *Large Eddy Simulation of Turbulent Reactive Flows: Stochastic Representation of the Sub-Grid Scale Scalar Fluctuations*. Ph.D. Thesis, Department of Mechanical and Aerospace Engineering, State University of New York at Buffalo, Buffalo, NY, 1998.

[111] T. M. Eidson. Numerical simulation of the turbulent Rayleigh-Benard problem using subgrid modelling. *J. Fluid Mech.*, 158:245–268, 1985.

[112] S. C. Garrick. *Large Eddy Simulation of Turbulent Reacting Jets*. Ph.D. Thesis, Department of Mechanical and Aerospace Engineering, State University of New York at Buffalo, Buffalo, NY, 1998.

[113] R. L. Curl. Dispersed phase mixing: I. Theory and effects in simple reactors. *AIChE J.*, 9(2):175–181, 1963.

[114] D. W. Meyer and P. Jenny. Micromixing models for turbulent flows. *J. Comp Phys.*, 228:1275–1293, 2009.

[115] M. Stöllinger and S. Heinz. Evaluation of scalar mixing and time scale models in pdf simulations of a turbulent premixed flame. *Combust. Flame*, 157:1671–1685, 2010.

[116] D. W. Meyer. A new particle interaction mixing model for turbulent dispersion and turbulent reactive flows. *Phys. Fluids*, 22, 2010.

[117] H. I. Andersson and P. Å. Krogstad, editors. *Advances in PDF methods for turbulent reactive flows*, Barcelona, 2004. Proceedings of the Tenth European Turbulence Conference, CIMNE.